

ABSTRACT

Title of dissertation: SIGNAL DENOISING FOR EXO-200
AND AN IMPROVED LIMIT ON
NEUTRINOLESS DOUBLE-BETA DECAY

Clayton G. Davis, Doctor of Philosophy, 2014

Dissertation directed by: Professor Carter Hall
Department of Physics

The EXO-200 detector is designed to measure the spectrum of Xenon-136 double-beta ($\beta\beta$) decay. This extremely low-rate radioactive process is interesting on its own, but more profound is its potential to reveal non-standard neutrinoless double-beta ($\beta\beta0\nu$) decay. $\beta\beta0\nu$ decay, if it occurs, would have important consequences for our understanding of the neutrino sector of the standard model. It would demonstrate the type of the neutrino mass term; set the mass scale of the neutrino sector; and demonstrate the first direct observation of lepton number non-conservation.

In the EXO-200 detector, we measure the summed energy of the two emitted electrons. The summed-electron-energy spectrum of standard $\beta\beta$ decay produces a smooth spectrum due to the "missing" energy of the two emitted neutrinos. In contrast, the non-standard $\beta\beta0\nu$ decay has no neutrino products, and emits energy only in the form of electrons. Since all energy is captured by the electrons, the sum of electron energies will always be 2458 keV; thus, we can discover this process by looking for a peak in the summed electron energy spectrum at this energy.

The sensitivity of the search depends on two basic factors: accumulated Xenon-136 exposure, and expected background near 2458 keV from non- $\beta\beta0\nu$ decays. The EXO-200 detector was designed to minimize background primarily through its construction. All materials used in the construction of the EXO-200 detector were carefully screened for low concentration of radioactive backgrounds, making the EXO-200 detector one of the lowest-background detectors in the world.

Backgrounds were also minimized in EXO-200 by ensuring that the energy resolution of the detector would be excellent. Good energy resolution ensures that all monoenergetic peaks (including both $\beta\beta0\nu$ and background gamma lines) will be sharp. When background is integrated over the width of the $\beta\beta0\nu$ expected peak, we wish for the integrated number of expected counts to be as small as possible; when peaks are sharper, we can expect that integral to be smaller.

When the EXO-200 detector turned on, its scintillation signals observed more electronic noise than had been expected based on design goals. The present work is concerned with improving the energy resolution of the EXO-200 detector by removing electronic noise by an offline denoising process. It will be concerned with a detailed characterization of the signal and noise behavior of the EXO-200 scintillation measurements; a novel algorithm for denoising such signals; and results from denoised EXO-200 data will be presented, showing an improved $\beta\beta0\nu$ limit in Xenon-136. Since this scheme is still in its infancy, possible future improvements will be described throughout, along with discussion of motivations for these improvements.

SIGNAL DENOISING FOR EXO-200 AND AN IMPROVED
LIMIT ON NEUTRINOLESS DOUBLE-BETA DECAY

by

Clayton G. Davis

Dissertation submitted to the Faculty of the Graduate School of the
University of Maryland, College Park in partial fulfillment
of the requirements for the degree of
Doctor of Philosophy
2014

Advisory Committee:
Professor Carter Hall, Chair/Advisor
Professor Radu Balan
Professor Betsy Beise
Professor Rabindra Mohapatra
Professor Peter Shawhan

© Copyright by
Clayton G. Davis
2014

Preface

If needed.

Foreword

If needed.

Dedication

If needed.

Acknowledgments

Without the help of my colleagues, advisor, friends, family, and my wife, this thesis and the work it embodies would never have happened. I would like to give thanks to the EXO-200 collaboration, which has provided a supportive and stimulating environment for my work and learning over the past four years.

Particular thanks must go to: David Auty, Phil Barbeau, Giorgio Gratta, Steve Herrin, Sam Homiller, Mike Jewell, Tessa Johnson, Tony Johnson, Caio Licciardi, Mike Marino, Dave Moore, Russell Neilson, Igor Ostrovskiy, J.J. Russell, Kevin O'Sullivan, Tony Waite, Josiah Walton, Liangjian Wen, Liang Yang, and of course my advisor Carter Hall. I can honestly say that each one of you directly made the following work possible with your contribution of insight, data, plots, and analysis. Denoising has been a tremendously collaborative effort, and I am grateful that my last project with this group has provided the chance to work with all of you so closely.

Contents

List of Figures	viii
List of Abbreviations	xiii
1 Theory of $\beta\beta0\nu$ Decay	1
1.1 Double-Beta Decay	1
1.2 Neutrinoless Double-Beta Decay	4
1.3 Neutrino Flavor Physics	9
1.4 Particle Physics Constraints	11
1.5 Nuclear Physics Constraints from $\beta\beta0\nu$	14
2 The EXO-200 Detector	21
2.1 Overview of the EXO-200 Detector	21
2.2 Backgrounds to $\beta\beta0\nu$ Decay	27
2.3 Passive Background Rejection	31
2.4 Active Background Rejection	40
2.5 Pulse Amplification and Waveform Readout	42
2.6 Calibration Systems	46
2.7 Summary	50
3 Denoising Theory	51
3.1 Setup	54
3.2 The Signal Model	56
3.2.1 APD Noise	58
3.2.2 APD Signals and Noise	62
3.3 Derivation	66
3.4 Matrix Version	73
3.5 Preconditioning	77
3.6 Solver	80
3.7 Implementation	81
3.8 Denoising in Practice	87
3.9 Future Plans	89
3.9.1 Anticorrelated Cluster Energies	89
3.9.2 Wire Denoising	93

4 Noise Measurements	94
4.1 Mathematical Framework for Noise Correlations	94
4.2 Time Windows of Constant Noise	96
4.3 Algorithm for Measuring Noise	97
4.4 Future Directions with Noise Measurement	97
5 The Lightmap	98
5.1 Four-Dimensional Lightmap	100
5.2 Algorithm Details	102
5.2.1 Event Selection	103
5.2.2 Function Parametrization	106
5.2.3 Convergence and Error Estimation	110
5.3 Implementation for this Analysis	113
5.4 Visualization	115
6 EXO-200 Analysis and Results from Denoising	123
6.1 Simulation	123
6.1.1 Simulation of Particles using GEANT	124
6.1.2 Digitization of Waveforms	128
6.2 Cluster Reconstruction	138
6.2.1 Pulse Finding	138
6.2.2 Pulse Fitting	142
6.2.3 Clustering Pulses into Deposit Sites	144
6.3 Energy Corrections	147
6.3.1 Charge Corrections	148
6.3.2 Light Corrections	152
6.3.3 Rotated Energy Calibration	154
6.3.4 Measurement of Rotated Energy Resolution	158
6.4 Fitting	166
6.5 Results and Physics Reach	177
6.6 Comparison to Results without Denoising	182
6.7 Summary	182
7 Conclusions and Future Plans	183
Bibliography	184

List of Figures

1.1	Feynman diagram for $\beta\beta2\nu$ decay. The reaction products are equivalent to two β decays in succession, but this reaction can sometimes occur even if a single β decay would be energetically forbidden.	2
1.2	Energy diagram of isotopes with atomic mass $A = 136$. The energies ΔE are the binding energies of the atom, compared to the bare masses of the same nuclei. Values are from [2].	3
1.3	Feynman diagram for $\beta\beta0\nu$ decay. A virtual neutrino mediates the exchange. This is only possible if $\bar{\nu}_R$ can oscillate to ν_L , and the interaction that induces this oscillation also generates neutrino mass.	5
1.4	A generic $\beta\beta0\nu$ process, with no assumptions of the underlying mechanism. If $\beta\beta0\nu$ is observed, it requires that this reaction is possible even though it does not strictly imply that the oscillation in figure 1.3 is the cause.	6
1.5	Since $\beta\beta0\nu$ requires that the reaction in Figure 1.4 occurs, we can insert that diagram into this larger one and assert that regardless of the underlying mechanism, $\beta\beta0\nu$ implies an effective neutrino mass generated by $\bar{\nu}\text{-}\nu$ oscillation as a higher-order process.	7
1.6	$\beta\beta0\nu$ half-life limits versus the year of the limit. Colors indicate which isotope is under study. Open circles indicate experiments which have not yet concluded data-taking. Figure from [9], with additional isotopes included, plus a couple of additional points for recent results which you prefered not to include – BUT MAYBE THAT'S MORE TROUBLE THAN IT'S WORTH?	8
1.7	The electron spectrum of Tritium (3H) β decay. The endpoint contains only a small fraction of the total statistics. Figure from [18].	13
1.8	The relationship between the effective Majorana mass $\langle m_{\beta\beta} \rangle$ and other fundamental neutrino quantities: the lightest neutrino mass eigenstate m_{min} , the sum of mass eigenstates $M = \sum m_i$, and the effective single-beta-decay neutrino mass $\langle m_\beta \rangle$. Black (magenta) lines indicate the allowed region for the inverted (normal) hierarchy; red (blue) hatches indicate uncertainty for the inverted (normal) hierarchy due to the unknown CP-violating and Majorana phases δ , α_1 , and α_2 . [24]	16

2.1	A two-dimensional energy spectrum of scintillation and ionization from a testbed liquid xenon experiment under an electric field of 4 kV/cm. The spectrum is from a ^{207}Bi source. Figure reproduced from [36].	22
2.2	Schematic of the inner EXO-200 TPC. Figure reproduced from [34].	24
2.3	Anode collection wires (u-wires) and induction wires (v-wires) from EXO-200. (1) and (5) indicate the wire support frame; (2) indicates the wires themselves, constructed as gangs of three wires; (3) illustrates the attachment between wires and the support frame; (4) shows the return cables from the wires to the data acquisition system. Figure reproduced from [34].	26
2.4	X-ray attenuation lengths in xenon. Compton (incoherent) scattering, pair production, and photoelectric absorption are shown, along with their combined attenuation length; coherent (Rayleigh) scattering is omitted because it produces no observable energy deposit. The vertical axis, in cm^2/g , can be multiplied by the density of the xenon to derive an attenuation factor per unit length. Figure produced by [42].	32
2.5	Wire triplet, read as one channel. Figure from [34].	35
2.6	APDs ganged together (bottom right). Wiring to the front-end electronics are visible as yellow “tape.” Figure from [34].	36
2.7	A cutaway schematic image of the TPC and surrounding materials in the cleanroom. HFE-7000 refrigerant is contained between the cryostat and the LXe vessel. Figure from [34].	37
2.8	Muon flux as a function of depth, in meters water equivalent. The WIPP site is indicated in relation to other underground science facilities. Figure from [45].	39
2.9	A cross-sectional schematic of an APD is shown in (a). The electric field as a function of depth is shown in (b). Figure from [46].	43
2.10	A guide tube permits gamma sources to be inserted to known locations near the TPC. Green dots indicate a few of the locations where the source may conventionally be placed. Figure from [34].	47
3.1	Coherent and incoherent noise power spectra for a sample set of APD channels without signal shaping. [52]	52
3.2	Shaped and unshaped APD waveforms. The normalization is shown to make the peak of the shaped waveform have a magnitude of one, and the time axis is shifted so that the unshaped waveform is a step function centered at $t = 0$	57
5.1	Lightmap position-dependence $R(\vec{x})$ for selected APD gangs.	115
5.2	Lightmap position-dependence $R(\vec{x})$ for selected APD gangs. Here extreme anode positions are omitted to permit better contrast for the lightmap in the fiducial volume.	116
5.3	Functions $S(t)$ for selected channels.	117
5.4	Functions $S(t)$ for selected channels.	118

5.5	Functions $S(t)$ for selected channels.	119
6.1	The GEANT simulation includes large-scale features of the EXO-200 detector, including the outer and inner lead wall (black), outer and inner cryostat and TPC legs (red), and the TPC itself (brown). Components are assembled from simple geometrical shapes, and distant objects are only described coarsely. [49]	125
6.2	Detector components which are close to the liquid xenon are simulated in GEANT with far greater accuracy than distant objects, to reduce computational time. [49]	126
6.3	Energy spectra from ^{238}U in the TPC vessel; single-site and multi-site energy spectra are shown separately. [49]	129
6.4	Energy spectra from ^{232}Th in the TPC vessel; single-site and multi-site energy spectra are shown separately. [49]	130
6.5	The wire planes are modeled in only two dimensions; charge drifts along the field lines, which are arranged to terminate only on the u-wires. [49]	132
6.6	Weight potential of a u-wire channel consisting of three ganged wires. Electric field lines are superimposed. [49]	134
6.7	Weight potential of a v-wire channel consisting of three ganged wires. Electric field lines are superimposed. [49]	135
6.8	Comparison between simulated and observed waveforms on a u-wire (left) and v-wire (right) from ^{228}Th sources. The events are chosen to have similar energies so that the magnitudes match. [49]	136
6.9	Comparison between simulated and observed energy spectra (a) and standoff distance (b) in single-site ^{226}Ra events from a source located at position S5. [35]	137
6.10	A u-wire waveform (left) and the output from operation of the matched filter (right). The red line on the right indicates our signal threshold; the matched filter output exceeds the threshold, so this waveform is determined to contain a signal. [50]	140
6.11	A u-wire waveform composed of two signals near in time is shown (top left); the matched filter (top right) correctly detects the presence of signal, but does not detect the presence of two distinct signals. At bottom left, the waveform is unshaped; at bottom right the waveform is reshaped with shorter differentiation times, leading to easier detection. [50]	141
6.12	Fits to data for a u-wire (top left), v-wire (top right), and summed-APD waveform (bottom). The red model line indicates the time extent of the fit window. [50]	143
6.13	The purity charge correction is measured by fitting the 2615-keV ^{208}Tl gamma line as a function of Z-position. [71]	149
6.14	The expected grid correction of a u-wire as a function of Z-position. In this plot, $Z = 6$ mm represents the position of the u-wire plane and $Z = 12$ mm is the position of the v-wire plane. [48]	150

6.15 After applying all charge corrections, we find that the 2615-keV ^{208}Tl ionization peak is observed at the expected location for single-wire events; however, for two-wire events a residual bias is observed which also exhibits Z-dependence. [71]	151
6.16 A residual calibration offset and Z-dependent behavior is observed in the denoised scintillation measurements. The top plots show the relative peak position of the scintillation-only 2615-keV ^{208}Tl peak (one-wire and two-wire) and average alpha energy from ^{222}Rn versus Z (top left) and R (top right). The bottom plot shows the absolute denoised scintillation energy from the 2615-keV ^{208}Tl peak for one and two wires, with the measured correction function overlaid. [71] . .	153
6.17 Corrected scintillation versus charge energy are shown for a thorium run. The projection angle for the rotated energy measurement is illustrated at the 2615-keV peak; the projection onto a calibrated axis is shown. Figure provided by Liangjian Wen.	156
6.18 Charge-only, scintillation-only, and rotated energy spectra are shown from a thorium source run; the significant improvement in energy resolution with the rotated energy measurement is apparent, as are low-energy features which are washed out in the lower-resolution spectra. The dotted red line indicates the diagonal cut described in section 6.4. Figure provided by Liangjian Wen.	157
6.19 The resolution functions (top) and relative resolution functions (bottom) are compared for denoised and undenoised data.	160
6.20 Time dependence of the single-site energy resolution at 2615 keV with denoised (blue) and undenoised (red) scintillation. The denoised energy resolution at the $\beta\beta0\nu$ Q -value is estimated (open square) from the time-dependent energy resolution measured with thorium data combined with the time-independent shape of the average resolution function. [35]	163
6.21 The single-site (left) and multi-site (right) gamma line at 2.2 MeV from neutron capture on hydrogen can be used as a low-background cross-check on the resolution calibration. [71]	164
6.22 The low-background potassium peak at 1461 keV is used as a cross-check on the single-site (left) and multi-site (right) energy calibrations. Fits also include the nearby 1332-keV cobalt peak. [71]	165
6.23 The X-Y fiducial cuts applied to the data do not include the entire active volume; however, for the $\beta\beta0\nu$ search we find that aggressive fiducial cuts optimize our sensitivity.	167
6.24 Vetoing events coincident with muons can reduce our 1σ and 2σ event counts. Figure provided by David Auty.	168
6.25 The fit provides constraints on the beta-scale. Figure provided by Liangjian Wen.	173

- 6.26 Energy spectra with best-fit pdfs for single-site (top) and multi-site (bottom). Residuals between data and the combined pdfs are shown below the spectra. The last bin of the spectra is an overflow bin. The 2σ region of interest around the Q -value is shown on the single-site spectrum. Insets for single-site and multi-site zoom around the Q -value. The simultaneous standoff-distance fit is not shown. [35] . . . 175
- 6.27 The positions of events in the 1σ region of interest (red) and wider energy range $2325 - 2550$ keV (black) are shown projected onto their X-Y (left) and R^2 -Z (right) coordinates. Lines indicate the fiducial volume, with the dotted lines indicating the fiducial cut away from the cathod that is not used as a component to the standoff distance observable. Figure provided by Dave Moore. 176
- 6.28 Profile scan of negative log-likelihood as a function of the number of fit $\beta\beta0\nu$ counts. [35] 177
- 6.29 Assuming that the background measurements of EXO-200 from this analysis are accurate, toy datasets are simulated. The top plot shows the probability distribution of our 90% confidence limit; we find that our median upper limit is 14.04 counts attributed to $\beta\beta0\nu$, compared to our observed upper limit of 23.92 counts. The bottom plot shows the probability distribution of our ability to reject the null hypothesis (no $\beta\beta0\nu$) based on the negative log-likelihood; we find that the present dataset rejects the null hypothesis with probability less than 90%. Figures provided by Ryan Killick. 178
- 6.30 $\beta\beta0\nu$ constraints are shown from ^{136}Xe (horizontal) and ^{76}Ge (vertical). The four diagonal lines represent four recent matrix element computations [76–79] and one recent phase-space factor [22] relating the two half-lives; tick marks along the diagonal represent the corresponding mass $\langle m_{\beta\beta} \rangle$. 90% confidence limits and median 90% sensitivities are shown for the KamLand-Zen [31], GERDA [26], and EXO-200 experiments [35]; the claimed 2006 discovery by Klapdor-Kleingrothaus and Krivosheina is shown as a 1σ confidence interval. [80] 180

List of Abbreviations

EXO	Enriched Xenon Observatory (family of current or planned detectors)
EXO-200	Current (200-kg) iteration of the EXO family of detectors
nEXO	Planned next-generation EXO detector
APD	Avalanche Photo-diode
ADC	Analog-Digital Converter, or one of its discrete output units
DAQ	Data Acquisition System
TPC	Time Projection Chamber
WIPP	Waste Isolation Pilot Plant
PDF	Probability Distribution Function

Chapter 1: Theory of $\beta\beta0\nu$ Decay

1.1 Double-Beta Decay

Standard-model double beta ($\beta\beta$) decay is the result of the particle interaction



mediated by W^- -exchange, as depicted in Figure 1.1. It is effectively the simultaneous occurrence of two beta (β) decays from the same nucleus.

$\beta\beta$ decay is the result of a second-order weak interaction, so it has a remarkably slow rate compared to most β decay processes. As a result, although many nuclei are expected to decay by $\beta\beta$, the process is thoroughly masked by conventional β decay in most of them. We can only hope to detect $\beta\beta$ decay in isotopes where β decay is forbidden or highly suppressed.

In rare cases, β decay may be highly suppressed, enabling $\beta\beta$ decay to have a rate comparable to or exceeding single- β decay. This is, for example, the case in $^{48}_{20}\text{Ca}$: the ground state of $^{48}_{20}\text{Ca}$ has zero units of angular momentum, whereas its single- β -decay daughter product $^{48}_{21}\text{Sc}$ has six units of total angular momentum in its ground state. This β decay is thus highly suppressed by angular momentum

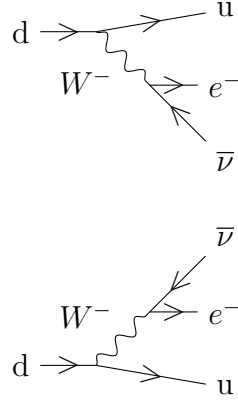


Figure 1.1: Feynman diagram for $\beta\beta 2\nu$ decay. The reaction products are equivalent to two β decays in succession, but this reaction can sometimes occur even if a single β decay would be energetically forbidden.

conservation. By contrast, $^{48}_{22}\text{Ti}$ has zero units of total angular momentum, making $\beta\beta$ decay of $^{48}_{20}\text{Ca}$ permitted by angular momentum considerations, and as a result the $\beta\beta$ decay mode of $^{48}_{20}\text{Ca}$ dominates. [1]

However, in most cases of interest β decay is forbidden by energy conservation. It is well-known that nuclei minimize their energy by arranging similar nucleons to have overlapping wavefunctions. [1] Thus, isotopes with an even number of protons and an even number of neutrons will have less nucleon-pairing potential energy than an isotope with either an odd number of protons or an odd number of neutrons, which in turn will have less nucleon-pairing potential energy than an isotope with an odd number of protons and an odd number of electrons.

A typical nuclear energy level diagram is shown in figure 1.2 for the $A = 136$ isobar: Xenon, Barium, Cerium, and Neodynium are even-even isotopes, and have systematically lower energies than the odd-odd isotopes Iodine, Cesium, Lanthanum,

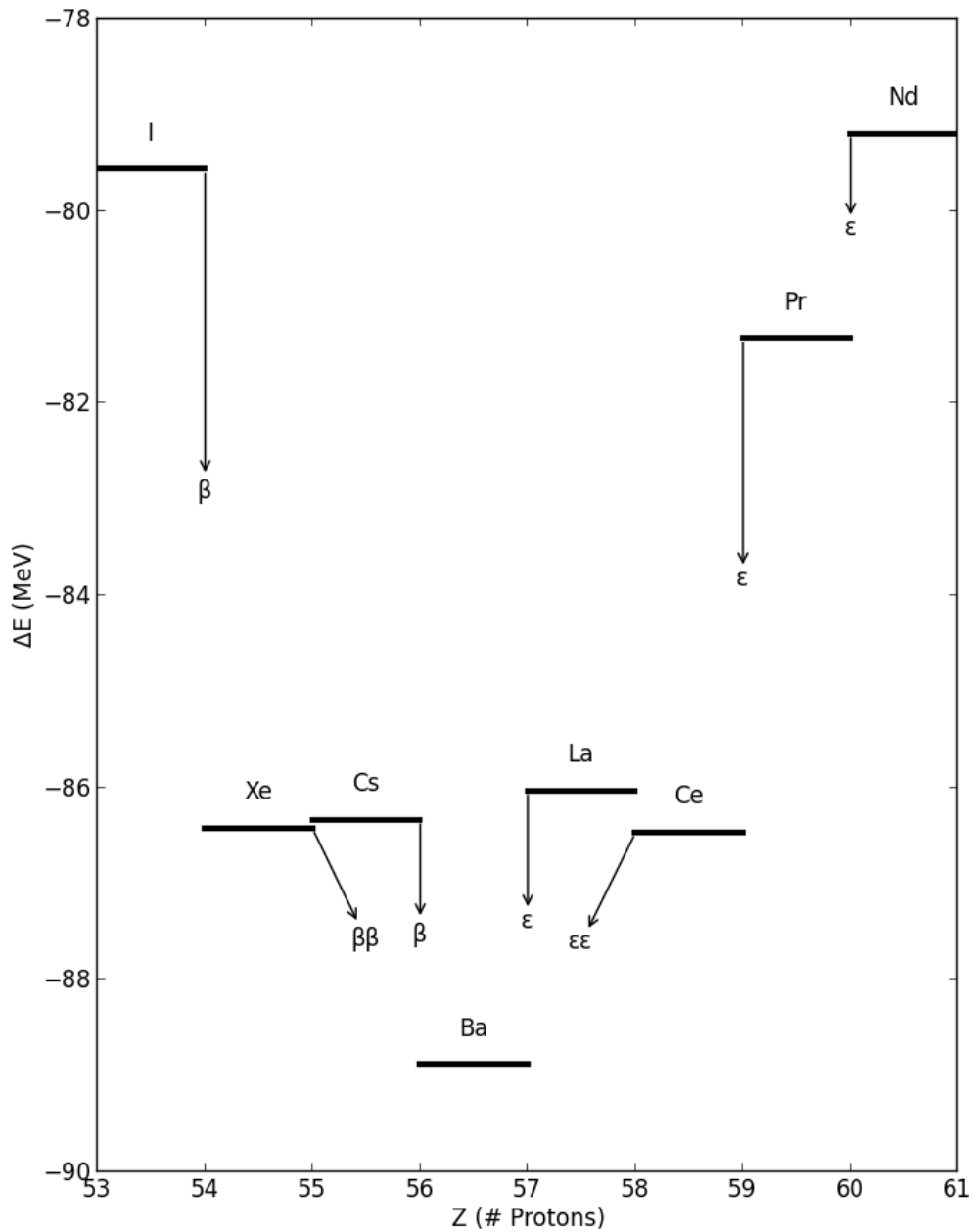


Figure 1.2: Energy diagram of isotopes with atomic mass $A = 136$. The energies ΔE are the binding energies of the atom, compared to the bare masses of the same nuclei. Values are from [2].

and Praseodymium. For this particular isobar, we can see that Xenon is energetically forbidden from single- β decaying to Cesium because the odd-odd isotope of Cesium has just slightly more potential energy than the even-even isotope of Xenon; as a result, the primary mode of decay of Xenon-136 will be by $\beta\beta$ decay to Barium-136. (We also note a similar feature, that the primary mode of decay of Cerium-136 will be by double-electron-capture ($\epsilon\epsilon$) to Barium-136. Many of the same implications of $\beta\beta$ decay also apply to $\epsilon\epsilon$ decay; however, in practice the rates for these decays will be lower than the rates for $\beta\beta$ decay, so we will not consider them further in this work.)

1.2 Neutrinoless Double-Beta Decay

The detection and study of $\beta\beta$ decay provides an opportunity to test a new class of nuclear matrix computations; however, it does not violate any fundamental symmetries and is, in this sense, a mundane prediction of the Standard Model. The primary appeal of $\beta\beta$ decay is through the opportunity it provides to probe the nature of neutrinos.

It has been suggested as early as 1937 that neutrinos could possess mass through a neutrino-antineutrino interaction, provided that the neutrino is its own antiparticle [3]. The theorized Majorana interaction comes from Lagrangian terms

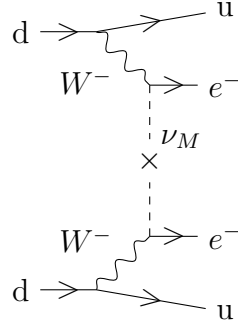


Figure 1.3: Feynman diagram for $\beta\beta 0\nu$ decay. A virtual neutrino mediates the exchange. This is only possible if $\bar{\nu}_R$ can oscillate to ν_L , and the interaction that induces this oscillation also generates neutrino mass.

of the form (for each of three neutrino eigenstates)

$$\begin{aligned}\mathcal{L}_{Maj} = & - \frac{m_L}{2} (\overline{\Psi}_L^c \Psi_L + \overline{\Psi}_L \Psi_L^c) \\ & - \frac{m_R}{2} (\overline{\Psi}_R^c \Psi_R + \overline{\Psi}_R \Psi_R^c),\end{aligned}\quad (1.2)$$

where the superscript- c represents charge conjugation. (This is the reason that Majorana mass terms are only possible for a chargeless lepton.) The masses m_L and m_R may be tuned independently; since there has never been an observation of right-handed neutrinos or left-handed anti-neutrinos, it is possible that $m_R = 0$ and that the fields Ψ_R and Ψ_R^c do not exist in nature [4].

If neutrinos do have Majorana mass interactions, then any isotope that undergoes $\beta\beta$ decay can also undergo the related process $2d \rightarrow 2u + 2e^-$, depicted in Figure 1.3, in which the two outgoing neutrinos in $\beta\beta$ decay are replaced by one virtual neutrino. We can interpret this as a mixing interaction between a left-handed neutrino and a right-handed antineutrino; this is only possible if neutrinos

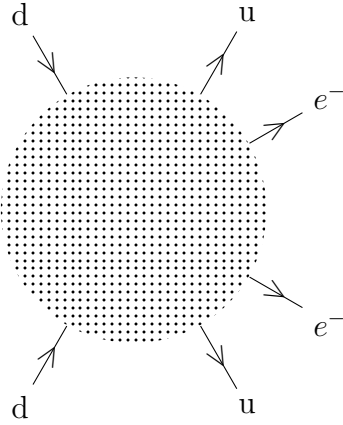


Figure 1.4: A generic $\beta\beta0\nu$ process, with no assumptions of the underlying mechanism. If $\beta\beta0\nu$ is observed, it requires that this reaction is possible even though it does not strictly imply that the oscillation in figure 1.3 is the cause.

are Majorana particles. We refer to the standard process as two-neutrino double beta ($\beta\beta2\nu$) decay and the novel process as neutrinoless double beta ($\beta\beta0\nu$) decay.

The tree-level diagram for $\beta\beta0\nu$ has one additional interaction vertex compared to $\beta\beta2\nu$ decay, and as a result we would expect it to occur at an even slower rate. However, the more immediate consequence of $\beta\beta0\nu$ decay is that lepton number conservation would be violated. The lepton number changes by two units corresponding to the creation of two leptons with no balancing anti-leptons. Numerous theories have suggested other plausible modes of lepton number non-conservation [5, 6], but none have yet reported a positive result. In the conventional Standard Model with massless neutrinos, lepton number conservation is an accidental symmetry [7], but in a model with massive neutrinos there may no longer be any reason *a priori* to expect conservation or non-conservation of lepton number.

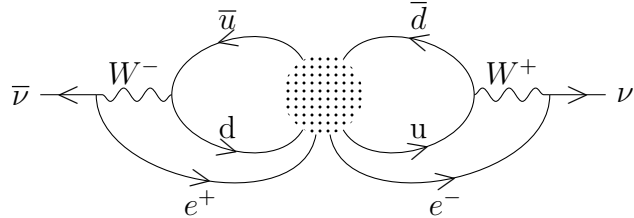


Figure 1.5: Since $\beta\beta0\nu$ requires that the reaction in Figure 1.4 occurs, we can insert that diagram into this larger one and assert that regardless of the underlying mechanism, $\beta\beta0\nu$ implies an effective neutrino mass generated by $\bar{\nu}\text{-}\nu$ oscillation as a higher-order process.

It is worth noting that the interaction term above assumes no mediating particles in the mechanism, whereas it is possible that $\beta\beta0\nu$ could be mediated by some higher-order interaction terms. However, if $\beta\beta0\nu$ decay is observed, it leads very generally to a conclusion that neutrinos have an *effective* Majorana mass interaction [8]. We can see this by examining the generic diagram for $\beta\beta0\nu$ decay in figure 1.4. No matter what the mechanism of the decay is, we can insert this diagram into figure 1.5 and see that an effective neutrino-antineutrino mass vertex is implied by the existence of $\beta\beta0\nu$ decay.

It has long been clear that appealing extensions to the Standard Model can be built around neutrinos with Majorana mass; see eg. the introduction in 1980 of the see-saw mechanism in [10], where the naturalness of the neutrino mass scale is addressed by hypothesizing m_R is inversely related to m_L and $m_L \ll m_R$. The motivation to search for $\beta\beta0\nu$ decay became stronger when neutrinos were proven to have mass, particularly by the definitive proof of the oscillation of atmospheric

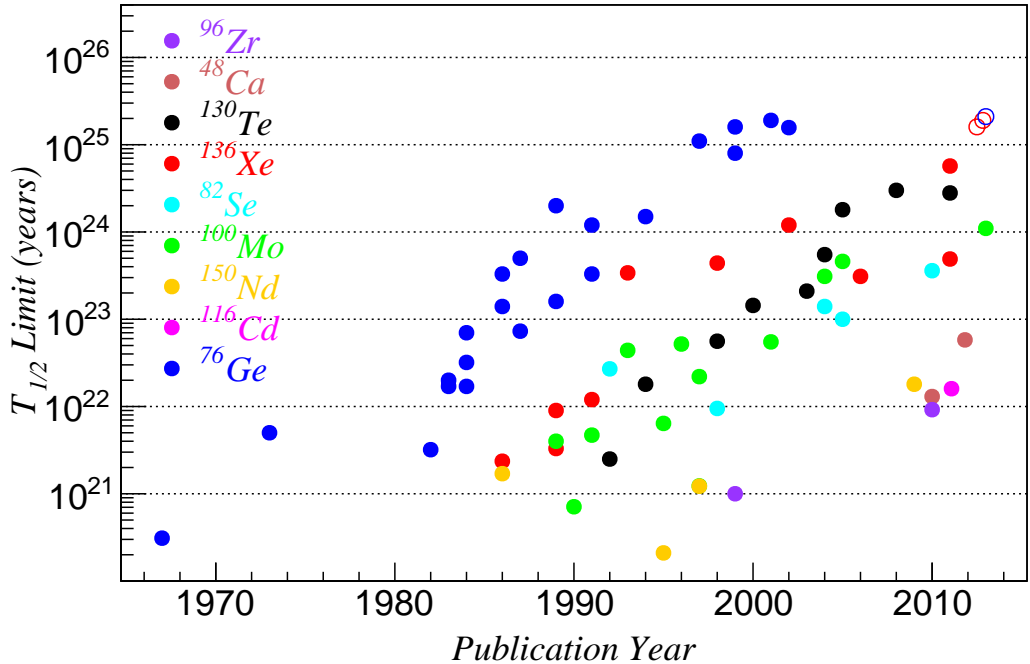


Figure 1.6: $\beta\beta0\nu$ half-life limits versus the year of the limit. Colors indicate which isotope is under study. Open circles indicate experiments which have not yet concluded data-taking. Figure from [9], with additional isotopes included, plus a couple of additional points for recent results which you prefered not to include – BUT MAYBE THAT'S MORE TROUBLE THAN IT'S WORTH?.

neutrinos in [11]. As a result, the number of experiments searching for $\beta\beta$ decays exploded during this time period; figure 1.6 shows a collection of $\beta\beta0\nu$ half-life limits obtained versus year, colored by the isotope under study. The search for $\beta\beta0\nu$ has by now evolved into a highly competitive field, in which the isotopes ^{130}Te , ^{76}Ge , and ^{136}Xe are particularly dominant but searches are also being actively pursued in many other isotopes.

1.3 Neutrino Flavor Physics

Neutrinos are known to come in three flavors, or eigenstates which are diagonal with respect to the lepton interaction terms of the Standard Model. These flavors are ν_e , ν_μ , and ν_τ ; they interact, respectively, with e , μ , and τ leptons. We can hypothesize that neutrinos may also have a basis diagonalized with respect to rest mass which may not be identical to the flavor basis, and call the mass eigenstates ν_1 , ν_2 , and ν_3 with respective masses m_1 , m_2 , and m_3 . The unitary operator which translates between the two bases is specified by:

$$\begin{pmatrix} \nu_e \\ \nu_\mu \\ \nu_\tau \end{pmatrix} = \mathbf{U} \begin{pmatrix} \nu_1 \\ \nu_2 \\ \nu_3 \end{pmatrix} = \begin{pmatrix} U_{e1} & U_{e2} & U_{e3} \\ U_{\mu 1} & U_{\mu 2} & U_{\mu 3} \\ U_{\tau 1} & U_{\tau 2} & U_{\tau 3} \end{pmatrix} \begin{pmatrix} \nu_1 \\ \nu_2 \\ \nu_3 \end{pmatrix}. \quad (1.3)$$

These formalities are uninteresting if the neutrino sector is massless, since the mass eigenstates are degenerate. However, in the case where neutrinos are massive, we can see that neutrinos which are created in one flavor eigenstate will oscillate between the flavor eigenstates with a period which depends on the differences be-

tween masses, as is typical in an N-state quantum system. In the neutrino sector, we can more specifically state that the probability for a transition from flavor α to flavor β will be: [12]

$$P_{\alpha\beta} = \delta_{\alpha\beta} - 4 \sum_{i=1}^2 \sum_{j=i+1}^3 \text{Re} [U_{\alpha i} U_{\beta i}^* U_{\alpha j}^* U_{\beta j}] \sin^2 \left(\frac{[m_i^2 - m_j^2] L}{4E} \right) \quad (1.4)$$

where L is the distance (or time, in $c = 1$ units) between neutrino source and destination, and E is the relativistic energy of the emitted neutrinos.

The transition probability is sensitive to the masses of the neutrinos, but only in the form $|m_i^2 - m_j^2|$. These measurements have now been performed in a variety of neutrino oscillation experiments, and the best current constraints are $|m_1^2 - m_2^2| = (7.50 \pm 0.20) \cdot 10^{-5} \text{eV}^2$ [13] and $|m_2^2 - m_3^2| = 2.32_{-0.08}^{+0.12} \cdot 10^{-3} \text{eV}^2$ [14].

However, oscillation experiments cannot constrain the overall mass scale of neutrinos; they can only set a conservative lower limit that $\max(m_2, m_3) \geq 0.048$ eV if we assume one of m_2 or m_3 is zero. Furthermore, they do not establish the sign of the difference. We can see that m_1 and m_2 are fairly close together, and m_3 is significantly different; but we cannot see whether m_3 is larger or smaller than the other two masses. We refer to the situation with $m_1 \simeq m_2 \ll m_3$ as the normal hierarchy, and $m_3 \ll m_1 \simeq m_2$ as the inverted hierarchy; the regime where $m_1 \simeq m_2 \simeq m_3 \gg |m_2^2 - m_3^2|$ is called the degenerate region. Distinguishing between these three situations is one of the significant open questions in neutrino physics because of its impact on observable quantities.

1.4 Particle Physics Constraints

To produce more detailed constraints on neutrino physics, it is generally useful to provide a parametrization of the mixing matrix \mathbf{U} from equation 1.3. The standard parametrization is:

$$\begin{aligned} \mathbf{U} &= \begin{pmatrix} U_{e1} & U_{e2} & U_{e3} \\ U_{\mu 1} & U_{\mu 2} & U_{\mu 3} \\ U_{\tau 1} & U_{\tau 2} & U_{\tau 3} \end{pmatrix} \\ &= \begin{pmatrix} 1 & 0 & 0 \\ 0 & \cos(\theta_{23}) & \sin(\theta_{23}) \\ 0 & -\sin(\theta_{23}) & \cos(\theta_{23}) \end{pmatrix} \begin{pmatrix} \cos(\theta_{13}) & 0 & \sin(\theta_{13})e^{-i\delta} \\ 0 & 1 & 0 \\ -\sin(\theta_{13})e^{i\delta} & 0 & \cos(\theta_{13}) \end{pmatrix} \times \quad (1.5) \\ &\quad \begin{pmatrix} \cos(\theta_{12}) & \sin(\theta_{12}) & 0 \\ -\sin(\theta_{12}) & \cos(\theta_{12}) & 0 \\ 0 & 0 & 1 \end{pmatrix} \begin{pmatrix} e^{i\alpha_1/2} & 0 & 0 \\ 0 & e^{i\alpha_2/2} & 0 \\ 0 & 0 & 1 \end{pmatrix}. \end{aligned}$$

Out of the six parameters used in defining this matrix, the only ones which have been measured are the three mixing angles $\sin^2(2\theta_{12}) = 0.857^{+0.023}_{-0.025}$ [13], $\sin^2(2\theta_{13}) = 0.089 \pm 0.010(\text{stat}) \pm 0.005(\text{sys})$ [15], and $\sin^2(2\theta_{23}) > 0.95$ [16]. The Dirac phase δ is in principle observable from oscillation experiments, but no current experiments have achieved the sensitivity necessary to accomplish this. The Majorana phases α_1 and α_2 cannot be extracted from neutrino oscillations. [4]

The sum of the three mass eigenstates, $M = \sum m_i$, can be constrained by cosmological observations. This constraint (like all cosmologically-based constraints)

will be model-dependent; it relies on the expectation that low-mass, hot forms of dark matter similar to neutrinos promote the formation of large-scale structures in the early universe by allowing extremely remote regions of matter to remain in thermal equilibrium. Recent results from Planck combined with WMAP and baryon acoustic oscillations have restricted $M < 0.230$ eV with 95% confidence. [17] Considering the assertion in section 1.3 that the heaviest neutrino must have a mass no less than 0.048eV, we can see that this cosmological constraint pushes M to within a factor of five of its lower limit; taken at face value, the Planck measurement is the strongest existing constraint on the absolute mass scale of neutrinos.

Closer to home, the mass of neutrinos is also reflected in β decay, $d^- > u + e^- + \bar{\nu}_e$. The total energy of the daughter products is known, and will be shared between the electron and antineutrino; the minimum energy of the antineutrino will be its rest mass, so by searching for the maximum energy of the electron we can simultaneously measure the rest mass of the neutrino. The electron anti-neutrino emitted from beta decay has a mix of all three mass eigenstates; since no current or planned experiment has sufficiently good energy resolution to resolve the separate endpoints from the three neutrino masses, we can instead write an effective rest mass of an electron antineutrino as: [4]

$$\langle m_\beta \rangle^2 = \sum_i m_i^2 |U_{ei}|^2. \quad (1.6)$$

Attempts to measure $\langle m_\beta \rangle$ require experiments to measure the electron energy spectrum of beta decays at the endpoint, which is complicated by the fact that this portion of the electron spectrum contains only a small fraction of the total electron

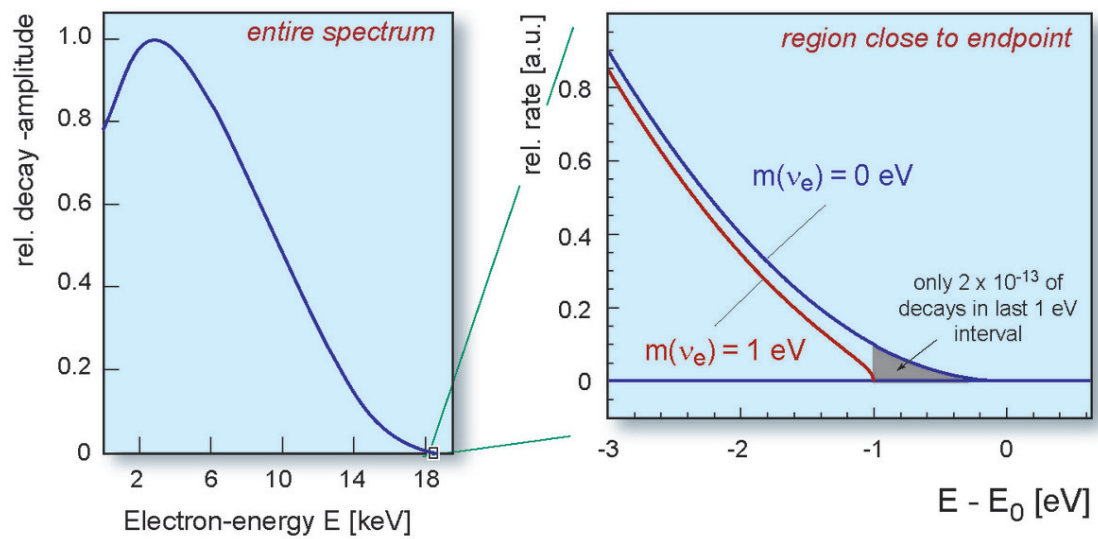


Figure 1.7: The electron spectrum of Tritium (3H) β decay. The endpoint contains only a small fraction of the total statistics. Figure from [18].

statistics. Tritium (3H) is commonly used for these experiments because it has a medium-length halflife of 12.3 years and an extremely low β decay endpoint energy of 18.6 keV, which maximizes the relative shift in endpoint energy due to $\langle m_\beta \rangle$. Figure 1.7 shows that for $\langle m_\beta \rangle = 1\text{eV}$ in Tritium, experiments must observe a shift in the spectrum which affects only about one decay in $5 \cdot 10^{12}$, making this level of sensitivity extremely difficult to achieve. The best existing limit from β decay is $\langle m_\beta \rangle < 2.05 \text{ eV}$, with 95% confidence, from the Troitsk experiment which ran from 1994 to 2004. [19] The KATRIN experiment hopes to achieve a sensitivity of 0.2 eV, and is expected to begin taking data in 2015. [20, 21]

1.5 Nuclear Physics Constraints from $\beta\beta0\nu$

If the mechanism of $\beta\beta0\nu$ decay really is, at tree level, a neutrino mass term as shown in figure 1.3, then the rate of $\beta\beta0\nu$ decay will also reflect the magnitude of the neutrino mass parameters. We can write the partial half-life of an isotope which undergoes $\beta\beta0\nu$ decay as

$$[T_{1/2}^{0\nu}]^{-1} = G_{0\nu}(Q_{\beta\beta}, Z) |M_{0\nu}|^2 \langle m_{\beta\beta} \rangle^2, \quad (1.7)$$

where $G_{0\nu}(Q_{\beta\beta}, Z)$ is a phase-space factor coming from the range of possible output states, $M_{0\nu}$ is a nuclear matrix element, and the last factor is the effective $\beta\beta$ neutrino mass, defined as:

$$\langle m_{\beta\beta} \rangle = \left| \sum_k m_k U_{ek}^2 \right|. \quad (1.8)$$

The phase-space factor $G_{0\nu}(Q_{\beta\beta}, Z)$ is difficult to compute exactly due to

nuclear effects; for a recent computation, see [22] which estimates errors of 7% dominated by uncertainty in the nuclear radius. Its main feature is that it scales roughly like $Q_{\beta\beta}^5$, the fifth power of the decay energy. As a result, using $\beta\beta$ isotopes with high Q -values confers a significant advantage in neutrino mass sensitivity.

The dominant uncertainty in translating $\beta\beta0\nu$ half-life limits into $\langle m_{\beta\beta} \rangle$ constraints comes from our knowledge of the matrix elements $M_{0\nu}$, which can have uncertainties as large as a factor of 2 – 3. [4] Calculations which attempt to estimate these values rely on a variety of matrix models, but often rely on approximations of some sort to make the calculations tractable. Efforts to improve the accuracy of these values include a combination of more precise computations and experimental feedback to improve the accuracy of these models. See [23] for more discussion of attempts to improve this situation.

Unlike $\langle m_\beta \rangle$, which is an incoherent sum of strictly positive terms in equation 1.6, we can see that $\langle m_{\beta\beta} \rangle$ is a coherent sum of terms, each of which may have arbitrary complex phase which may increase or decrease the result of equation 1.8. In other words it is possible, even if neutrinos do have Majorana mass, for $\langle m_{\beta\beta} \rangle$ to be arbitrarily small if \mathbf{U} is tuned to produce cancellations between terms.

It is possible to relate the observables $\langle m_{\beta\beta} \rangle$, $\langle m_\beta \rangle$, and M within the model for \mathbf{U} of equation 1.5. These relations are shown in figure 1.8; we recall from section 1.4 that beta spectrum measurements constrain $\langle m_\beta \rangle < 2.05$ eV and cosmological observations constrain $M < 0.230$ eV, both with 90% confidence. The strongest constraints on $\langle m_{\beta\beta} \rangle$ from $\beta\beta0\nu$ searches place $\langle m_{\beta\beta} \rangle < 0.15 - 0.4$ eV, depending on the choice of matrix element calculations. We can see that if the cosmological

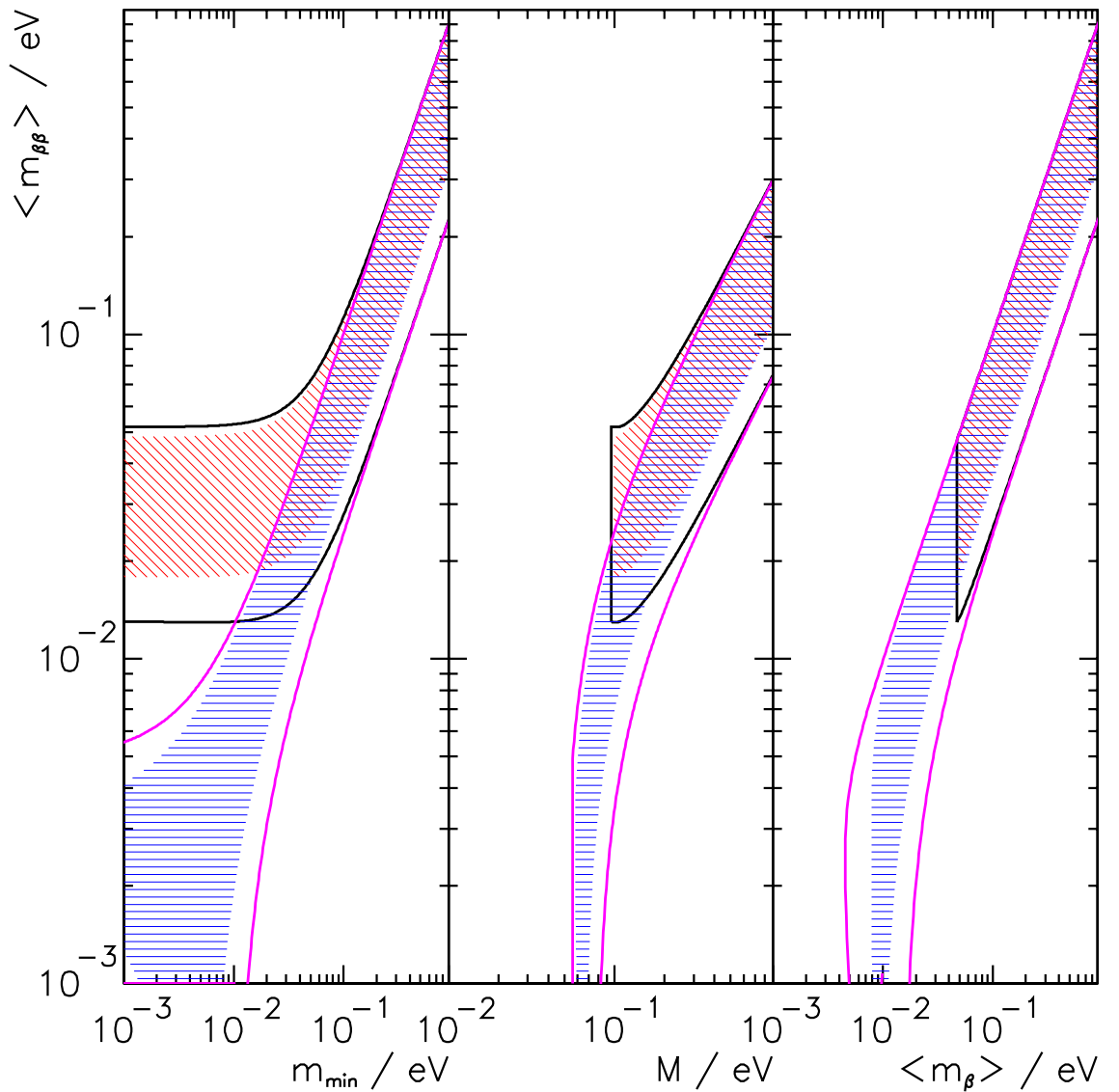


Figure 1.8: The relationship between the effective Majorana mass $\langle m_{\beta\beta} \rangle$ and other fundamental neutrino quantities: the lightest neutrino mass eigenstate m_{min} , the sum of mass eigenstates $M = \sum m_i$, and the effective single-beta-decay neutrino mass $\langle m_\beta \rangle$. Black (magenta) lines indicate the allowed region for the inverted (normal) hierarchy; red (blue) hatches indicate uncertainty for the inverted (normal) hierarchy due to the unknown CP-violating and Majorana phases δ , α_1 , and α_2 . [24]

limits are to be trusted, they provide the strongest constraints on the neutrino mass parameters; however, all three observables are being probed competitively, and the wide range of experimental approaches means that systematic effects are unlikely to be shared by all three methods.

The sensitivity of an experiment for measuring $T_{1/2}^{0\nu}$ can be described by the approximate formula: [4]

$$T_{1/2}^{0\nu}(n_\sigma) = \frac{4.16 \cdot 10^{26} \text{ yrs}}{n_\sigma} \left(\frac{\epsilon a}{W} \right) \sqrt{\frac{Mt}{b\Delta E}}, \quad (1.9)$$

where M is the mass of material, a is the isotopic enrichment, W is the molecular mass of the material in atomic units, and t is the live-time of the experiment; ϵ is the signal efficiency, b is the background rate (in counts per kg keV year, or some similar units), and ΔE is the energy resolution of the detector at the Q -value; and n_σ is the desired confidence limit, in sigmas, where the standard 90% confidence limit will require $n_\sigma = 1.64$. The scaling of this equation is most accurate when the energy resolution is much smaller than the Q -value and the background is uniformly distributed in energy; however as a rough guide it, combined with phase factor and matrix element estimates, allows us to compare the relative strengths of different $\beta\beta$ experiments.

What it tells us, broadly, is that we should prefer experiments for which:

- A large quantity of highly-enriched isotope can be obtained.
- Signal detection is highly efficient.
- Background contamination around the Q -value is small, and does not scale

with detector mass.

- Good energy resolution can be achieved.

Currently the leading choices of materials for $\beta\beta$ searches are: [4]

^{76}Ge has by far the best energy resolution of any material, around 3 keV. It is also possible to grow Germanium crystals with fairly low background, with 0.06 counts/(kg keV year) having been demonstrated. However, it is difficult to grow large, clean crystals of Germanium, and as a result it may not be a scalable material. It also has a Q -value of only 2039 keV, giving it one of the lowest phase factors among the popular isotopes. GERDA is currently the leading experiment, with data-taking underway.

^{130}Te also has an excellent energy resolution around 7 keV. Its Q -value is also higher than ^{76}Ge , at 2530 keV. TeO_2 crystals must be grown, though, so it may suffer from some of the same challenges of scalability as Germanium. The CUORE experiment is expected to begin data-taking in 2014.

^{136}Xe has a comparatively poor energy resolution around 35 – 40 keV. However, Xenon stands out for its scalability: it is easy to enrich in centrifuges, easy to purify chemically due to its status as a noble element, and it is easy to construct large monolithic detectors because it can be used in a liquid or gaseous state. Background rates of $1 - 2 \cdot 10^{-3}$ counts/(kg keV year) have been demonstrated. There are currently two leading experiments. KamLAND-Zen is the larger experiment, containing 180 kg of active ^{136}Xe ; however, it detects

only scintillation, and as a result its resolution is roughly 100 keV. EXO-200 only contains roughly 80 kg of active ^{136}Xe , but it detects energy through both the scintillation and ionization modes, and as a result is able to achieve energy resolutions around $35 - 40$ keV.

Table 1.1 tabulates the most current $T_{1/2}^{0\nu}$ limits in all $\beta\beta$ isotopes for which $\beta\beta0\nu$ limits have been published. Representative limits on $\langle m_{\beta\beta} \rangle$ are also included; these come from one particular set of phase space factors and nuclear matrix element calculations chosen because they have been tabulated for a broad range of isotopes and permit comparisons across all available half-life limits. [22,33] However, it should be remembered that errors in the matrix elements may propagate to errors in $\langle m_{\beta\beta} \rangle$ of as much as a factor of two for each isotope. We can see that although there are favoured isotopes, active and successful programs exist in a wide range of isotopes.

As the table indicates, ^{136}Xe has provided some of the strongest constraints on $\langle m_{\beta\beta} \rangle$ in spite of its relatively poor energy resolution. The present work will demonstrate that it is possible, in the EXO-200 detector, to produce significant improvements to the energy resolution through offline denoising of the scintillation signals. This denoising technique will be applied to data from the detector, and will result in a stronger limit on $T_{1/2}^{0\nu}$ from EXO-200 than could be obtained from the same data without denoising. Recent results will be presented which benefit from this and other improvements, as well as increased livetime.

Isotope	$T_{1/2}^{0\nu}$ (years, 90% CL)	$\langle m_{\beta\beta} \rangle$ (eV, 90% CL)	Collaboration
^{48}Ca	$5.8 \cdot 10^{22}$	3.7	ELEGANT IV [25]
^{76}Ge	$2.1 \cdot 10^{25}$	0.24	GERDA [26]
^{82}Se	$3.6 \cdot 10^{23}$	1.1	NEMO-3 [27]
^{96}Zr	$9.2 \cdot 10^{21}$	8.0	NEMO-3 [28]
^{100}Mo	$1.1 \cdot 10^{24}$	0.56	NEMO-3 [29]
^{116}Cd	$1.6 \cdot 10^{22}$	6.1	NEMO-3 [27]
^{130}Te	$3.0 \cdot 10^{24}$	0.34	Cuoricino [30]
^{136}Xe	FILL IN		
^{136}Xe	$1.9 \cdot 10^{25}$	0.16	KamLAND-Zen [31]
^{150}Nd	$1.8 \cdot 10^{22}$	3.4	NEMO-3 [32]

Table 1.1: A listing of the strongest available $\beta\beta0\nu$ limits; all limits are quoted at 90% confidence. Limits on $\langle m_{\beta\beta} \rangle$ are obtained using phase space factors from [22] and matrix elements from [33], both chosen for the completeness of their tabulations. For ^{136}Xe , this author has taken the liberty of including both Kamland-Zen's published results and EXO-200 results described in this work.

Chapter 2: The EXO-200 Detector

This chapter will describe the physical apparatus of the EXO-200 detector. Section 2.1 will give a broad overview of the detector. Section 2.2 will identify the dominant backgrounds for $\beta\beta0\nu$ decay, and sections 2.3 and 2.4 will describe methods used to mitigate these backgrounds. The pulse and waveform readout subsystems are described in section 2.5, where discussion of the scintillation readout will be particularly important for subsequent chapters. We conclude with a description of the calibration systems in section 2.6. Throughout, the reader is referred to the detailed description in [34] for more information.

2.1 Overview of the EXO-200 Detector

The EXO-200 detector is a cryogenic experiment containing 175 kg of liquid xenon enriched to 80.6% in ^{136}Xe . Of those 175 kg of liquid xenon, 110 kg are contained within the “active” volume where the detector is fully sensitive to deposited energy from $\beta\beta$ decay, [34] and 94.7 kg are contained within the fiducial volume where we believe the detector’s response is well-understood. Only fiducial xenon will be used in the search for $\beta\beta0\nu$ decay; this means there are $3.39 \cdot 10^{26}$ atoms ^{136}Xe which will

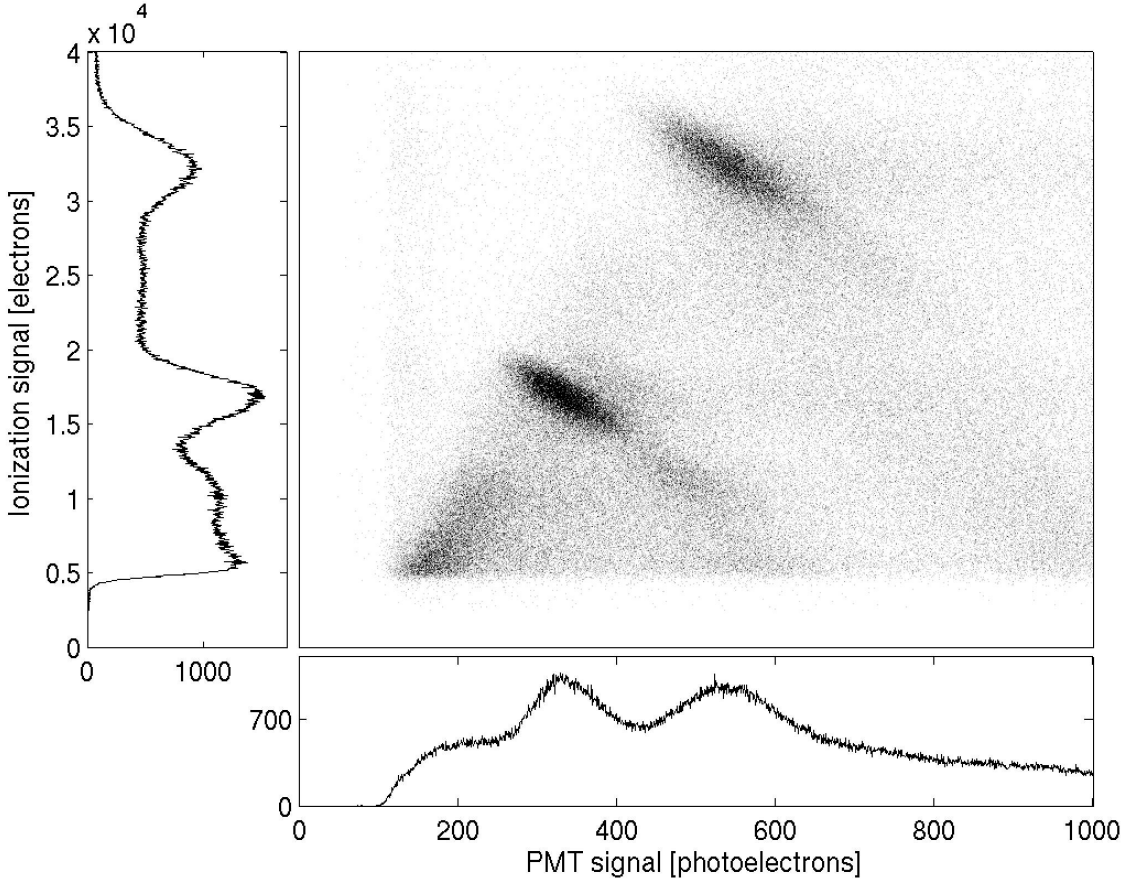


Figure 2.1: A two-dimensional energy spectrum of scintillation and ionization from a testbed liquid xenon experiment under an electric field of 4 kV/cm. The spectrum is from a ^{207}Bi source. Figure reproduced from [36].

be used for setting half-life limits. [35]

Energy deposits in xenon can be measured primarily in two ways: optical photons are emitted from the excitation and de-excitation of atomic electrons of xenon, and xenon atoms are ionized to produce free electrons. It is well-known [36] that liquid noble element calorimeters show significant fluctuations in their separate production of scintillation photons and free electrons, but that these separate quantities are strongly anticorrelated. As a result, is it possible to achieve far better

energy resolution if both light and charge are independently measured than if only one is detected; figure 2.1 illustrates this phenomenon in a testbed liquid xenon experiment, where it is apparent that using light and charge simultaneously lets us observe narrower gamma lines than either individually.

Scintillation will be produced from energy deposits in liquid xenon in all cases; [37] however, to observe free electrons we must exert an electric field on the xenon which drifts the electrons onto a collection anode. The EXO-200 detector is shaped as a cylinder, and the required electric field is produced by placing a cathode grid in the center of that cylinder and anode wires along each of the two endcaps of the detector; such a detector is called a time projection chamber, or TPC. The EXO TPC is shown in figure 2.2. The light is collected by avalanche photo-diodes (see section 2.5 for details) mounted on the endcaps behind the anode wires; the anode wires are thin, so the effect on light collection efficiency is minimal.

The cathode is maintained at a voltage of 8 kV above the anode wire voltage. Field shaping rings encircle the outside of the EXO cylinder to ensure that electric field lines are approximately parallel and the magnitude of the electric field is roughly constant in the bulk volume of xenon. (Near the edges, non-uniformities in the electric field are believed to exist; these are a continuing topic of research.) The cathode and anode wires are separated by roughly 20.4 cm; after accounting for edge effects, we believe that the bulk volume of xenon has an electric field of roughly 374 V/cm.

Electrons in liquid xenon drift at a velocity of $1.71 \text{ mm}/\mu\text{s}$ under an electric field of 375 V/cm. The maximum drift distance from the cathode to the anode

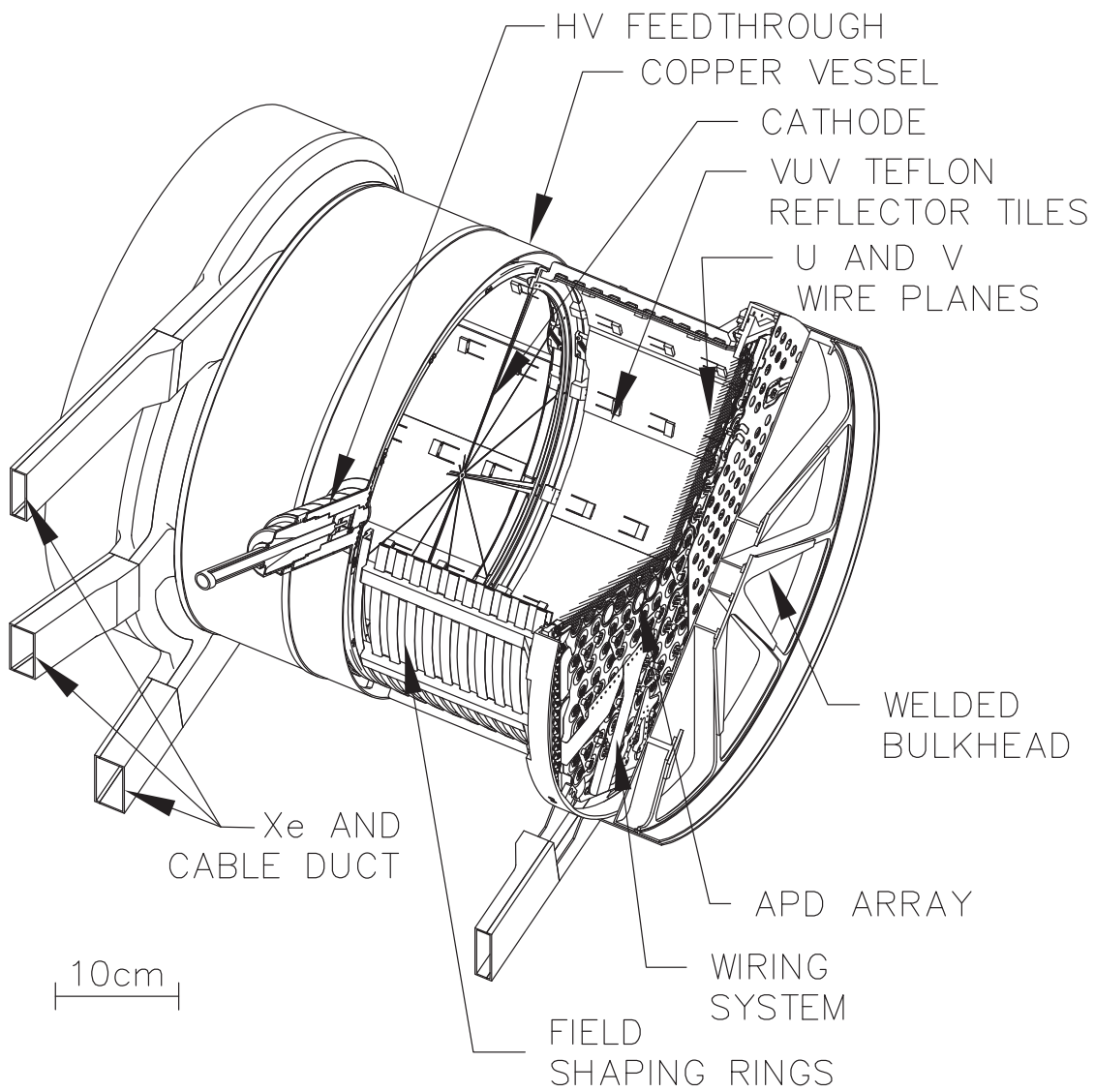


Figure 2.2: Schematic of the inner EXO-200 TPC. Figure reproduced from [34].

is 198.4 mm, resulting in a maximum electron drift time of roughly $116 \mu\text{s}$. Free electrons are not absorbed by xenon – as for other noble elements, xenon has a low electronegativity, so in a pure xenon detector electrons could drift unimpeded for the time necessary to reach the anode. EXO-200 does have small quantities of electronegative impurities such as oxygen and methane; to minimize the concentration of these impurities, the xenon of EXO-200 is constantly circulated through a chemical purifier which extracts chemically active molecules and permits noble elements to pass through. [34]

It is necessary to associate charge pulses with their corresponding scintillation pulses in spite of their time separation. However, this is easily done provided the time between events is much longer than $116 \mu\text{s}$. Thus, sources should be calibrated to produce a data rate in xenon no higher than roughly 1 kHz. By measuring the time difference between the observation of scintillation and the collection of charge, we can measure the position of the energy deposit along one dimension. Our time resolution permits us to reconstruct this position coordinate with an accuracy of 0.42 mm. [38]

At the anode, there are two sets of parallel wire planes. The first (closer to the cathode) parallel wire plane is called the “v-wire” plane, and the second plane is called the “u-wire” plane. The voltages of the two wire planes are set so that no electric field lines terminate on the v-wires, and all field lines instead penetrate through the v-wire plane and terminate on the u-wires. When charge is deposited within the liquid xenon and drifts toward the anode, it induces a current on the v-wires as it passes by, and then produces a current on the u-wires as it is collected.

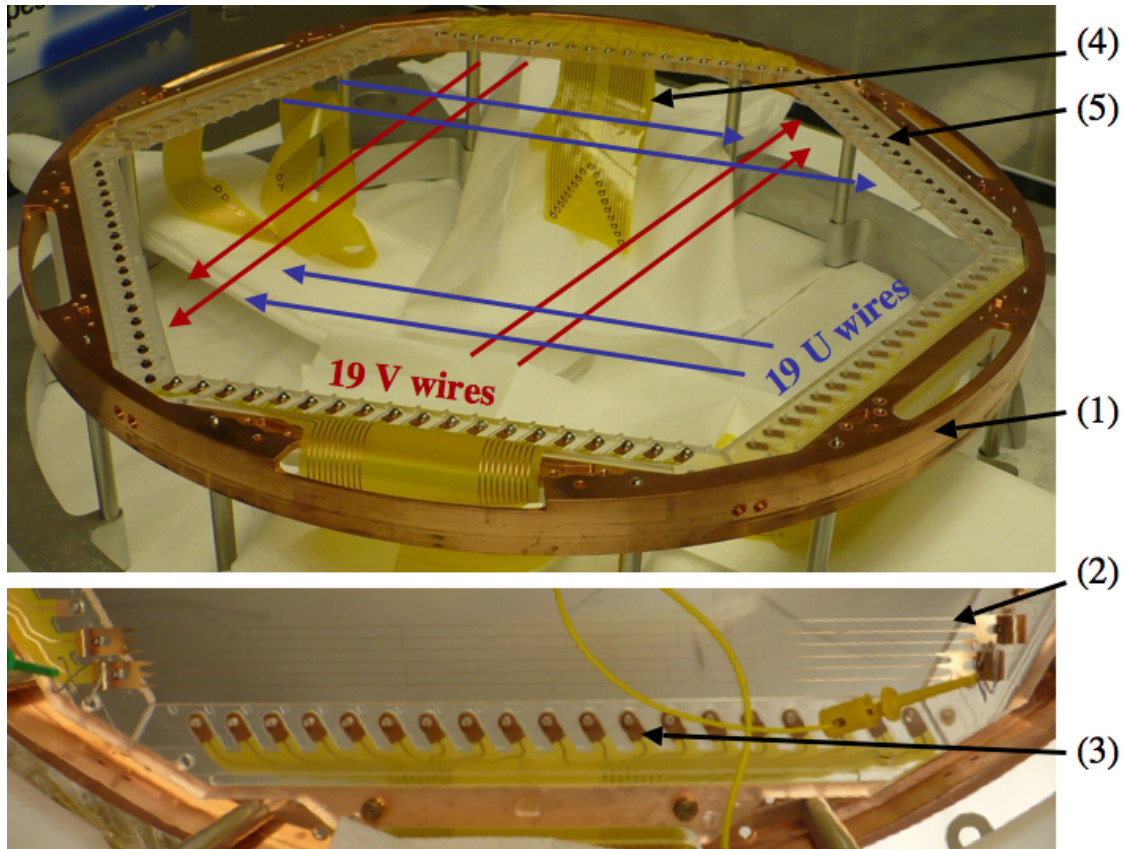


Figure 2.3: Anode collection wires (u-wires) and induction wires (v-wires) from EXO-200. (1) and (5) indicate the wire support frame; (2) indicates the wires themselves, constructed as gangs of three wires; (3) illustrates the attachment between wires and the support frame; (4) shows the return cables from the wires to the data acquisition system. Figure reproduced from [34].

Figure 2.3 indicates the relative orientation of the u-wires and v-wires. By detecting which (set of) wires observes a current pulse in both the u-wire and v-wire channels, it is possible to identify the two-dimensional location on the anode where the charge arrived. Channels in each plane are 9 mm wide; by taking advantage of signal sharing which sometimes occurs between u-wires and always occurs between v-wires, we are able to achieve position accuracy of 2.4 mm perpendicular to the u-wires and 1.2 mm perpendicular to the v-wires. [38]

Energy which appears to come from a single location is called a charge deposit “cluster” or “site”, and events are classified according to the number of sites they produce (their “multiplicity”) as either single-site or multi-site. We will see in section 2.4 that this provides a powerful tool for background rejection.

This section has described how energy deposits in the liquid xenon are transformed into scintillation and charge, which are then observed by APDs and anode wires, respectively. These observations are sufficient for us to reconstruct the positions and magnitudes of energy deposits in the liquid xenon.

2.2 Backgrounds to $\beta\beta0\nu$ Decay

^{136}Xe has a relatively high Q -value compared to most other $\beta\beta$ decays; in the neutrinoless mode the two emitted electrons will share 2456.7 keV. [35] This means that the sensitivity of $T_{1/2}^{0\nu}$ to the mass of the neutrino is good in ^{136}Xe , as was described in section 1.5; it also means that energy spectrum around our Q -value will naturally be relatively free from most sources of background radiation. This section will

identify the types of background which can be expected to affect our $\beta\beta0\nu$ search; subsequent sections will describe methods of mitigating those backgrounds.

It is common for alpha decays to have energies well in excess of our Q -value. As a result, we might expect all alpha decays to be possible backgrounds to $\beta\beta0\nu$. However, alpha particles are stopped rapidly by even a small quantity of shielding, and as a result the only alpha decays which can be observed in the detector are those from sources which are dissolved into the xenon. Radon is the only alpha-emitting noble element, and only ^{222}Rn is sufficiently long-lived to diffuse into the xenon; as a result, we only expect ^{222}Rn and its daughter products to contribute a significant quantity of alpha decays to the detector.

Cosmic rays produce high-energy muons; these are another source of high-energy backgrounds. Muons will produce a streak of energy in the detector rather than discrete clusters; generally they will have sufficient energy to pass fully through the detector. We can expect that such an event will look substantially different from a $\beta\beta0\nu$ event, and generally will deposit substantially more energy than our Q -value as well.

More interesting are the associated by-products from the passage of such a high-energy particle, called spallation products. Although high-energy muons can produce a range of fission products, the most significant spallation product of muons will be neutrons which can diffuse into the detector and activate materials there. ^{134}Xe and ^{136}Xe are both present in significant quantities in the TPC, and by activation can be converted into the radioactive isotopes ^{135}Xe and ^{137}Xe respectively. ^{135}Xe has too little energy to be a background to $\beta\beta0\nu$ decay, but ^{137}Xe undergoes

β decay with a maximum energy of 4173 keV. We will see that indeed ^{137}Xe is a significant source of background in our detector. [35, 39]

Some sources of background are intrinsic to the $\beta\beta0\nu$ search. Any isotope which can undergo $\beta\beta0\nu$ decay can also undergo $\beta\beta2\nu$ decay, and the endpoint of the $\beta\beta2\nu$ spectrum is necessarily at our Q -value. The only means of reducing background from $\beta\beta2\nu$ is to improve the energy resolution of the detector so that fewer such decays can mimic $\beta\beta0\nu$ decay. Fortunately with the energy resolution exhibited by the EXO-200 detector, $\beta\beta2\nu$ is subdominant to other backgrounds by many orders of magnitude. [35]

Similarly, it is hypothetically possible for neutrino absorption to stimulate a $\beta\beta2\nu$ decay by the reaction



which is obtained from the $\beta\beta2\nu$ reaction by taking one neutrino from product to reactant in equation 1.1. The observable spectrum is similar to the standard $\beta\beta2\nu$ spectrum, but with the endpoint shifted upward by the energy of the absorbed neutrino. The cross-section for this reaction is expected to be well below the cross-section for standard $\beta\beta2\nu$, so this will be a negligible background well beyond the current generation of $\beta\beta$ detectors.

A gamma background which is particularly detrimental to EXO-200 comes from ^{214}Bi , a member of the radium decay chain. ^{214}Bi emits a gamma particle at 2448 keV, which with our energy resolution is indistinguishable from our Q -value. It will occur as a daughter product of ^{226}Ra , which has a half-life of 1600 years

and generally will be supported by ^{230}Th (75,000 years), ^{234}U (250,000 years), and ultimately by ^{238}U ($4.5 \cdot 10^9$ years) which has a primordial abundance in the Earth's crust and most natural materials. [40]

Most other backgrounds to $\beta\beta0\nu$ will be gamma decays from ^{208}Tl , a member of the thorium decay chain. ^{208}Tl emits a gamma particle at 2614.5 keV; with our Q -value of 2456.7 keV, the two energies are separated by 157.8 keV. [40] The energy resolution (in σ/mean) of EXO-200 has typically been 1.5–2% at these energies, [35] meaning that separation between the central values of the gamma lines will be $3-4\sigma$. The thorium decay chain is supported by ^{232}Th , which has a half-life of 14 billion years and has a significant abundance in most natural materials; we may expect it to contribute a significant fraction of our radioactive backgrounds, and as a result we may expect that some events from the 2615 keV ^{208}Tl line will leak across those $3 - 4\sigma$ and act as backgrounds. Keeping our energy resolution at or below 1.5% may be of significant interest in reducing contamination from this gamma line.

The compton edge is a well-known feature of gamma decay spectra; it originates from gammas which enter a calorimeter, scatter once, and escape from the detector. The maximum energy which a gamma of incident energy E_{inc} can deposit in a single compton scatter is: [41]

$$E_{dep} = \frac{2E_{inc}^2}{m_e c^2 + 2E_{inc}}. \quad (2.2)$$

When the incident gamma has an energy of 2615 keV, the compton edge will lie at 2382 keV, or only 74.5 keV below our Q -value. Using the same estimate that our energy resolution is around 1.5–2 σ at these energies, this separation is only around

$1.5 - 2\sigma$. It is clear that improving our energy resolution may have a strong impact on background contamination by improving separation from the compton edge of the ^{208}Tl as well as its full deposit line.

We have here identified some of the primary backgrounds which can be expected in the EXO-200 detector, noting particularly those which can be significantly reduced through improvements to the energy resolution. The following sections will identify some of the mechanisms used to further minimize these backgrounds.

2.3 Passive Background Rejection

When we describe the methods by which backgrounds to $\beta\beta0\nu$ are reduced, we can distinguish between two classes: passive methods in which backgrounds are reduced by reducing the amount of background reaching the xenon in the first place, and active methods in which backgrounds are observed by the detector but discriminated from $\beta\beta$ signal based on identifying characteristics. In this section, passive methods will be described; section 2.4 will describe the active methods of background rejection.

The simplest and most immediate method of reducing the presence of backgrounds is by exploiting the self-shielding properties of xenon. The xenon itself is extremely pure due to the ease of chemical purification; as a result most backgrounds will be external to the xenon. Since external gammas are attenuated by dense materials such as liquid xenon, we can expect that the xenon near the center of the detector will be exposed to less background than the xenon near the TPC

Xenon

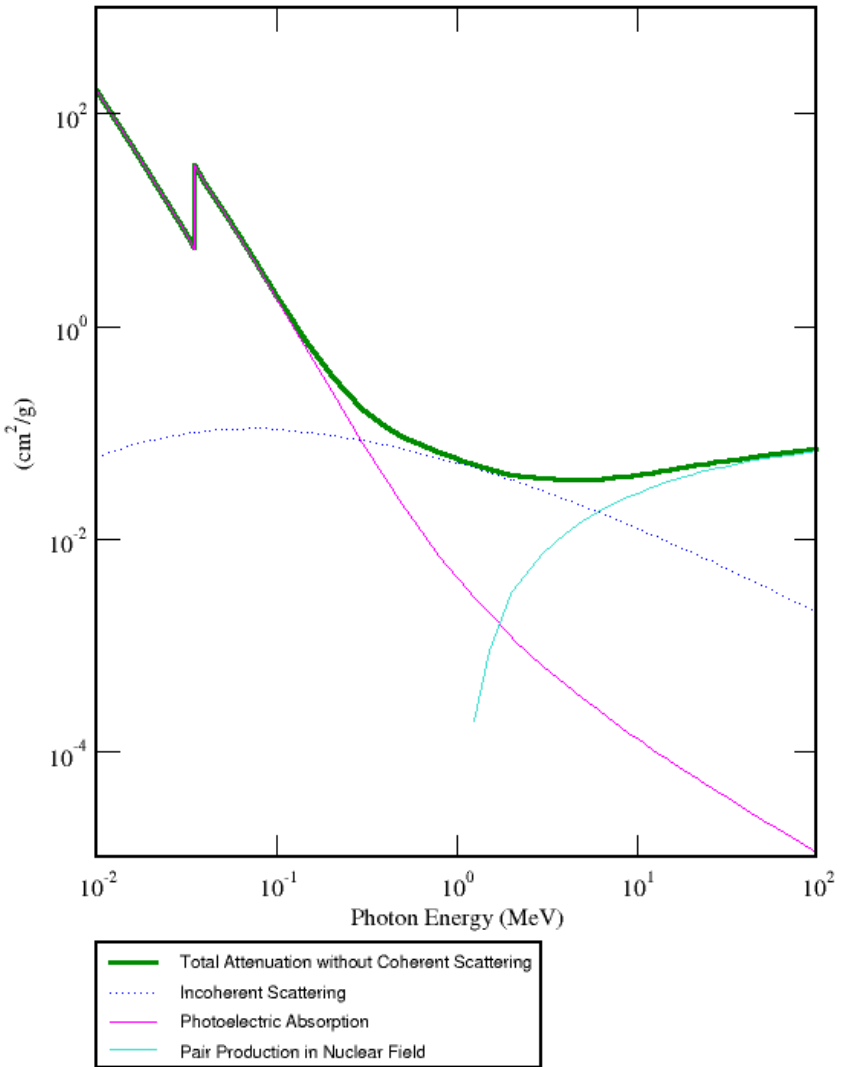


Figure 2.4: X-ray attenuation lengths in xenon. Compton (incoherent) scattering, pair production, and photoelectric absorption are shown, along with their combined attenuation length; coherent (Rayleigh) scattering is omitted because it produces no observable energy deposit. The vertical axis, in cm²/g, can be multiplied by the density of the xenon to derive an attenuation factor per unit length. Figure produced by [42].

walls. This is one of the primary advantages of xenon as a source: it is easy to construct a large monolithic detector, maximizing the quantity of xenon which is shielded from the walls.

Figure 2.4 shows the attenuation lengths of gammas at a range of energies in xenon. Photoabsorption and pair production both convert the gamma entirely into short-ranged electron and positron carriers; compton (incoherent) scattering results in only some deposited energy, with the rest remaining in the gamma which will rebound and continue on its path. Liquid xenon has a density around 3 g/cm^3 , which means that the minimum attenuation factor is roughly $0.1/\text{cm}$ at energies around 4 MeV. Unfortunately, this is the same order of magnitude as our Q -value at 2456.7 keV, which means that at the energy of interest to us self-shielding is minimally effective. Nevertheless, there will still be some reduction in backgrounds deeper in the interior of the xenon, and lower-energy gammas will be attenuated more effectively. [42]

To reduce the quantity of background around the detector, all materials near the xenon were carefully screened for radioactive contamination. Backgrounds from ^{40}K , ^{232}Th , and ^{238}U were cataloged for all materials which have unshielded line-of-site access to the detector system. Requirements for ^{238}U were particularly stringent because its daughter products include the ^{214}Bi background which cannot be resolved from $\beta\beta0\nu$ decay. For the copper of the TPC vessel and the lead shielding around the detector apparatus, samples from a range of companies and mines were tested to locate an optimal choice of material source. For the wires which were placed into the TPC, a range of manufacturing methods were tested; improvements to a

photo-etching scheme were identified which led to a reduction in background from these materials. This thorough material screening research is one of the distinctive processes which has enabled EXO-200 to fully reach its background targets. Details of the quantification of and constraints on material radioactivity can be found in [43].

Beyond selecting extremely clean materials, it is possible to reduce backgrounds by minimizing the mass of these external materials. Most notably, EXO-200 is constructed with a copper TPC which in most places is only 1.37 mm thick; to maintain structural integrity, supporting structures are welded to the TPC where needed, and it was possible to keep the total mass of copper below 30 kg. [34]

Some materials were dispensed with entirely. Typically, silicon APDs are encapsulated with ceramic to isolate them from water contamination and provide electrical insulation. However, this ceramic material would have contributed backgrounds. Instead, the APDs were delivered “bare,” without any encapsulation, and protected from water by storing them in a dry-nitrogen container. Liquid xenon itself serves as an excellent electrical insulator, ensuring the APDs would function properly during detector operations. [44]

Another example of material avoidance comes from the cabling from wires and APDs to the electrical amplifiers and digitizers. These electronics contain many high-background plastics and other complex materials, so they were placed outside the lead shielding rather than placing them close to the TPC. Wires connect the sensors in the TPC to these electronics; ordinarily such long wires would need to be shielded by coaxial cabling to minimize cross-talk noise. However, the coaxial cabling was expected to contribute a high quantity of radioactive background, and

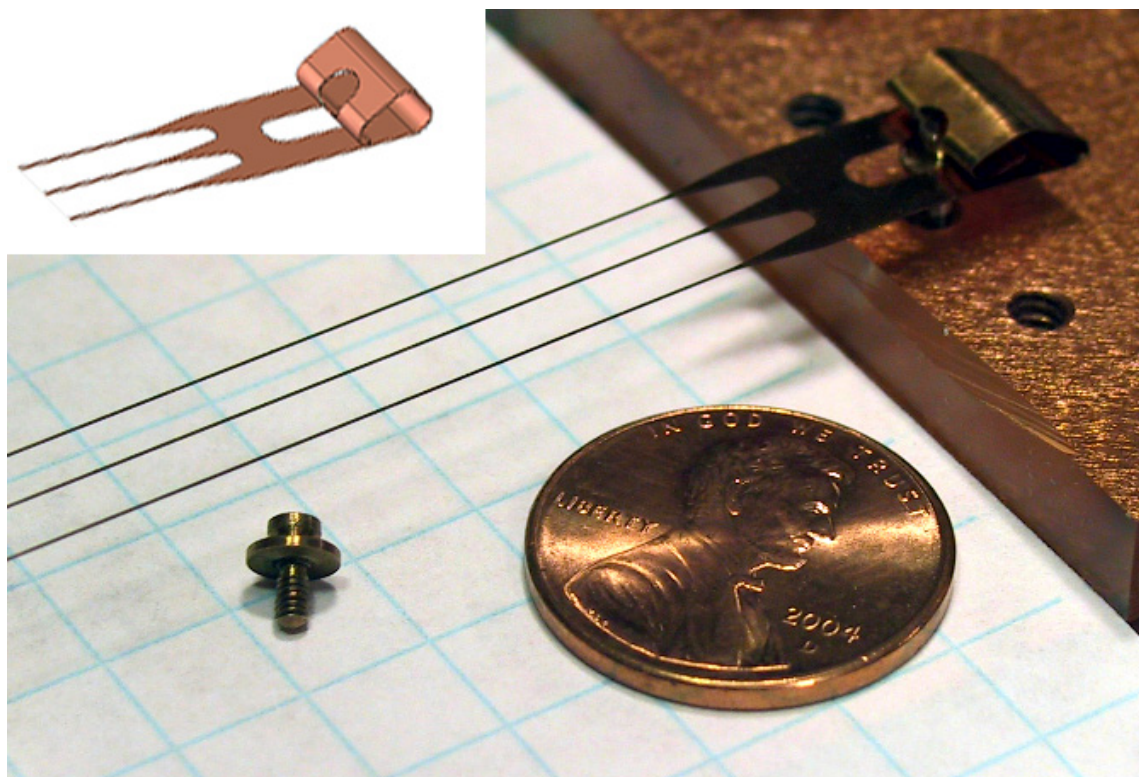


Figure 2.5: Wire triplet, read as one channel. Figure from [34].



Figure 2.6: APDs ganged together (bottom right). Wiring to the front-end electronics are visible as yellow “tape.” Figure from [34].

was omitted; instead wires are partially shielded by surrounding them with inactive wires which reduce cross-talk noise. Furthermore, the total number of wires needed was reduced by ganging together triplets of u- and v-wires and groups of six or seven APDs into single channels; this reduced the fineness of event information available in analysis, but reduced the quantity and complexity of material placed near the detector. See the wire gangs in figure 2.5; APD gangs and wiring to external electronics are visible in figure 2.6. [34]

We can imagine the TPC being shielded by nested layers of clean material designed to prevent backgrounds from reaching the xenon. In the innermost layer, HFE-7000 refrigerant (see figure 2.7) is used to maintain the detector at liquid xenon temperatures and maintain similar pressures inside and outside of the copper vessel walls. However, the HFE has a significant quantity of hydrogen, which makes it an

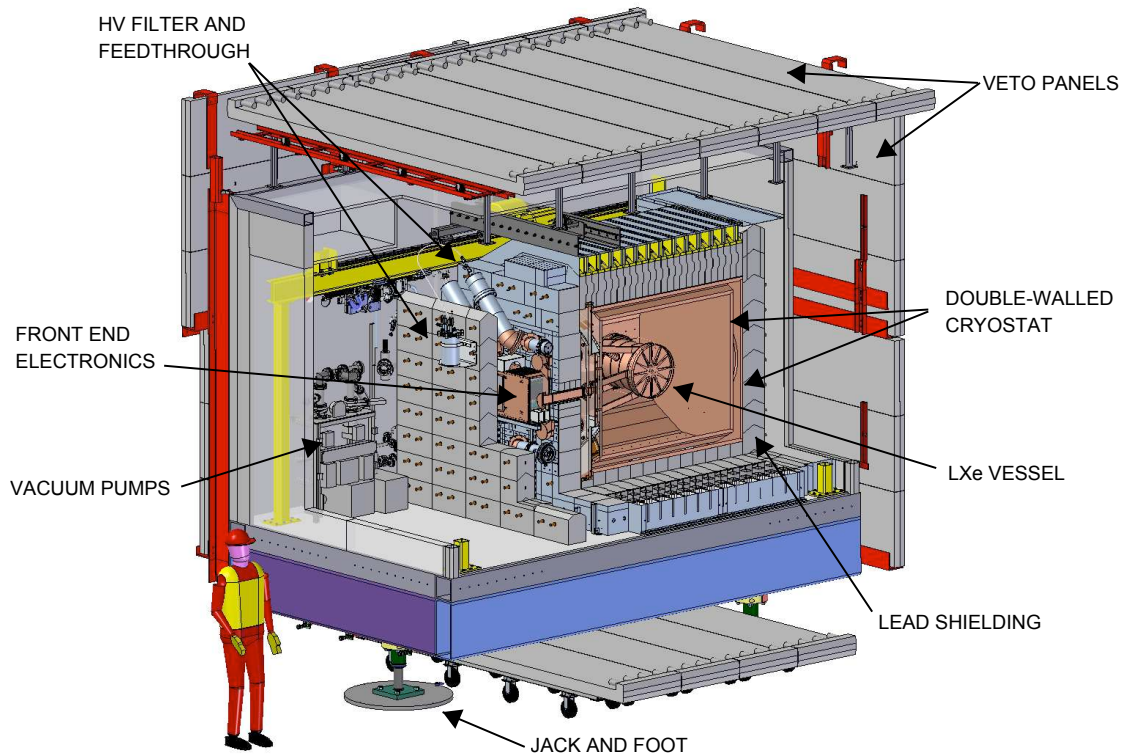


Figure 2.7: A cutaway schematic image of the TPC and surrounding materials in the cleanroom. HFE-7000 refrigerant is contained between the cryostat and the LXe vessel. Figure from [34].

excellent stopping agent for thermal neutrons. The refrigerant layer is more than 50 cm thick, so most neutron products of muons have time to thermalize and absorb onto hydrogen before reaching the TPC and producing ^{137}Xe . [34]

The following layer of shielding is lead, shown in figure 2.7. This is a common approach for low-background experiments due to the high density of lead, which enables it to stop gammas in a short distance. Lead bricks surround the detector on all sides; the bricks were designed with an interlocking shape to ensure no seams between bricks left a line-of-sight path from external sources into the TPC. In the front of the detector, where plumbing must enter and exit the detector through the first lead wall, a second lead wall is assembled with the purpose of blocking any line-of-sight paths into the TPC through the plumbing gaps of the first wall. [34]

Outside of the lead shielding, restrictions on materials are less stringent; however, control over the presence of materials is still desired. The entire apparatus is contained inside a class-1000 clean room facility. Entire facility is located in the Waste Isolation Pilot Plant (WIPP) facility, a DOE-owned waste repository located in a salt mine in Carlsbad, NM. The overburden of the facility is 1585 m water-equivalent, leading to a significant reduction in muon rate compared to the rate observed on the Earth's surface. Figure 2.8 demonstrated the reduction in muon flux due to depth at the WIPP site and a selection of other underground science facilities.

These passive approaches have all been demonstrated to reduce the rate of backgrounds depositing energy in the liquid xenon. The following section will describe an active set of background-rejection approaches.

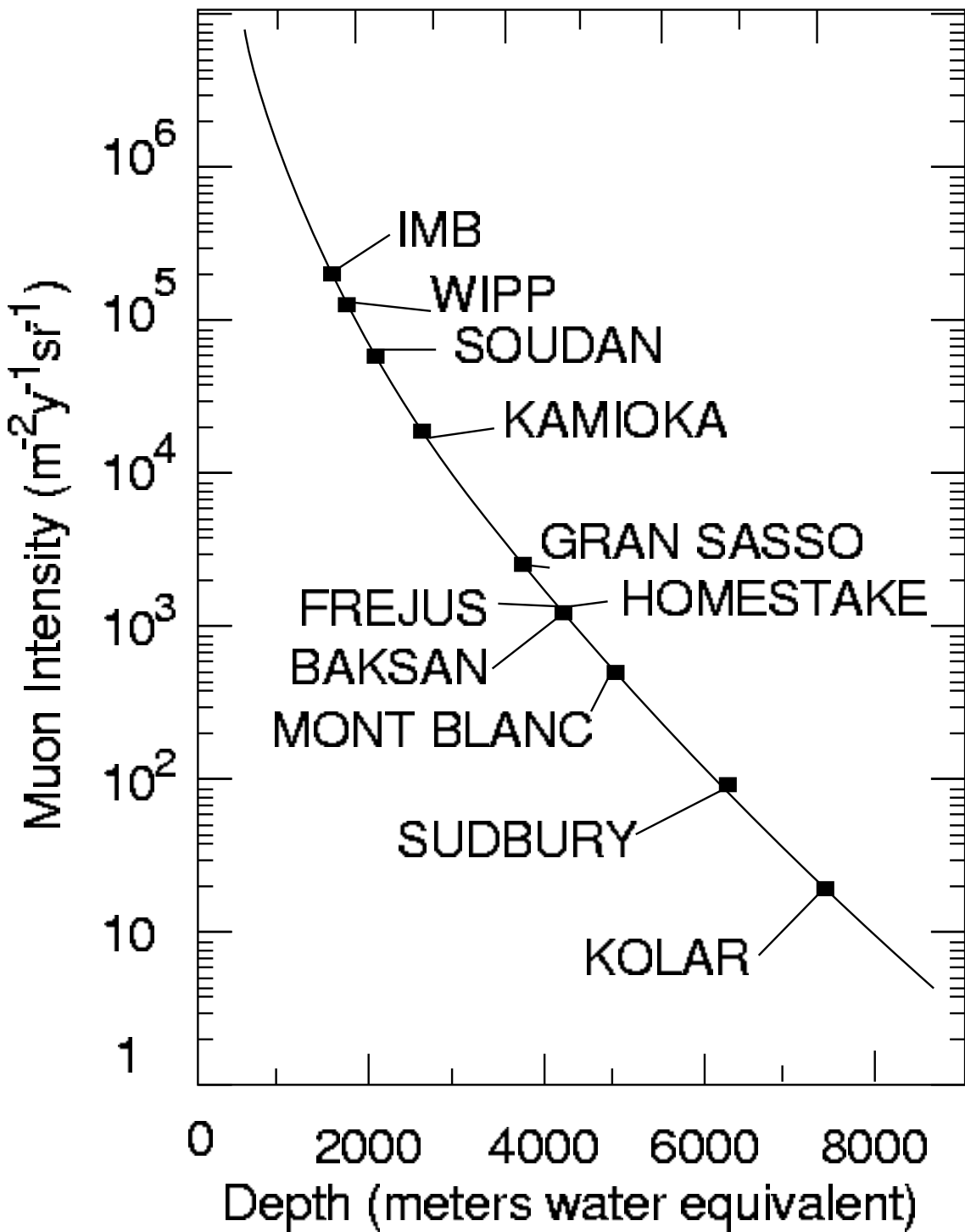


Figure 2.8: Muon flux as a function of depth, in meters water equivalent. The WIPP site is indicated in relation to other underground science facilities. Figure from [45].

2.4 Active Background Rejection

This section will describe the “active” forms of background reduction employed by the EXO-200 detector, in which events are observed but discriminated from $\beta\beta$ events based on their characteristics. We neglect the energy resolution as a background rejection tool here, since section 2.2 has already described how the impact of certain backgrounds may be reduced by improvement to the energy resolution.

A number of cosmogenic backgrounds have been described: neutrons and fission products can be produced from muons penetrating down to the depth of the WIPP facility. To reject many of these events, it is sufficient to detect the passage of a muon anywhere near the detector. This is accomplished by means of a set of veto panels surrounding the cleanroom on four of six sides. Muons are detected by coincident panel hits on opposite sides of the detector, with $(96.0 \pm 0.5)\%$ efficiency for detecting muons which traverse the TPC. [34] Further reduction in the impact of muon-induced backgrounds is achieved by searching for muon tracks observed within the TPC itself, and also by applying a one-second coincident event cut as a catch-all for spallation products of muons which may decay multiple times in rapid succession.

Alpha decays within the xenon were identified as another possible source of high-energy backgrounds. However, it is possible to discriminate alpha decays from beta and gamma decays based on the properties of their energy measurement. Alphas produce a far more dense energy deposit in liquid xenon than betas and gam-

mas; the dense collection of free electrons and ionized xenon has a higher rate of recombination than is observed with betas and gammas, which translates into a higher ratio of scintillation to ionization for alphas than for betas and gammas. This feature can be used to eliminate nearly all alpha background.

Discriminating between gamma, beta, and double-beta decays is more difficult. Gammas generally deposit their energy by ionizing atomic electrons of xenon, so in this way their behavior may closely mimic that of betas. However, most gammas within our energy window (and particularly gammas near our Q -value) will be attenuated by compton (incoherent) scattering, as can be seen in figure 2.4. By this process the gamma will deposit energy in more than one discrete location, which beta and double-beta decay will not do. We are generally able to resolve the positions of these energy deposits and classify the event as multi-site; more than half of external gamma backgrounds are classified as multi-site, whereas the fraction of $\beta\beta$ events classified as multi-site is only 5%. [38]

These are some of the basic techniques employed to reduce backgrounds in offline analysis, and the detector has been designed with the goal of facilitating their application. Although the passive methods of background reduction cannot be improved once construction of the detector is complete, it may be hoped that these active methods may be improved or extended through further analysis. These improvements could have the potential to reduce backgrounds in data which has already been collected, making them a particularly attractive target now that EXO-200 has collected a significant dataset.

2.5 Pulse Amplification and Waveform Readout

After an APD or wire collects a signal, how is it converted into a waveform on disk?

This section will provide a brief overview of the EXO electronics and waveform readout. Particular attention will be paid to subsystems which are relevant to the denoising algorithm described in chapter 3, including the APDs and front-end electronics.

The APDs are constructed from a silicon semiconductor which is doped and biased so that: [46]

1. Photons arriving at the active surface of the APD can deposit their energy by generating an electron-hole pair in the silicon semiconductor.
2. The electron-hole pair is drifted apart by an electric field. Here the electric field is low and the silicon is doped to be of p-type (electron-poor), ensuring a similar number of electron-hole pairs are produced by all photons before any amplification can occur.
3. The electron enters a high-field n-type (electron-rich) region of silicon, and liberates additional electron-hole pairs in an avalanche effect.
4. Electrons reach another p-type region of silicon, and then are collected on a cathode as an output current pulse.

These phases of the APD are illustrated in figure 2.9.

EXO-200 had 851 APDs specially made with pure aluminum and no casing;

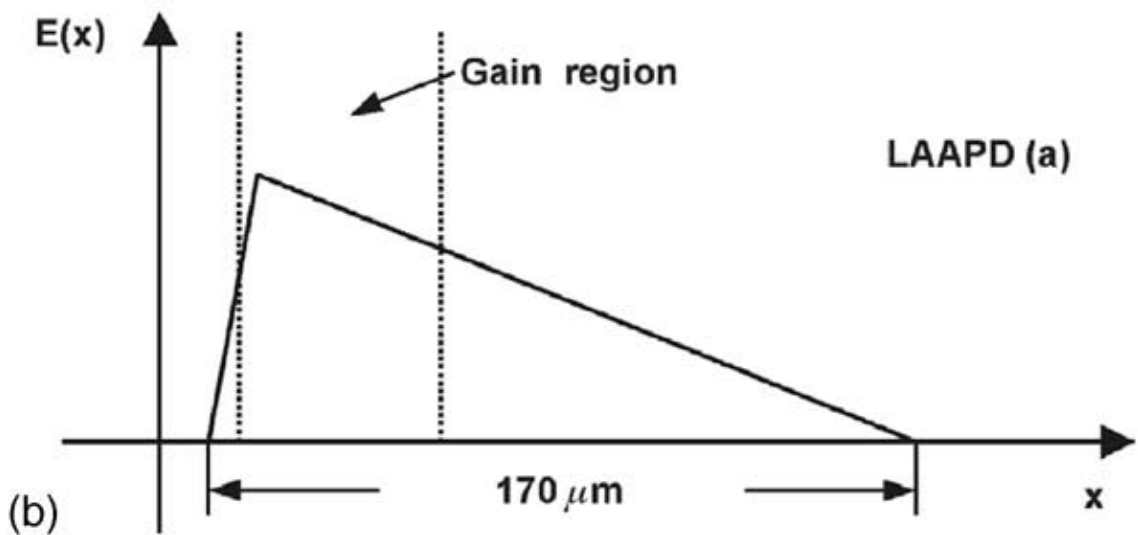
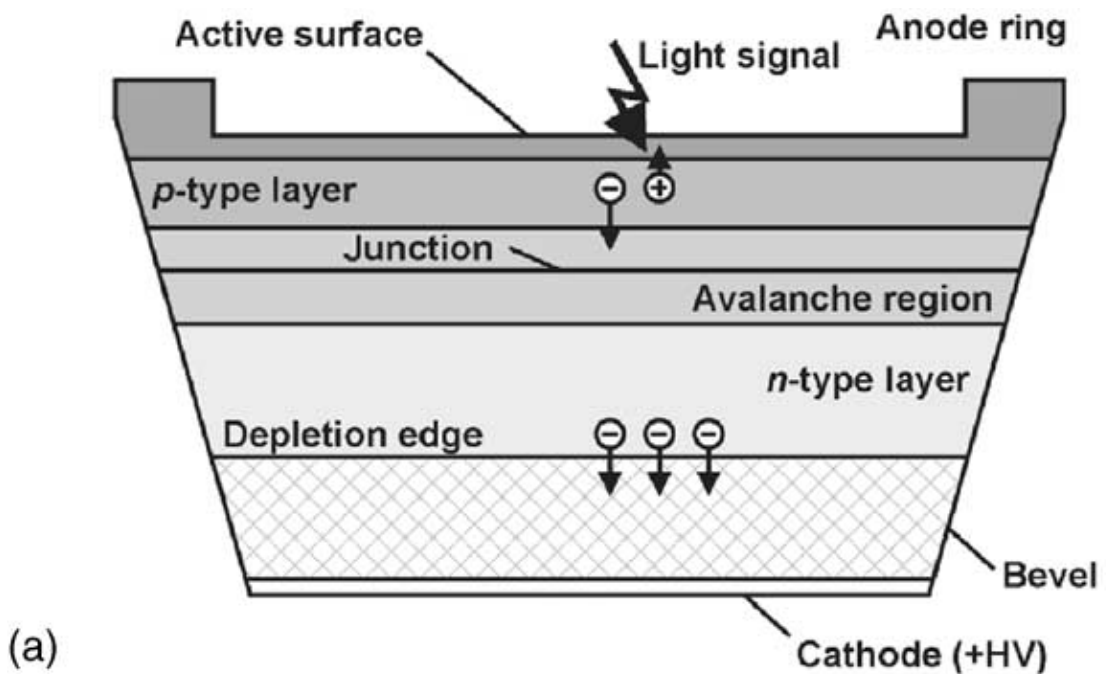


Figure 2.9: A cross-sectional schematic of an APD is shown in (a). The electric field as a function of depth is shown in (b). Figure from [46].

from those, 468 were selected for use based on their excellent noise and gain properties. [44] For each APD, the relative quantum efficiency for electron-hole production and the bias voltage needed to ensure the product of gain and quantum efficiency equals one hundred were both measured. APDs were assigned to gangs and pies so that their products of gain and quantum efficiency could be set to one hundred as uniformly as possible. [47] It is impossible to make the gain of all APDs perfectly uniform because of limitations in the configurability of the APD bias voltages in EXO-200. [34] We note that the current operating conditions of EXO-200 establish a higher operating gain of around 200 – 300; this may have the side effect of making the product of gain and quantum efficiency less uniform in each APD gang.

The means by which wires deliver charge is somewhat simpler than for APDs. In the u-wires, charge is collected and delivered directly to the electronics as current. In the v-wires, no net charge is delivered, but transient currents are induced in such a way that the v-wire remains at a constant voltage; these transient currents produce a pulse with a different shape than the u-wire pulses, such that the integral (before shaping) is zero. We note that the pulse shape depends on the path of electrons in the xenon – both sets of wires deliver a current signal which is induced from approaching charge before the charge deposits on the u-wires, and the path of the electrons can affect the timing of that induced current. Furthermore, the pulse magnitude will depend on the point of origin of the electrons because at that location positively-charged ions will remain long after the electrons have been collected, and the ions will hold a net charge on the u- and v-wires which is released only on much longer timescales than we can observe in our waveforms. (Ions, being much more massive

than electrons, drift much more slowly through liquid xenon.) [48, 49]

The front-end electronics, located between the two lead walls in front of the detector, consist of four stages: [34, 50]

1. A transimpedance amplifier which converts the current signals from the detector to voltage signals. This stage applies amplification and a differentiator with a long time constant (roughly $60\mu\text{s}$ for wires and $300\mu\text{s}$ for APDs).
2. Two differentiators and two integrators, to improve signal-to-noise ratio for real-time triggering. For the u-wires, each integrator has a time constant of $1.5\mu\text{s}$ and each differentiator has a time constant of $40\mu\text{s}$; for the APDs and v-wires, each integrator has a time constant of $3\mu\text{s}$ and each differentiator has a time constant of $10\mu\text{s}$. Some signal amplification is applied at this stage as well.
3. An analog-to-digital converter (ADC) converts voltage pulses into 12-bit digital waveforms. The full 12-bit scale is equivalent to 2.5V. Digitization is performed at a rate of 1MHz.
4. A triggering module reads the digitized waveforms, and issues a trigger to the data acquisition (DAQ) when signals exceed programmable thresholds. The triggering module can also accept external requests for a “solicited” trigger.

In most cases, when a trigger is issued, the DAQ will write out 2048 samples (just over 2ms) from all waveforms, centered on the first sample responsible for the trigger.

In cases where the data rate is high, waveforms can be truncated to a length less

than 2048 samples.

2.6 Calibration Systems

Energy resolution has been discussed as a general feature of the detector which can have a significant impact on the reduction of backgrounds. A significant factor in the resolution is the quality of the detector's absolute energy calibration. This is particularly important because of the long lifetime of the experiment. If the calibration of the detector drifts over time, this will be perceived in the cumulative low-background spectrum as a smearing out of energy peaks, worsening the effective resolution. This section will describe some of the techniques used to produce an accurate time-dependent calibration for the detector.

The most critical type of calibration comes from external gamma sources. The EXO experiment was constructed with a guide tube passing through the HFE refrigerant and wrapping loosely around the TPC, as shown in figure 2.10. Currently available to the experiment are sources containing ^{228}Th (primary gamma line at 2615 keV), ^{60}Co (simultaneous emission of gammas at 1173 and 1332 keV), and ^{137}Cs (gamma line at 662 keV); additionally, a new ^{226}Ra source became available in the summer of 2013 (numerous gammas, including 2448 keV). Together these sources allow us to observe the detector response to external gammas with known energies, permitting energy calibrations, energy resolution measurements, and verification of monte carlo simulations.

All of these sources have been used periodically (roughly every three months)

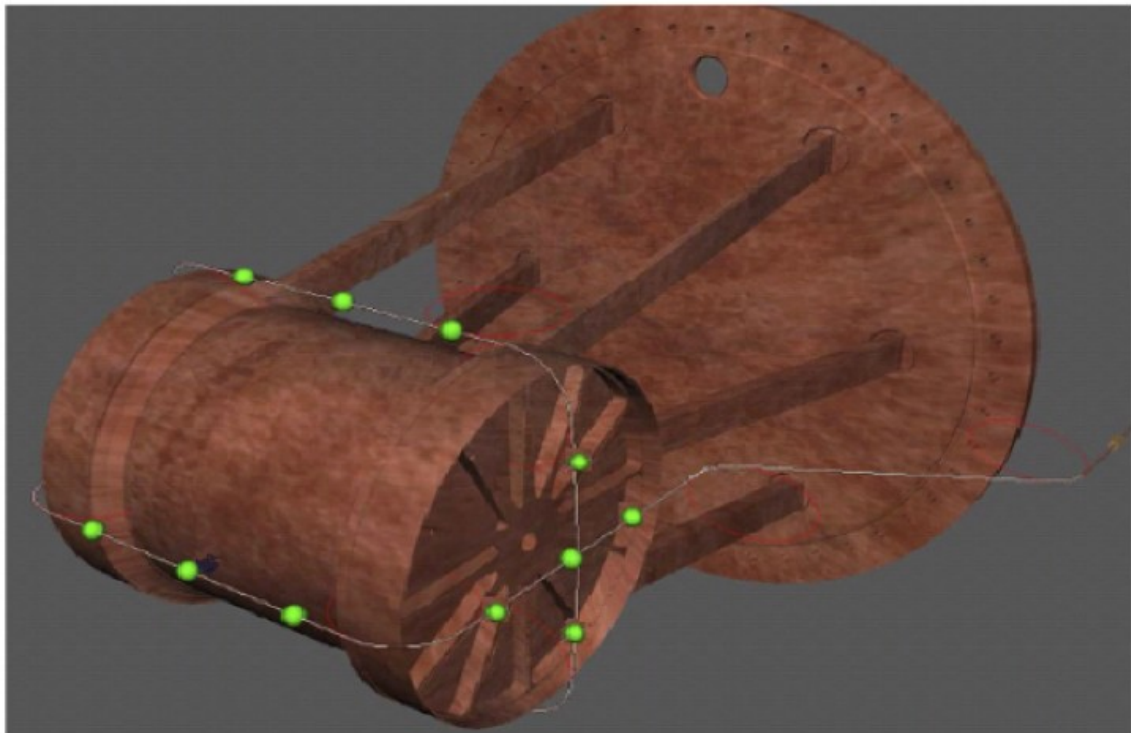


Figure 2.10: A guide tube permits gamma sources to be inserted to known locations near the TPC. Green dots indicate a few of the locations where the source may conventionally be placed. Figure from [34].

in calibration campaigns intended to permit a full characterization of the detector response across a wide energy range at a particular moment. Additionally, the ^{228}Th source has been deployed regularly, typically three times every week for 2 – 3 hours, for the entire history of the dataset. The fullness of the ^{228}Th source dataset, along with the benefit that it contains a relatively clean high-energy gamma line, make it a particularly convenient dataset to work with; it will play a prominent role in the generation of our lightmap described in chapter 5.

Other calibrations are also performed on the detector, and may in some instances supplement the information provided by the source data. To perform direct calibrations of the APDs, one APD mount contains a light diffuser rather than an APD device; the diffuser can be illuminated by a laser through optical fibers. [34] The APDs can be calibrated by pulsing the laser while varying the voltages of the APDs to adjust their gain, and in this way it is possible to measure the gain of the APDs in situ. A laser system was available at the beginning of the dataset used in this work; however, there were certain deficiencies to the laser system which made its data difficult to use, and as a result a new and more accurate laser system was commissioned in August 2012. Laser data in some form has been collected roughly once per week for much of the time containing this dataset. Composing the laser data into a coherent history of the APD gains is an ongoing project, but it has been possible to use APD gain information from specific moments to inform the APD noise model described in section 3.2.1.

Just as it is possible and desirable to learn the gain of the APDs separately from other components using laser runs, it is also desirable to learn the gain of the

electronics amplifiers separately from other detector function. This is accomplished using “internal calibrations:” simultaneously with software triggers solicited by the data acquisition, a switched capacitor injects charge into the input of the electronics cards of individual or groups of channels. [51] The resulting waveform is then read normally, and the size of the output pulse reflects the gain of the electronics. This system is employed approximately daily on all channels; it provides an excellent measure of relative changes in the electronics gains over time. However, the absolute gains cannot be extracted accurately from this data, and must be obtained by other means.

To measure the absolute gains of the electronics, the front-end cards must be physically removed from their enclosures; when this is done, it is possible to use a more accurately calibrated capacitor to make an absolute gain measurement in the same style as the internal calibrations. These “external calibrations” can be performed in two flavors: manual, in which a capacitor calibrated to 1% is used to inject charge, and automatic, in which the calibration is automatically performed at a much faster rate but accuracy is limited to 2 – 3%. Due to the inconvenience of removing electronics cards from their enclosures, this process has only been performed once in February 2011. Both styles of external calibration were performed on the u-wire channels. Less demanding needs for resolution on the v-wires and APD channels were foreseen, so only the less accurate automatic calibration was performed on those channels. The data from these runs has not been fully analyzed, but may be revived in future analysis to permit a better calibrations of the subsequent internal calibrations which were taken. A few electronics boards have

been swapped since February 2011; channels on those boards will no longer have an absolute calibration available after the board swap, so it may be advisable to perform an additional external calibration. [48]

2.7 Summary

This chapter has described some of the key characteristics of the construction and operation of the EXO-200 detector. Background reduction has been a theme throughout – EXO-200 has employed both passive and active methods to reject background and improve its sensitivity to $\beta\beta0\nu$ decay. Energy resolution has also been described as a key element in background rejection because with sufficiently precise energy measurements, many backgrounds will no longer resemble $\beta\beta0\nu$ decay. Chapter 3 will begin our discussion of a new scheme to extract more accurate energy measurements from the APD channels, thereby improving our overall energy resolution and the sensitivity of the limit on the $\beta\beta0\nu$ halflife we will be able to demonstrate.

Chapter 3: Denoising Theory

As has been discussed, the performance of double-beta experiments like EXO-200 is partially determined by their energy resolution. In EXO-200, the energy resolution is limited by the scintillation energy resolution, which in turn is dominated by electronic noise in the APDs. Significant effort must therefore be expended to understand and reduce the noise in the scintillation signals.

When the noise in the APDs is studied, it was found that the individual APD channels met targetted root-mean-square noise levels of 2000 electrons. However, rather than observing the noise on summed APD channels increase proportionally to the square root of the number of channels, the summed APD noise is roughly two to three times higher than projected. This worse-than-expected scaling of the noise with channels indicates that noise across different channels is correlated, and further analysis confirms that the bulk of the noise on an unshaped APD waveform is correlated with other channels, as shown in Figure 3.1. There are many possible sources of coherent noise in the hardware, and reducing the amount of coherent noise is a topic for further research. [52]

However, the observation that coherent noise is the dominant source of noise in

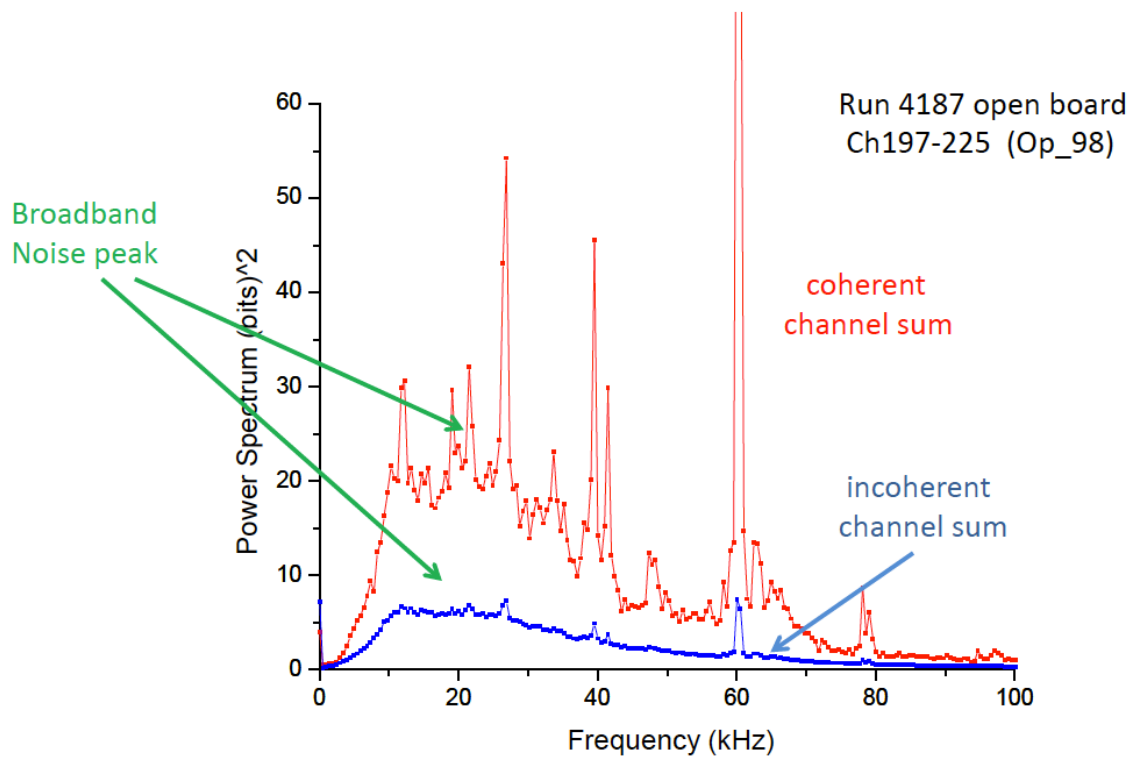


Figure 3.1: Coherent and incoherent noise power spectra for a sample set of APD channels without signal shaping. [52]

the APDs, and thus also the limiting factor in EXO-200’s energy resolution, means that it should be possible to exploit these correlations and reduce the level of noise in offline analysis. This chapter will describe a scheme to accomplish that goal and produce an optimal estimate of scintillation energy which takes noise correlations into account.

It is worth noting that in fact there are a number of different qualitative approaches to reducing the noise levels in the scintillation channel. In casual terms, we will refer to “passive” approaches as those in which components of our signals are weighted more or less heavily based on their relative signal-to-noise content. “Active” approaches, by contrast, will be classified as those which attempt to improve the signal-to-noise content of signal components. We have identified the following three types of denoising:

Frequency weighting

On a given channel signal, weight more heavily the frequency components which contain larger signal-to-noise ratio. This passive denoising scheme requires knowledge of the shapes in fourier space of a signal and the power spectrum of the noise.

Channel weighting

Different channels may have different levels of noise, so some may generally have higher-quality signals. More importantly, though, the amount of signal on a given channel depends strongly on the proximity of the APD gang to the source of scintillation within the detector. This passive denoising scheme

therefore allows us to weight more heavily the channels which have more scintillation, provided we can identify these weights on an event-by-event basis. This requires knowledge of the magnitude of noise on each channel and of the correspondence between event position and signal magnitude on each APD gang; the latter is described by the lightmap, described earlier.

Noise subtraction

This active form of denoising consists of using correlations between noise on different channels to produce a better estimate of the noise component of signals than each signal taken independently could provide. To accomplish this, we will require detailed information about the pairwise noise correlations across channels at each frequency.

In the following, we will describe a general linear operator on the APD signals which in principle can accomplish each of these forms of denoising, and we will presume that all of the described inputs are available; by identifying the parameters for that linear operator which are optimal, we can be confident that the denoising operator we produce will accomplish all three forms of denoising described above.

3.1 Setup

We first establish a number of notational conventions:

- i, j will represent indices over APD channels.
- a, b, c will represent indices of signals in an event.

- τ will represent the time indices of a discrete waveform; t_a represents the calendar time of a signal a .
- f, g will represent the frequency indices of Fourier-transformed waveforms.
- For a waveform $*[\tau]$, we will represent the discrete Fourier transform of that waveform with $\tilde{*}[f]$, where the particular convention used to evaluate the Fourier transform is not significant.
- For a Fourier-transformed waveform $\tilde{*}[f]$, we denote the real and imaginary parts of that waveform by $\tilde{*}^R[f]$ and $\tilde{*}^I[f]$, respectively.
- For an unknown parameter $*$, the symbol $\hat{*}$ will identify an estimator for $*$.
- For an expression $*$ containing random variables, $\langle *\rangle$ is the expectation value of $*$.

We describe the data as a collection of discretely sampled waveforms, $X_i[\tau]$.

We assume that all signal times and shapes are already known, so we can model the waveforms by $X_i[\tau] = \sum_a M_{ia} Y_{ia}[\tau] + N_i[\tau] + b_i$, where Y is the shape of signal a on channel i , M is the magnitude of that signal, and N and b represent the electronic noise and baseline, respectively, of the channel.

To break the degeneracy between M and Y , we choose to fix the magnitude of the template signal Y . We choose to require that the signal Y has a magnitude of one, as described in figure 3.2. We assume that the expected magnitude of a signal on channel i from a single-site 2615-keV deposit is known, and is characterized as a function $L_i(\vec{x}, t)$ of the deposit position \vec{x} and calendar time t . The exact methods

for measuring $L_i(\vec{x}, t)$ will be described in chapter 5. In cases where a multi-site event deposits energy in multiple locations, we will use the charge information to estimate the energy deposited in each location; the estimated lightmap yield from such an event will be a weighted sum:

$$L_i^{MS}(\vec{x}_1, \dots, \vec{x}_{n_{max}}, t) = \frac{\sum_n E_n^{charge} L_i(\vec{x}_n, t)}{\sum_n E_n^{charge}}. \quad (3.1)$$

For notational simplicity, we will still characterize the expected yield on a gang i from a multi-site event as $L_i(\vec{x}, t)$; in practice it will always be clear how to compute the expected yields for any event from this function. We can thereby characterize the expected yields M_{ia} from an event with energy E_a as:

$$\langle M_{ia} \rangle = L_i(\vec{x}_a, t_a) E_a. \quad (3.2)$$

Noise correlations will be much simpler in frequency space, so we take the Fourier transform and drop the zero-frequency component to obtain

$$\tilde{X}_i[f] = \sum_a M_{ia} \tilde{Y}_{ia}[f] + \tilde{N}_i[f]. \quad (3.3)$$

As with the lightmap, we will assume that all correlations in the noise, of the form

$$\begin{aligned} & \left\langle \tilde{N}_i^R[f] \tilde{N}_j^R[g] \right\rangle \left\langle \tilde{N}_i^R[f] \tilde{N}_j^I[g] \right\rangle \\ & \left\langle \tilde{N}_i^I[f] \tilde{N}_j^R[g] \right\rangle \left\langle \tilde{N}_i^I[f] \tilde{N}_j^I[g] \right\rangle, \end{aligned} \quad (3.4)$$

are known; our means of measuring these correlations will be described in chapter 4.

3.2 The Signal Model

It is first important to characterize the response of the APDs to energy deposits in EXO-200. This will require us to understand the signal amplification of the detector

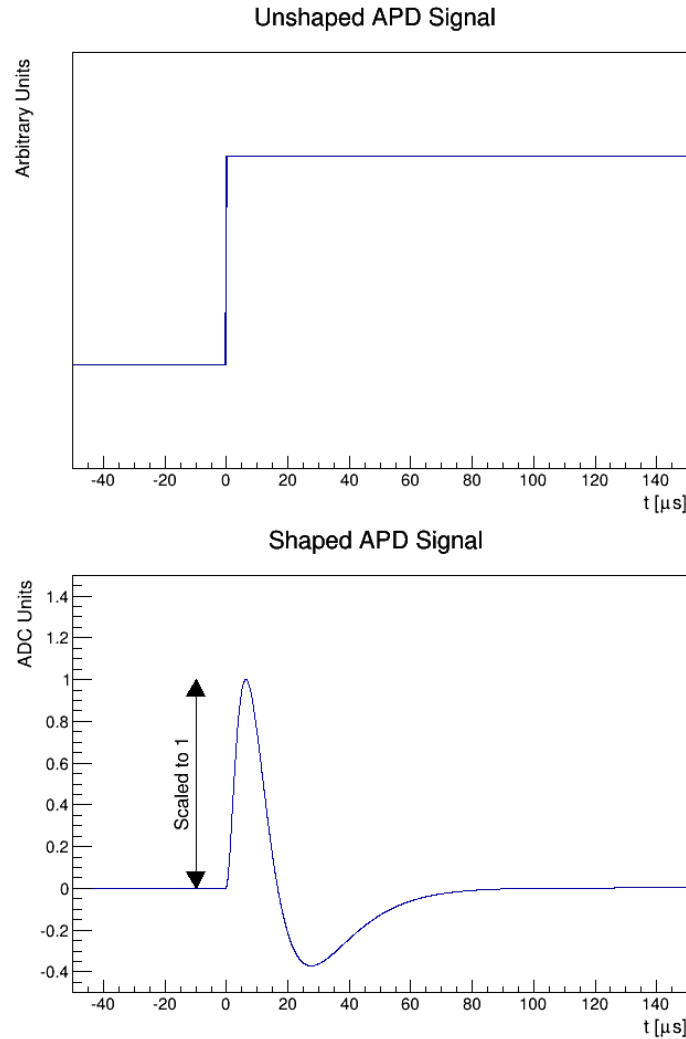


Figure 3.2: Shaped and unshaped APD waveforms. The normalization is shown to make the peak of the shaped waveform have a magnitude of one, and the time axis is shifted so that the unshaped waveform is a step function centered at $t = 0$.

at each physical stage, as well as the noise introduced by each of these processes.

We will describe both in detail here.

3.2.1 APD Noise

We will assume that there are two sources of noise in this model. First, the electronic noise $N_i[\tau]$ is assumed to be random. We require that noise with different frequencies is uncorrelated:

$$\langle \tilde{N}_i[f] \tilde{N}_j[g] \rangle = 0 \text{ when } f \neq g. \quad (3.5)$$

The noise correlations $\langle \tilde{N}_i[f] \tilde{N}_j[f] \rangle$ are assumed to be known; our means for measuring them are described in chapter 4.

The second random variable will be the magnitude of the signal itself, M_{ia} . When an energetic decay occurs in bulk of the detector, it will release some number of photons. We will denote the number of photons released by signal a by $P_a^{(0)}$, and this is the parameter we wish to measure. However, the magnitude signal actually observed on APD channels number of photons actually collected by sensors is a random variable whose distribution depends on $P_a^{(0)}$, and we will now identify the chain of events which produce it.

First, each APD gang i has some number $P_{ia}^{(1)}$ of photons which reach them. The mean fraction of photons reaching a particular gang i from position \vec{x}_a , $f_i(\vec{x}_a)$, is assumed to be known; however, the initial paths of the optical photons emitted from the source, their trajectories through the Xenon, and their success in reflecting off of teflon are all random, so we treat $P_{ia}^{(1)}$ as a Poisson-distributed random variable

with mean $f_i(\vec{x}_a)P_a^{(0)}$. A typical deposit from a $\beta\beta0\nu$ event may deposit up to roughly 1000 photons on a nearby APD gang, resulting in roughly 3% uncertainty from photon statistics; in the bulk of the Xenon, it may be that the largest single APD signal is only one-tenth of this size, resulting in closer to 10% uncertainty due to photon statistics on the nearest APD gang. Thus, we find that the Poisson noise on a single APD channel may be quite significant.

Additionally, the number of photons reaching different gangs are not uncorrelated; since a photon which reaches gang i cannot deposit on a different gang j , $P_{ia}^{(1)}$ and $P_{ja}^{(1)}$ are anticorrelated for different gangs $i \neq j$. This process is described by a multinomial distribution. Explicitly, we can identify the expectation values of a multinomial distribution:

$$\left\langle P_{ia}^{(1)} \right\rangle = f_i(\vec{x}_a)P_a^{(0)} \quad (3.6)$$

$$\left\langle P_{ia}^{(1)} P_{jb}^{(1)} \right\rangle = \left\langle P_{ia}^{(1)} \right\rangle \left\langle P_{jb}^{(1)} \right\rangle + [f_i(\vec{x}_a)\delta_{ij} - f_i(\vec{x}_a)f_j(\vec{x}_a)] P_a^{(0)}\delta_{ab} \quad (3.7)$$

(As a detail, we should note that the multinomial distribution is an incorrect model in one important respect: photons may reflect off of teflon one or more times on its way to the APD. Photons incident on the teflon may be absorbed, leading to a reflection efficiency which may be less than one. Furthermore, it is possible that teflon may be mildly fluorescent at the wavelength of our scintillation, leading to an increase in efficiency for reflection. As a result, photons which reflect off of teflon experience a combination of variances from each path photons travel and variances in each gain which they undergo. These conditional variances will always be larger than a simple Poisson distribution would indicate [53], so our variance estimate for

$P^{(1)}$ is probably an underestimate.)

Following the random process associated with photons reaching the APD gangs, there is also randomness associated with signal amplification internally in the APDs. These processes are described in detail in [44], but we can summarize that:

1. Optical photons in the liquid xenon arrive at the active layer of the APDs have a wavelength of roughly 178 nm, meaning that each optical photon has an energy of roughly 7.0 eV. The energy required to produce one electron-hole pair in silicon is roughly 3.66 eV, which means that each incident photon produces roughly 1.9 electron-hole pairs; we will define $P_{ia}^{(2)}$ to be the number of electron-hole pairs actually produced from $P_{ia}^{(1)}$ incident photons. The corresponding Fano factor for electrons produced in silicon is roughly 0.1, meaning that in addition to the uncertainty in $P_{ia}^{(1)}$ which we have already characterized, there is an additional uncorrelated variance in $P_{ia}^{(2)}$ equal to $0.1 \langle P_{ia}^{(2)} \rangle$. The correlations in the parameters $P_{ia}^{(2)}$ are therefore:

$$\langle P_{ia}^{(2)} \rangle = 1.9 \cdot P_{ia}^{(1)} \quad (3.8)$$

$$\langle P_{ia}^{(2)} P_{jb}^{(2)} \rangle = (1.9)^2 \langle P_{ia}^{(1)} P_{jb}^{(1)} \rangle + 0.1 \langle P_{ia}^{(2)} \rangle \delta_{ij} \delta_{ab} \quad (3.9)$$

2. Electron-hole pairs are then amplified by an avalanche process inside the APDs. The magnitude of this gain is APD-dependent, generally on the order of $200 - 300$, and can be identified by a time-dependent quantity $G_i^P(t)$; we will call the number of output electrons $P_{ia}^{(3)}$. In addition to amplification of existing noise in $P_{ia}^{(2)}$, two additional source of noise are introduced. First,

there is statistical variance in the amplification experienced by each electron due to the randomness of the avalanche process. This variance is dependent on many factors, including the gain, and scales like the square root of the number of electrons; we define the variance on the gain experienced by a single electron as $\sigma_{G_i}^2(t)$. From [44], $\sigma_{G_i}^2(t)$ is approximately equal to $(G_i^P(t))^2$ when $G_i^P(t) = 100$; as a result, we approximate $\sigma_{G_i}^2(t) \approx (G_i^P(t))^2$. Second, there are gain non-uniformities in the diode volume, which contribute variance proportional to the square of the number of initial electron-hole pairs; we will identify the proportionality constant as σ_{NU}^2 , which may depend on time and APD gang. The magnitude of this uncertainty is not well-known, but may be significant. Our current code base treats σ_{NU}^2 as zero; however, future analyses will likely attempt to estimate it, and the derivation which follows will retain it as an aid to that anticipated work. The correlations in the parameters $P_{ia}^{(3)}$ are therefore:

$$\langle P_{ia}^{(3)} \rangle = G_i^P(t_a) P_{ia}^{(2)} \quad (3.10)$$

$$\langle P_{ia}^{(3)} P_{jb}^{(3)} \rangle = G_i^P(t_a) G_j^P(t_b) \langle P_{ia}^{(2)} P_{jb}^{(2)} \rangle + \left[P_{ia}^{(2)} \sigma_{G_i}^2(t_a) + (P_{ia}^{(2)})^2 \sigma_{NU}^2 \right] \delta_{ij} \delta_{ab} \quad (3.11)$$

My thinking on non-uniformities has evolved a little bit – clarify in this section

why it's such a big deal.

Finally, there is amplification

$$M_{ia} = G_i^E(t) P_{ia}^{(3)} \quad (3.12)$$

associated with the electronics of the APDs which is dependent on time and channel. This includes preamplifier gain, shaper gain, gain associated with the shaping times, and conversion from voltage to ADC counts. We assume that no signal-dependent noise is introduced during this stage, but there is constant electronic noise $N_i[\tau]$ which has been described above. Additionally, the APDs can contribute noise in the form of a dark current which is uncorrelated with signals; this is inseparable from the electronic noise, and so we absorb it into our description of $N_i[\tau]$.

3.2.2 APD Signals and Noise

We have already characterized the overall gain of the APDs using the lightmap described earlier. We know that a typical single-site deposit of 2615 keV at position \vec{x} and time t will produce a signal with expected magnitude $L_i(\vec{x}, t)$ on APD channel i . We must now connect this empirical understanding of our APD signals with the physical understanding in terms of photons and electrons described above.

We have identified the number of photons created by an event a as $P_a^{(0)}$. In reality, an ideal scintillation measurement can only measure this quantity, and not the true energy of the event – there is randomness in the number of photons produced by a known-energy deposit, so $P_a^{(0)}$ will not be perfectly correlated with the energy E_a of the event. However, the number of photons generated is a difficult parameter to understand empirically, and all of our calibrations occur at a known energy even though the corresponding number of deposited photons is unknown.

Simulations using NEST [54] which have been performed within the EXO

group by Liangjian Wen at our bulk electric field indicate that we can expect roughly 82,000 photons from a 2615-keV gamma deposit. We will identify this parameter with c , and express the average relation between energy and photon yield in EXO-200 by

$$P^{(0)} = c \cdot E, \quad (3.13)$$

where E is the energy measured in units of 2615 keV. We will treat this relationship as exact, and attempt to measure E rather than $P^{(0)}$; this means that when we speak of measuring the energy of an event using the APD signals, we really are referring to measuring the “scintillation energy,” or a parameter proportional to the number of emitted photons which on average will equal the true energy of the deposit.

Ignoring variances for a moment, we can combine equations 3.6, 3.8, 3.10, 3.12, and 3.13 to state that on average,

$$M_{ia} = 1.9 \cdot c f_i(\vec{x}_a) G_i^P(t_a) G_i^E(t_a) E_a.$$

We can compare this to our empirical lightmap measurements, which are expressed by $M_{ia} = L_i(\vec{x}_a, t_a) E_a$, and we conclude that:

$$L_i(\vec{x}, t) = 1.9 \cdot c f_i(\vec{x}) G_i^P(t) G_i^E(t). \quad (3.14)$$

We recall that it is assumed the lightmap is a separable function, $L_i(\vec{x}, t) = R_i(\vec{x}) S_i(t)$, and we can provide the two proportionalities:

$$R_i(\vec{x}) \propto f_i(\vec{x})$$

$$S_i(t) \propto G_i^P(t) G_i^E(t).$$

Although $G_i^E(t)$ is in principle time-dependent, due to environmental effects on the APD electronics and occasional replacement of electronics cards for certain channels, precision data on its value is not readily available. Instead, we use a time-independent estimate

$$G_i^E(t) = 1.1 \cdot 10^{-3} \quad (3.15)$$

ADC counts per electron emitted from the APD; the uncertainty in this figure is dominated by uncertainty in the preamplifier gains, which are controlled by a roughly 5 pF capacitor. Other contributors to the gain include shaper gain of 21.2 (from a combination of amplification and shaping) and a full-scale digitizer range of 2.5 volts for 12-bit digitization.

We do have independent measurements of the APD gains $G_i^P(t)$ available from laser calibration runs. These special runs allow a laser to shine into the detector from a fixed point and with a stable amplitude while the bias voltages on the APDs are varied from an effective unity gain to our standard voltage settings. Using these measurements, we are able to measure $G_i^P(t)$ at weekly intervals from September 2012 to the present time. Before September 2012, some less-reliable laser data is available, but results from that data are not readily available as of this writing.

It would be possible, and should be a goal for future improvements, to make use of this full range of laser data. However, the laser data provides a less uniform history of APD gains over the full data-taking window of EXO-200 from September 2011 to November 2013, and it is much easier to track time-dependent behavior from Thorium source data which have been collected regularly throughout that period.

As a result, a compromise is used to characterize $G_i^P(t)$. One particular laser run, run 4540 (taken on December 13, 2012), is used to fix $G_i^P(t_{4540})$, and the function is extrapolated using Thorium source data with:

$$G_i^P(t) \approx G_i^P(t_{4540}) \cdot S_i(t)/S_i(t_{4540}).$$

This assumption makes use of the approximation that $G_i^E(t)$ is roughly constant in time, which is probably only accurate to one significant figure; therefore when an electronics change is made to a channel, we can expect that the accuracy of $G_i^P(t)$ is no better than one significant figure. These results mean that we can also estimate with the same level of accuracy:

$$f_i(\vec{x}) \approx \frac{S_i(t_{4540})}{G_i^P(t_{4540})} \cdot \frac{R_i(\vec{x})}{1.9 \cdot c G_i^E(t)}.$$

It is then possible to express the full correlations in signal magnitudes in terms of the scintillation energies of deposits as:

$$\langle M_{ia} \rangle = L_i(\vec{x}_a, t_a) E_a \quad (3.16)$$

$$\begin{aligned} \langle M_{ia} M_{jb} \rangle &= L_i(\vec{x}_a, t_a) L_j(\vec{x}_b, t_b) E_a E_b \left[1 + \frac{\sigma_{NU}^2}{(G_i^P(t))^2} \delta_{ij} \delta_{ab} \right] \\ &\quad - L_i(\vec{x}_a, t_a) L_j(\vec{x}_a, t_a) E_a \delta_{ab}/c \\ &\quad + L_i(\vec{x}_a, t_a) G_i^E(t) E_a \delta_{ij} \delta_{ab} \left[(0.1 + 1.9) G_i^P(t) + \frac{\sigma_{G_i}^2(t)}{G_i^P(t)} \right]. \end{aligned} \quad (3.17)$$

We combine this with our knowledge of the noise coefficients:

$$\begin{aligned} \langle \tilde{N}_i[f] \rangle &= 0 \\ \langle \tilde{N}_i[f] \tilde{N}_j[g] \rangle &= \begin{cases} 0 & \text{if } f \neq g \\ \text{known} & \text{if } f = g \end{cases} \end{aligned}$$

and can claim to now have a complete description of the signals and noise observed in the APD channels.

3.3 Derivation

It is now possible to specify the optimization criteria for generating an energy estimate from the APD signals. We wish to identify an energy estimator which is unbiased and has a minimal expected error. For the problem to remain tractable, we will demand that the operator be linear. Furthermore, although the Fourier-transformed waveforms $\tilde{X}_i[f]$ are complex-valued, we will require that the energy estimate be strictly real-valued.

We will therefore take the energy estimator to be of the form:

$$\hat{E}_a = \sum_{if} A_{ifa} \tilde{X}_i^R[f] + B_{ifa} \tilde{X}_i^I[f]. \quad (3.18)$$

The goal of denoising is therefore reduced to identifying the optimal parameters A_{ifa} and B_{ifa} for this estimator.

The error in the energy estimate \hat{E}_a of E_a is defined by:

$$\epsilon_a^2 = \left\langle \left(\hat{E}_a - E_a \right)^2 \right\rangle. \quad (3.19)$$

Our goal is then to minimize ϵ_a^2 under the constraint of no bias, ie. that:

$$\left\langle \hat{E}_a - E_a \right\rangle = 0 \quad (3.20)$$

or, equivalently,

$$\sum_{ifb} \left[A_{ifa} \tilde{Y}_{ib}^R[f] + B_{ifa} \tilde{Y}_{ib}^I[f] \right] L_i(\vec{x}_b, t_b) E_b = E_a.$$

However, we will find that it is necessary to specify a slightly stronger constraint. In particular, it will be desirable to ensure that the constraints are as independent of energy as possible to reduce the need to input an estimated energy into our energy estimator; therefore we will freely employ the stronger constraint

$$\sum_{if} \left[A_{ifa} \tilde{Y}_{ib}^R[f] + B_{ifa} \tilde{Y}_{ib}^I[f] \right] L_i(\vec{x}_b, t_b) = \delta_{ab} \text{ for all } b, \quad (3.21)$$

which implies the earlier forms and leads to advantageous cancellations of terms.

We now proceed with the optimization. We start by expanding ϵ_a^2 :

$$\begin{aligned} \epsilon_a^2 &= \left\langle \left(\hat{E}_a - E_a \right)^2 \right\rangle \\ &= \left\langle \hat{E}_a^2 \right\rangle - E_a \left\langle \hat{E}_a \right\rangle - \left\langle \hat{E}_a - E_a \right\rangle E_a \end{aligned}$$

We can employ the constraint of equation 3.20 to simplify the second term of this expansion, and eliminate the third altogether; we then proceed:

$$\begin{aligned} \epsilon_a^2 &= \left\langle \hat{E}_a^2 \right\rangle - E_a^2 \\ &= \left\langle \left(\sum_{if} \left[A_{ifa} \tilde{X}_i^R[f] + B_{ifa} \tilde{X}_i^I[f] \right] \right)^2 \right\rangle - E_a^2 \\ &= \left\langle \left(\sum_{if} \left[A_{ifa} \tilde{N}_i^R[f] + B_{ifa} \tilde{N}_i^I[f] \right] \right. \right. \\ &\quad \left. \left. + \sum_{ifb} \left[A_{ifa} \tilde{Y}_{ib}^R[f] + B_{ifa} \tilde{Y}_{ib}^I[f] \right] M_{ib} \right)^2 \right\rangle - E_a^2 \end{aligned}$$

The noise \tilde{N} and signal M_{ia} are uncorrelated, so multiplicative cross-terms will have an expectation value of zero:

$$\begin{aligned} \epsilon_a^2 &= \left\langle \left(\sum_{if} \left[A_{ifa} \tilde{N}_i^R[f] + B_{ifa} \tilde{N}_i^I[f] \right] \right)^2 \right\rangle \\ &\quad + \left\langle \left(\sum_{ifb} \left[A_{ifa} \tilde{Y}_{ib}^R[f] + B_{ifa} \tilde{Y}_{ib}^I[f] \right] M_{ib} \right)^2 \right\rangle - E_a^2 \end{aligned}$$

Additionally, electronic noise cross-terms between different frequencies will not survive:

$$\begin{aligned}
\epsilon_a^2 &= \left\langle \sum_{ijf} \left[A_{ifa} \tilde{N}_i^R[f] + B_{ifa} \tilde{N}_i^I[f] \right] \left[A_{jfa} \tilde{N}_j^R[f] + B_{jfa} \tilde{N}_j^I[f] \right] \right\rangle \\
&\quad + \left\langle \left(\sum_{ifb} \left[A_{ifa} \tilde{Y}_{ib}^R[f] + B_{ifa} \tilde{Y}_{ib}^I[f] \right] M_{ib} \right)^2 \right\rangle - E_a^2 \\
&= \sum_{ijf} \left[A_{ifa} A_{jfa} \left\langle \tilde{N}_i^R[f] \tilde{N}_j^R[f] \right\rangle + A_{ifa} B_{jfa} \left\langle \tilde{N}_i^R[f] \tilde{N}_j^I[f] \right\rangle \right. \\
&\quad \left. + B_{ifa} A_{jfa} \left\langle \tilde{N}_i^I[f] \tilde{N}_j^R[f] \right\rangle + B_{ifa} B_{jfa} \left\langle \tilde{N}_i^I[f] \tilde{N}_j^I[f] \right\rangle \right] \\
&\quad + \sum_{\substack{ifb \\ jgc}} \left[A_{ifa} \tilde{Y}_{ib}^R[f] + B_{ifa} \tilde{Y}_{ib}^I[f] \right] \left[A_{jga} \tilde{Y}_{jc}^R[g] + B_{jga} \tilde{Y}_{jc}^I[g] \right] \langle M_{ib} M_{jc} \rangle - E_a^2
\end{aligned}$$

We will now expand $\langle M_{ib}M_{jc} \rangle$ using equation 3.17 and take advantage of the stronger form of our constraint 3.21 to simplify the expression:

$$\begin{aligned}
\epsilon_a^2 &= \sum_{ijf} \left[A_{ifa}A_{jfa} \left\langle \tilde{N}_i^R[f] \tilde{N}_j^R[f] \right\rangle + A_{ifa}B_{jfa} \left\langle \tilde{N}_i^R[f] \tilde{N}_j^I[f] \right\rangle \right. \\
&\quad \left. + B_{ifa}A_{jfa} \left\langle \tilde{N}_i^I[f] \tilde{N}_j^R[f] \right\rangle + B_{ifa}B_{jfa} \left\langle \tilde{N}_i^I[f] \tilde{N}_j^I[f] \right\rangle \right] \\
&\quad + \left(\sum_{ifb} \left[A_{ifa} \tilde{Y}_{ib}^R[f] + B_{ifa} \tilde{Y}_{ib}^I[f] \right] L_i(\vec{x}_b, t_b) E_b \right)^2 - E_a^2 \\
&\quad - \sum_b \left(\sum_{if} \left[A_{ifa} \tilde{Y}_{ib}^R[f] + B_{ifa} \tilde{Y}_{ib}^I[f] \right] L_i(\vec{x}_b, t_b) \right)^2 \frac{E_b}{c} \\
&\quad + \sum_{ifgb} \left[A_{ifa} \tilde{Y}_{ib}^R[f] + B_{ifa} \tilde{Y}_{ib}^I[f] \right] \left[A_{iga} \tilde{Y}_{ib}^R[g] + B_{iga} \tilde{Y}_{ib}^I[g] \right] \cdot \\
&\quad L_i(\vec{x}_b, t_b) E_b \left[(0.1 + 1.9) G_i^E(t_b) G_i^P(t_b) \right. \\
&\quad \left. + \frac{G_i^E(t_b)}{G_i^P(t_b)} \sigma_{G_i}^2(t_b) + L_i(\vec{x}_b, t_b) E_b \frac{\sigma_{NU}^2}{(G_i^P(t_b))^2} \right] \\
&= \sum_{ijf} \left[A_{ifa}A_{jfa} \left\langle \tilde{N}_i^R[f] \tilde{N}_j^R[f] \right\rangle + A_{ifa}B_{jfa} \left\langle \tilde{N}_i^R[f] \tilde{N}_j^I[f] \right\rangle \right. \\
&\quad \left. + B_{ifa}A_{jfa} \left\langle \tilde{N}_i^I[f] \tilde{N}_j^R[f] \right\rangle + B_{ifa}B_{jfa} \left\langle \tilde{N}_i^I[f] \tilde{N}_j^I[f] \right\rangle \right] \\
&\quad + \sum_{ib} \left(\sum_f \left[A_{ifa} \tilde{Y}_{ib}^R[f] + B_{ifa} \tilde{Y}_{ib}^I[f] \right] \right)^2 \cdot \\
&\quad L_i(\vec{x}_b, t_b) E_b \left[(0.1 + 1.9) G_i^E(t_b) G_i^P(t_b) \right. \\
&\quad \left. + \frac{G_i^E(t_b)}{G_i^P(t_b)} \sigma_{G_i}^2(t_b) + L_i(\vec{x}_b, t_b) E_b \frac{\sigma_{NU}^2}{(G_i^P(t_b))^2} \right] \\
&\quad - \frac{E_a}{c}
\end{aligned}$$

We are now in a position to evaluate the partial derivatives of ϵ_a^2 with respect

to the parameters A_{ifa} and B_{ifa} . They are:

$$\begin{aligned} \frac{\partial \epsilon_a^2}{\partial A_{ifa}} &= 2 \sum_j \left[A_{jfa} \left\langle \tilde{N}_i^R[f] \tilde{N}_j^R[f] \right\rangle + B_{jfa} \left\langle \tilde{N}_i^R[f] \tilde{N}_j^I[f] \right\rangle \right] \\ &\quad + 2 \sum_{gb} E_b \tilde{Y}_{ib}^R[f] L_i(\vec{x}_b, t_b) \left[A_{iga} \tilde{Y}_{ib}^R[g] + B_{iga} \tilde{Y}_{ib}^I[g] \right] \cdot \\ &\quad \left[(0.1 + 1.9) G_i^E(t_b) G_i^P(t_b) \right. \\ &\quad \left. + \frac{G_i^E(t_b)}{G_i^P(t_b)} \sigma_{G_i}^2(t_b) + L_i(\vec{x}_b, t_b) E_b \frac{\sigma_{NU}^2}{(G_i^P(t_b))^2} \right] \\ \frac{\partial \epsilon_a^2}{\partial B_{ifa}} &= 2 \sum_j \left[A_{jfa} \left\langle \tilde{N}_i^I[f] \tilde{N}_j^R[f] \right\rangle + B_{jfa} \left\langle \tilde{N}_i^I[f] \tilde{N}_j^I[f] \right\rangle \right] \\ &\quad + 2 \sum_{gb} E_b \tilde{Y}_{ib}^I[f] L_i(\vec{x}_b, t_b) \left[A_{iga} \tilde{Y}_{ib}^R[g] + B_{iga} \tilde{Y}_{ib}^I[g] \right] \cdot \\ &\quad \left[(0.1 + 1.9) G_i^E(t_b) G_i^P(t_b) \right. \\ &\quad \left. + \frac{G_i^E(t_b)}{G_i^P(t_b)} \sigma_{G_i}^2(t_b) + L_i(\vec{x}_b, t_b) E_b \frac{\sigma_{NU}^2}{(G_i^P(t_b))^2} \right] \end{aligned}$$

We will use Lagrange's method to minimize ϵ_a^2 while satisfying our constraints; we define

$$C_{ab} = \sum_{if} \left[A_{ifa} \tilde{Y}_{ib}^R[f] + B_{ifa} \tilde{Y}_{ib}^I[f] \right] L_i(\vec{x}_b, t_b),$$

with ordered indices, and restate the constraints of equation 3.21 as

$$C_{ab} = \delta_{ab}.$$

Then, the partial derivatives of these constrained expressions are:

$$\begin{aligned} \frac{\partial C_{bc}}{\partial A_{ifa}} &= \tilde{Y}_{ic}^R[f] L_i(\vec{x}_c, t_c) \delta_{ab} \\ \frac{\partial C_{bc}}{\partial B_{ifa}} &= \tilde{Y}_{ic}^I[f] L_i(\vec{x}_c, t_c) \delta_{ab} \end{aligned}$$

Denoting the set of Lagrange multipliers for ϵ_a^2 with λ_{ab} , where the indices are ordered, and allowing these parameters to absorb constant factors, we can at last

identify the full set of linear equations describing the optimal energy estimator \widehat{E}_a :

$$\begin{aligned}
& \sum_j \left[A_{jfa} \left\langle \widetilde{N}_i^R[f] \widetilde{N}_j^R[f] \right\rangle + B_{jfa} \left\langle \widetilde{N}_i^R[f] \widetilde{N}_j^I[f] \right\rangle \right] \\
& + \sum_{gb} E_b \widetilde{Y}_{ib}^R[f] L_i(\vec{x}_b, t_b) \left[A_{iga} \widetilde{Y}_{ib}^R[g] + B_{iga} \widetilde{Y}_{ib}^I[g] \right] \cdot \\
& \quad \left[(0.1 + 1.9) G_i^E(t_b) G_i^P(t_b) + \frac{G_i^E(t_b)}{G_i^P(t_b)} \sigma_{G_i}^2(t_b) + L_i(\vec{x}_b, t_b) E_b \frac{\sigma_{NU}^2}{(G_i^P(t_b))^2} \right] \\
& + \sum_b \lambda_{ab} \widetilde{Y}_{ib}^R[f] L_i(\vec{x}_b, t_b) = 0 \quad \text{for each } i, f \\
& \sum_j \left[A_{jfa} \left\langle \widetilde{N}_i^I[f] \widetilde{N}_j^R[f] \right\rangle + B_{jfa} \left\langle \widetilde{N}_i^I[f] \widetilde{N}_j^I[f] \right\rangle \right] \\
& + \sum_{gb} E_b \widetilde{Y}_{ib}^I[f] L_i(\vec{x}_b, t_b) \left[A_{iga} \widetilde{Y}_{ib}^R[g] + B_{iga} \widetilde{Y}_{ib}^I[g] \right] \cdot \\
& \quad \left[(0.1 + 1.9) G_i^E(t_b) G_i^P(t_b) + \frac{G_i^E(t_b)}{G_i^P(t_b)} \sigma_{G_i}^2(t_b) + L_i(\vec{x}_b, t_b) E_b \frac{\sigma_{NU}^2}{(G_i^P(t_b))^2} \right] \\
& + \sum_b \lambda_{ab} \widetilde{Y}_{ib}^I[f] L_i(\vec{x}_b, t_b) = 0 \quad \text{for each } i, f \\
& \sum_{if} \left[A_{ifa} \widetilde{Y}_{ib}^R[f] + B_{ifa} \widetilde{Y}_{ib}^I[f] \right] L_i(\vec{x}_b, t_b) = \delta_{ab} \quad \text{for each } b
\end{aligned}$$

To simplify the notation, let us define a new function:

$$\begin{aligned}
q(i, b) := & \left((0.1 + 1.9) G_i^E(t_b) G_i^P(t_b) + \frac{G_i^E(t_b)}{G_i^P(t_b)} \sigma_{G_i}^2(t_b) \right. \\
& \left. + L_i(\vec{x}_b, t_b) E_b \frac{\sigma_{NU}^2}{(G_i^P(t_b))^2} \right) L_i(\vec{x}_b, t_b) E_b
\end{aligned} \tag{3.22}$$

which we note should be strictly positive if measured correctly (because all gains and lightmap values should be strictly positive, and all variances are non-negative).

Using this shorthand, we can re-write our system of equations in the more compact

form:

$$\begin{aligned} & \sum_j \left[A_{jfa} \left\langle \tilde{N}_i^R[f] \tilde{N}_j^R[f] \right\rangle + B_{jfa} \left\langle \tilde{N}_i^R[f] \tilde{N}_j^I[f] \right\rangle \right] \\ & + \sum_{gb} \tilde{Y}_{ib}^R[f] q(i, b) \left[A_{iga} \tilde{Y}_{ib}^R[g] + B_{iga} \tilde{Y}_{ib}^I[g] \right] \\ & + \sum_b \lambda_{ab} \tilde{Y}_{ib}^R[f] L_i(\vec{x}_b, t_b) = 0 \quad \text{for each } i, f \end{aligned} \quad (3.23a)$$

$$\begin{aligned} & \sum_j \left[A_{jfa} \left\langle \tilde{N}_i^I[f] \tilde{N}_j^R[f] \right\rangle + B_{jfa} \left\langle \tilde{N}_i^I[f] \tilde{N}_j^I[f] \right\rangle \right] \\ & + \sum_{gb} \tilde{Y}_{ib}^I[f] q(i, b) \left[A_{iga} \tilde{Y}_{ib}^R[g] + B_{iga} \tilde{Y}_{ib}^I[g] \right] \\ & + \sum_b \lambda_{ab} \tilde{Y}_{ib}^I[f] L_i(\vec{x}_b, t_b) = 0 \quad \text{for each } i, f \end{aligned} \quad (3.23b)$$

$$\sum_{if} \left[A_{ifa} \tilde{Y}_{ib}^R[f] + B_{ifa} \tilde{Y}_{ib}^I[f] \right] L_i(\vec{x}_b, t_b) = \delta_{ab} \quad \text{for each } b \quad (3.23c)$$

It is important to note here that energies E_b , which we are intending to measure, do in fact enter into this linear set of equations. At first this would seem to demonstrate that the equations here are impossible to apply, but in fact they remind us that the forms of noise which are correlated with the signal are also dependent on the magnitude of that signal. Statistical fluctuations in the number of photons observed on each APD, for instance, scale like the square root of the number of photons emitted.

We can see, then, that some estimate of energy is necessary to know the relative importance of different forms of noise. But the constraint equation does ensure that our estimate will be unbiased regardless of what energy estimates are fed into the system of equations, so we can be confident that it is only a rough estimate of the energy scale which is needed, and not worry that the optimization will be biased to

estimate energies similar to the estimates we feed in. For this purpose, it is sufficient to use the charge-only energy as an estimate of the scintillation-only energy.

3.4 Matrix Version

Because the system of equations above is linear in A_{ifa} and B_{ifa} , we wish to solve it as a matrix equation. This requires, first, that we choose an ordering of the unknowns; the best ordering will be the one which groups nonzero entries into blocks, since this will allow us to make more efficient use of matrix libraries. We define:

$$\vec{A}_a = (A_{11a}, B_{11a}, A_{21a}, B_{21a}, \dots, B_{i_{max}1a}, A_{12a}, \dots, A_{1f_{max}a}, A_{2f_{max}a}, \dots, A_{i_{max}f_{max}a}) \quad (3.24)$$

so that the entries alternate between A and B , iterating quickly through channels and more slowly through frequencies. Note that only the A terms are included for the maximum frequency; this is because $X_i[t]$ is real-valued, so $\tilde{X}_i[0]$ and $\tilde{X}_i[f_{max}]$ are real-valued as well. We also will find it convenient to define the matrix:

$$\mathbf{A} = \begin{pmatrix} \vdots & & \vdots \\ \vec{A}_1 & \dots & \vec{A}_{a_{max}} \\ \vdots & & \vdots \end{pmatrix} \quad (3.25)$$

which includes the parameters needed for each of the estimators \hat{E}_a .

We can then define the electronic noise blocks as:

$$\mathbf{N}_f = \begin{cases} \text{COV} \left(\tilde{N}_1^R[f], \tilde{N}_1^I[f], \tilde{N}_2^R[f], \dots, \tilde{N}_{i_{max}}^I[f] \right) & \text{for } f < f_{max} \\ \text{COV} \left(\tilde{N}_1^R[f], \tilde{N}_2^R[f], \dots, \tilde{N}_{i_{max}}^R[f] \right) & \text{for } f = f_{max} \end{cases} \quad (3.26)$$

where \mathbf{COV} specifies the covariance matrix of an ordered list of random variables,

$$\mathbf{COV}(x_1, x_2, \dots, x_n) = \begin{pmatrix} cov(x_1x_1) & cov(x_1x_2) & \cdots & cov(x_1x_n) \\ cov(x_2x_1) & cov(x_2x_2) & \cdots & cov(x_2x_n) \\ \vdots & \vdots & \ddots & \vdots \\ cov(x_nx_1) & cov(x_nx_2) & \cdots & cov(x_nx_n) \end{pmatrix}. \quad (3.27)$$

Note that because our noise variables $\tilde{N}_i^R[f]$ and $\tilde{N}_i^I[f]$ have mean zero, we can move smoothly between expectation values of products and covariances:

$$\begin{aligned} cov(\tilde{N}_i^R[f], \tilde{N}_j^R[f]) &= \langle \tilde{N}_i^R[f] \tilde{N}_j^R[f] \rangle \\ cov(\tilde{N}_i^R[f], \tilde{N}_j^I[f]) &= \langle \tilde{N}_i^R[f] \tilde{N}_j^I[f] \rangle \\ cov(\tilde{N}_i^I[f], \tilde{N}_j^R[f]) &= \langle \tilde{N}_i^I[f] \tilde{N}_j^R[f] \rangle \\ cov(\tilde{N}_i^I[f], \tilde{N}_j^I[f]) &= \langle \tilde{N}_i^I[f] \tilde{N}_j^I[f] \rangle. \end{aligned} \quad (3.28)$$

We pack together the blocks of equation 3.26 into a sparse noise matrix:

$$\mathbf{N} = \begin{pmatrix} \mathbf{N}_1 & \mathbf{0} & \dots & \mathbf{0} \\ \mathbf{0} & \mathbf{N}_2 & \dots & \mathbf{0} \\ \vdots & \vdots & \ddots & \vdots \\ \mathbf{0} & \mathbf{0} & \dots & \mathbf{N}_{f_{\max}} \end{pmatrix}. \quad (3.29)$$

In a similar way, we can define the other noise terms in terms of matrix operations. We will find that it is possible to describe the noise terms correlated with signals as a product of two matrices, $\mathbf{P} = \mathbf{P}_1 \mathbf{P}_2$. First we define the matrix \mathbf{P}_1 , which steps horizontally through the APD channels and signals. For a particular

choice of indices j, b , the corresponding column of \mathbf{P}_1 will be:

$$\mathbf{P}_1(\text{column } j, b) = \begin{pmatrix} \tilde{Y}_{jb}^R[1]\delta_{1j} \\ \tilde{Y}_{jb}^I[1]\delta_{1j} \\ \tilde{Y}_{jb}^R[1]\delta_{2j} \\ \vdots \\ \tilde{Y}_{jb}^I[1]\delta_{i_{max}j} \\ \tilde{Y}_{jb}^R[2]\delta_{1j} \\ \vdots \\ \tilde{Y}_{jb}^R[f_{max}]\delta_{1j} \\ \tilde{Y}_{jb}^R[f_{max}]\delta_{2j} \\ \vdots \\ \tilde{Y}_{jb}^R[f_{max}]\delta_{i_{max}j} \end{pmatrix} \sqrt{q(j, b)}. \quad (3.30)$$

Note that in each column, only a small subset of the entries are nonzero.

This means that \mathbf{P}_2 should be a matrix with rows that step through the APD channels and signals as well. For a particular choice of indices j, b , the corresponding row of \mathbf{P}_2 will be:

$$\mathbf{P}_2(\text{row } j, b) = \begin{pmatrix} \tilde{Y}_{jb}^R[1]\delta_{1j} & \tilde{Y}_{jb}^I[1]\delta_{1j} & \tilde{Y}_{jb}^R[1]\delta_{2j} & \cdots & \tilde{Y}_{jb}^I[1]\delta_{i_{max}j} & \tilde{Y}_{jb}^R[2]\delta_{1j} & \cdots \\ \cdots & \tilde{Y}_{jb}^R[f_{max}]\delta_{1j} & \tilde{Y}_{jb}^R[f_{max}]\delta_{2j} & \cdots & \tilde{Y}_{jb}^R[f_{max}]\delta_{i_{max}j} \end{pmatrix} \sqrt{q(j, b)}. \quad (3.31)$$

Since we will be using the product $\mathbf{P} = \mathbf{P}_1 \mathbf{P}_2$, it clearly must be the case that the ordering of columns in \mathbf{P}_1 is the same as the ordering of rows in \mathbf{P}_2 . Because in practice there will always be more APD channels than APD signals, it will generally

be advantageous to iterate through j fastest, and step through b more slowly. We can also see that $\mathbf{P}_1 = \mathbf{P}_2^\top$, so

$$\mathbf{P} = \mathbf{P}_2^\top \mathbf{P}_2. \quad (3.32)$$

The constraint equations are represented by a matrix \mathbf{C} with rows that step through the APD signals; for a particular choice of b the corresponding row of \mathbf{C} will be:

$$\begin{aligned} \mathbf{C}(\text{row } b) = & \begin{pmatrix} \tilde{Y}_{1b}^R[1]L_1(\vec{x}_b, t_b) & \tilde{Y}_{1b}^I[1]L_1(\vec{x}_b, t_b) & \tilde{Y}_{2b}^R[1]L_2(\vec{x}_b, t_b) \\ \dots & \tilde{Y}_{i_{max}b}^I[1]L_{i_{max}}(\vec{x}_b, t_b) & \tilde{Y}_{1b}^R[2]L_1(\vec{x}_b, t_b) \\ \dots & \tilde{Y}_{1b}^R[f_{max}]L_1(\vec{x}_b, t_b) & \tilde{Y}_{2b}^R[f_{max}]L_2(\vec{x}_b, t_b) \\ & \dots & \tilde{Y}_{i_{max}b}^R[f_{max}]L_{i_{max}}(\vec{x}_b, t_b) \end{pmatrix}. \end{aligned} \quad (3.33)$$

Finally it is possible to restate the full linear equation specified above in matrix form, where we can simultaneously include the equations for all of the estimators \hat{E}_a :

$$\begin{pmatrix} \mathbf{N} + \mathbf{P} & \mathbf{C}^\top \\ \mathbf{C} & \mathbf{0} \end{pmatrix} \mathbf{A} = \begin{pmatrix} \mathbf{0} \\ \mathbf{I} \end{pmatrix}. \quad (3.34)$$

The matrix \mathbf{N} is the same as the covariance matrix of the electronic noise, so it must be symmetric and positive-semidefinite. Similarly, we have seen that $\mathbf{P} = \mathbf{P}_2^\top \mathbf{P}_2$, implying that \mathbf{P} must be symmetric and positive-semidefinite. This means that there is a Cholesky decomposition $\mathbf{N} + \mathbf{P} = \mathbf{L}\mathbf{L}^\top$, where \mathbf{L} is a lower-triangular matrix, and that $\mathbf{N} + \mathbf{P}$ is symmetric and positive semi-definite. This implies that the full matrix equation is symmetric; however, it is insufficient for

showing that the full system is positive semi-definite, and in fact we will see that this is not the case.

We also note the important observation that this matrix is sparse. Given roughly 1000 frequency components in our signals, only 0.1% of the entries of \mathbf{N} are non-zero. And with 70 APD channels and only a small number of signals we wish to denoise, the combined number of non-zero entries in \mathbf{P}_1 and \mathbf{P}_2 is easily an order of magnitude less than the number of non-zero entries in \mathbf{N} . As a result, we can conclude that this matrix is extremely sparse, and should ensure that whatever method we use to solve these equations takes advantage of this sparsity.

3.5 Preconditioning

We have specified a matrix equation which we now wish to solve. However, it is generally recommended that large matrix equations should not be solved directly. Instead, it is recommended that the matrix should be preconditioned. This means that if a matrix equation $\mathbf{A}\vec{x} = \vec{b}$ should be solved, one should first find a matrix \mathbf{A}' which is approximately equal to \mathbf{A} and which is easily invertible. Finding the right balance between the quality of the approximation $\mathbf{A}' \approx \mathbf{A}$ and the difficulty of computing the inverse $(\mathbf{A}')^{-1}$ is more art than science, but we will present here a preconditioning matrix which seems to strike a good balance for this particular system.

The matrix equation we wish to solve takes the form:

$$\begin{pmatrix} \mathbf{N} + \mathbf{P} & \mathbf{C}^\top \\ \mathbf{C} & \mathbf{0} \end{pmatrix} \mathbf{A} = \begin{pmatrix} \mathbf{0} \\ \mathbf{I} \end{pmatrix}$$

Let us define $\mathbf{D} = \text{diag}(\mathbf{N})$ and approximate

$$\begin{pmatrix} \mathbf{N} + \mathbf{P} & \mathbf{C}^\top \\ \mathbf{C} & \mathbf{0} \end{pmatrix} \approx \begin{pmatrix} \mathbf{D} & \mathbf{C}^\top \\ \mathbf{C} & \mathbf{0} \end{pmatrix} \quad (3.35)$$

This approximate form is easy to invert (assuming every frequency component of every channel has non-zero noise and every constraint is satisfiable, which is true in practice), and can be used to precondition our problem for better numerical behavior.

We can further factor this approximate form of the matrix:

$$\begin{aligned} \begin{pmatrix} \mathbf{D} & \mathbf{C}^\top \\ \mathbf{C} & \mathbf{0} \end{pmatrix} &= \begin{pmatrix} \mathbf{D}^{1/2} & \mathbf{0} \\ \mathbf{CD}^{-1/2} & \mathbf{H} \end{pmatrix} \begin{pmatrix} \mathbf{D}^{1/2} & \mathbf{D}^{-1/2}\mathbf{C}^\top \\ \mathbf{0} & -\mathbf{H}^\top \end{pmatrix} \\ &= \begin{pmatrix} \mathbf{D}^{1/2} & \mathbf{0} \\ \mathbf{0} & \mathbf{I} \end{pmatrix} \begin{pmatrix} \mathbf{I} & \mathbf{0} \\ \mathbf{CD}^{-1/2} & \mathbf{H} \end{pmatrix} \begin{pmatrix} \mathbf{I} & \mathbf{D}^{-1/2}\mathbf{C}^\top \\ \mathbf{0} & -\mathbf{H}^\top \end{pmatrix} \begin{pmatrix} \mathbf{D}^{1/2} & \mathbf{0} \\ \mathbf{0} & \mathbf{I} \end{pmatrix} \end{aligned} \quad (3.36)$$

where \mathbf{H} is a lower-diagonal square matrix defined uniquely as the Cholesky decomposition $\mathbf{HH}^\top = \mathbf{CD}^{-1}\mathbf{C}^\top$. (The solution is guaranteed to be real because \mathbf{D} is positive-semidefinite in all cases, and positive-definite in practice – it consists of noise variance terms, which are strictly positive in practice.) Note that $\mathbf{CD}^{-1}\mathbf{C}^\top$ has dimensions equal to the number of signals in an event, which in practice will be small enough that we can compute its Cholesky decomposition \mathbf{HH}^\top directly.

The two diagonal factors are easily inverted; we further define

$$\mathbf{K}_1 = \begin{pmatrix} \mathbf{I} & \mathbf{0} \\ \mathbf{C}\mathbf{D}^{-1/2} & \mathbf{H} \end{pmatrix} \quad \mathbf{K}_1^{-1} = \begin{pmatrix} \mathbf{I} & \mathbf{0} \\ -\mathbf{H}^{-1}\mathbf{C}\mathbf{D}^{-1/2} & \mathbf{H}^{-1} \end{pmatrix} \quad (3.37)$$

$$\mathbf{K}_2 = \begin{pmatrix} \mathbf{I} & \mathbf{D}^{-1/2}\mathbf{C}^\top \\ \mathbf{0} & -\mathbf{H}^\top \end{pmatrix} \quad \mathbf{K}_2^{-1} = \begin{pmatrix} \mathbf{I} & \mathbf{D}^{-1/2}\mathbf{C}^\top\mathbf{H}^{-\top} \\ \mathbf{0} & -\mathbf{H}^{-\top} \end{pmatrix}, \quad (3.38)$$

where $\mathbf{M}^{-\top}$ represents the inverse of the transpose of \mathbf{M} . We then follow the standard proscription for preconditioning a linear system by replacing our original matrix equation with the new form:

$$\mathbf{K}_1^{-1} \begin{pmatrix} \mathbf{D}^{-1/2} & \mathbf{0} \\ \mathbf{0} & \mathbf{I} \end{pmatrix} \begin{pmatrix} \mathbf{N} + \mathbf{P} & \mathbf{C}^\top \\ \mathbf{C} & \mathbf{0} \end{pmatrix} \begin{pmatrix} \mathbf{D}^{-1/2} & \mathbf{0} \\ \mathbf{0} & \mathbf{I} \end{pmatrix} \mathbf{K}_2^{-1} \tilde{\mathbf{A}} = \mathbf{K}_1^{-1} \begin{pmatrix} \mathbf{D}^{-1/2} & \mathbf{0} \\ \mathbf{0} & \mathbf{I} \end{pmatrix} \begin{pmatrix} \mathbf{0} \\ \mathbf{I} \end{pmatrix}$$

$$\tilde{\mathbf{A}} = \mathbf{K}_2 \begin{pmatrix} \mathbf{D}^{1/2} & \mathbf{0} \\ \mathbf{0} & \mathbf{I} \end{pmatrix} \mathbf{A}$$

which reduces to

$$\mathbf{K}_1^{-1} \left[\begin{pmatrix} \mathbf{D}^{-1/2}\mathbf{N}\mathbf{D}^{-1/2} & \mathbf{0} \\ \mathbf{0} & \mathbf{0} \end{pmatrix} + \begin{pmatrix} \mathbf{D}^{-1/2}\mathbf{P}\mathbf{D}^{-1/2} & \mathbf{D}^{-1/2}\mathbf{C}^\top \\ \mathbf{C}\mathbf{D}^{-1/2} & \mathbf{0} \end{pmatrix} \right] \mathbf{K}_2^{-1} \tilde{\mathbf{A}} = \begin{pmatrix} \mathbf{0} \\ \mathbf{H}^{-1} \end{pmatrix} \quad (3.39)$$

$$\mathbf{A} = \begin{pmatrix} \mathbf{D}^{-1/2} & \mathbf{0} \\ \mathbf{0} & \mathbf{I} \end{pmatrix} \mathbf{K}_2^{-1} \tilde{\mathbf{A}} \quad (3.40)$$

This preconditioned set of equations is numerically quite stable. It is also possible to provide an excellent initial guess $\tilde{\mathbf{A}}_0$ by taking the approximate form of the matrix to be exact, yielding

$$\tilde{\mathbf{A}}_0 = \begin{pmatrix} \mathbf{0} \\ \mathbf{H}^{-1} \end{pmatrix}$$

Based on these various advantages, it is this system which we attempt to solve rather than the original form. Below we define matrices \mathbf{M} and \mathbf{B} for convenience, and summarize the system to be solved:

$$\mathbf{M} = \mathbf{K}_1^{-1} \left[\begin{pmatrix} \mathbf{D}^{-1/2} \mathbf{N} \mathbf{D}^{-1/2} & \mathbf{0} \\ \mathbf{0} & \mathbf{0} \end{pmatrix} + \begin{pmatrix} \mathbf{D}^{-1/2} \mathbf{P} \mathbf{D}^{-1/2} & \mathbf{D}^{-1/2} \mathbf{C}^\top \\ \mathbf{C} \mathbf{D}^{-1/2} & \mathbf{0} \end{pmatrix} \right] \mathbf{K}_2^{-1} \quad (3.41)$$

$$\mathbf{B} = \tilde{\mathbf{A}}_0 = \begin{pmatrix} \mathbf{0} \\ \mathbf{H}^{-1} \end{pmatrix} \quad (3.42)$$

$$\mathbf{M}\tilde{\mathbf{A}} = \mathbf{B} \quad (3.43)$$

$$\mathbf{A} = \begin{pmatrix} \mathbf{D}^{-1/2} & \mathbf{0} \\ \mathbf{0} & \mathbf{I} \end{pmatrix} \mathbf{K}_2^{-1} \tilde{\mathbf{A}} \quad (3.44)$$

3.6 Solver

The matrix $\tilde{\mathbf{A}}$ for which we attempt to solve will have as many columns as there are signals we wish to denoise within an event; often, this will only be one, and $\tilde{\mathbf{A}}$ will simply be a column vector. However, there certainly are many events with multiple scintillation signals; we will also later discuss extended applications of denoising where we may treat events as having additional signals. In these cases the number of columns may be larger. In such cases it would be possible to solve for each column of $\tilde{\mathbf{A}}$ independently, but more efficient to solve the entire system simultaneously. In this way, information obtained from multiplying the matrix by one column may be exploited to solve the other columns as well, effectively multiplying the benefit from each matrix-multiplication by the number of columns of $\tilde{\mathbf{A}}$.

Matrix-solving algorithms which handle multiple vectors simultaneously are commonly referred to as block algorithms. We will use the Block-BiCGSTAB algorithm [55], an iterative method based on the popular stabilized biconjugate-gradient (BiCGSTAB) method. BiCGSTAB and Block-BiCGSTAB are notable for being able to deal with arbitrary matrices rather than requiring that the matrix be positive-definite (which our matrix is not). The algorithm is reproduced in the form used by our code as Algorithm 1. This algorithm only requires that we are able to left-multiply vectors and matrices by \mathbf{M} quickly, which makes it possible to exploit the sparsity of \mathbf{M} .

Since each column of $\tilde{\mathbf{A}}$ corresponds to one signal we are refitting, the norm of the corresponding column of \mathbf{R} tells us how well we have identified the optimal magnitude estimator for that signal; thus, to test for termination we should evaluate the norm of each column of \mathbf{R} , and while any of those norms are above some threshold, the solver must be permitted to continue. Because our resolution is only on the order of 1%, solutions generally need not be very accurate; in practice, we establish reasonable thresholds by plotting resolution against threshold for a small subset of data, and observing when the resolution stops improving.

3.7 Implementation

Although the previous section described the algorithm used for solving these matrix equations, in practice the processing time required is still significant; combined with the very large number of events which we hope to denoise (hundreds of millions), we

Algorithm 1 Block-BiCGSTAB Algorithm

```
1:  $\tilde{\mathbf{A}} \leftarrow \tilde{\mathbf{A}}_0$ 
2:  $\mathbf{R} \leftarrow \mathbf{B} - \mathbf{M}\tilde{\mathbf{A}}$ 
3:  $\mathbf{S} \leftarrow \mathbf{R}$ 
4:  $\tilde{\mathbf{R}}_0 \leftarrow \mathbf{R}$ 
5: loop
6:    $\mathbf{V} \leftarrow \mathbf{M}\mathbf{S}$ 
7:   Solve  $(\tilde{\mathbf{R}}_0^\top \mathbf{V})\alpha = (\tilde{\mathbf{R}}_0^\top \mathbf{R})$  for  $\alpha$ .
8:    $\mathbf{R} \leftarrow \mathbf{R} - \mathbf{V}\alpha$ 
9:    $\mathbf{T} \leftarrow \mathbf{M}\mathbf{R}$ 
10:   $\omega \leftarrow \langle \mathbf{T}, \mathbf{S} \rangle_F / \langle \mathbf{T}, \mathbf{T} \rangle_F$ , where  $\langle \cdot, \cdot \rangle_F$  is the Frobenius matrix norm.
11:   $\tilde{\mathbf{A}} \leftarrow \tilde{\mathbf{A}} + \mathbf{S}\alpha + \omega\mathbf{R}$ 
12:   $\mathbf{R} \leftarrow \mathbf{R} - \omega\mathbf{T}$ 
13:   $\mathbf{R}$  currently equals  $\mathbf{B} - \mathbf{M}\tilde{\mathbf{A}}$ 
14:  if all columns of  $\mathbf{R}$  have sufficiently small magnitudes then
15:    return  $\tilde{\mathbf{A}}$ 
16:  end if
17:  Solve  $(\tilde{\mathbf{R}}_0^\top \mathbf{V})\beta = -(\tilde{\mathbf{R}}_0^\top \mathbf{T})$  for  $\beta$ .
18:   $\mathbf{S} \leftarrow \mathbf{R} + (\mathbf{S} - \omega\mathbf{V})\beta$ 
19: end loop
```

still must seek out any possible speed-ups. There are certain implementation tricks which can be applied with significant impact. These are described here.

The majority of non-zero matrix entries comes from the electronic noise matrix \mathbf{N} , making it the computational bottleneck of the algorithm. \mathbf{N} is block-diagonal, as seen in equation 3.29; if we assume roughly 70 APD channels, then the last block of \mathbf{N} will have 70^2 non-zero entries and all other blocks will have $4 \cdot 70^2$ non-zero entries. With waveforms having 2048 samples, and ignoring the baseline component, the problem of multiplying a vector by the electronic noise terms thus consists of 1024 matrix-matrix multiplications, with each left matrix containing roughly 20,000 non-zero terms and each right matrix consisting of $O(1)$ columns and roughly 150 rows. (The number of columns in the right matrix is equal to the number of signals, which may be sometimes 3 – 5 or more; however, it is always much smaller than 150, and describing it as $O(1)$ captures this fact.)

The key points here which create an opportunity for optimization are that:

- The electronic noise terms generally do not change event-by-event. They are treated as constant across many runs.
- It is possible to multiply two $N \times N$ matrices together much faster than it is possible to perform N multiplications of an $N \times N$ matrix with $N N \times 1$ matrices. This can be achieved with a combination of algorithms faster than naive $O(N^3)$ speed and exploitation of low-level computer hardware features such as the CPU cache. [56, 57]

What we wish to do, then, is reorganize the solver algorithm so that whenever

multiplication by the electronic noise matrix is required, rather than performing that multiplication on a “skinny” $150 \times O(1)$ matrix, we pack together many such “skinny” matrices into a single matrix with many columns. Multiplication can then be performed in bulk; and individual columns from the result can be extracted and used as before.

Additionally, it is important that matrix multiplication be made as fast as possible. It has long been known that matrix multiplication provides significant opportunities for low-level optimizations. For example, most of the time taken by naive matrix multiplication is spent fetching and writing data to and from RAM. Significant speedups can be achieved by minimizing the number of CPU cache misses, which can be accomplished by operating on matrices in blocks with size chosen so they fit entirely in the cache. Multiplication instructions can also often be packed into vector instructions such as SSE or AVX. For extremely large matrices, there are even algorithms which require fewer than $O(N^3)$ multiplications, and these can sometimes be beneficial. [57]

Optimization of matrix-matrix multiplication is a large field, but fortunately there are a number of well-tuned software libraries implementing matrix multiplication well-tuned to specific machines. These libraries generally provide the standard Basic Linear Algebra Subroutines (BLAS) interface, making them interchangeable with ease. In this instance, Intel’s MKL library has been used; benefits to this implementation are its availability on scientific computing platforms and its ability to adapt to heterogeneous compute clusters by detecting the architecture of the machine on which it is run. [58]

Finally, implementation at NERSC has the interesting feature that NERSC’s computing systems are designed for multi-core processing. The Hopper and Edison computing systems at NERSC allocate whole nodes, each of which contains 24 cores. Although it is possible to simply run 24 independent processes on each node, memory on NERSC machines is highly constrained; memory use can be reduced by sharing certain large data structures across multiple cores on a node. Additionally, as more events are packed together for electronic-noise multiplication, greater savings can be realized; so it is better to handle many events in coordination. To this purpose, a multi-threaded version of the program has been developed to exploit portions of the code which are conveniently distributed. Because NERSC nodes have a Non-Uniform Memory Access (NUMA) architecture, processes are constrained to only run on cores with a similar memory access pattern; on Hopper this results in four 6-threaded processes per node, while on Edison this results in two 12-threaded processes per node.

As a result, and because the bulk of our computational time is spent multiplying by \mathbf{N} , we pursue the following strategies to improve code performance:

1. One denoising process will be run on each NUMA node of a NERSC machine. Processes should be run in “strict memory mode,” where a process only has access to memory resources on its own NUMA node.
2. Within a process, algorithm 1 should be performed in parallel on all available cores to maximize CPU utilization.
3. When a thread encounters the need for a matrix multiplication in lines 2, 6,

or 9, the thread should not multiply by \mathbf{N} . Instead, it should push the left hand side into new columns of a matrix \mathbf{RHS} of “thin” matrices needing to be multiplied by \mathbf{N} .

4. When enough columns have accumulated in \mathbf{RHS} , collect the running threads; these threads should each perform some fraction of the matrix multiplications between blocks of \mathbf{N} and the corresponding rows of \mathbf{RHS} . When this is complete, the threads should resume their processing of algorithm 1 in parallel on the available pool of events.
5. Every matrix multiplication should be performed by a direct call to the Intel MKL library. To facilitate this process, \mathbf{N} should be stored in a format that ensures its blocks are accessed in a contiguous segment of memory. Furthermore, because there is ample opportunity for higher-level parallelization, at no time should a multithreaded BLAS operation be invoked; this reduces computational overhead of parallelization.

These represent the most significant set of computational optimizations. However, there are also smaller optimizations which can still produce non-negligible speedups. The naive Block-BiCGSTAB algorithm (in the case of only one signal in an event) requires two matrix-vector multiplications, but it also requires a number of vector-vector operations, and the cumulative cost of these vector-vector operations can become non-negligible. One obvious shortcut is to reuse our computation of $\tilde{\mathbf{R}}_0^\top \mathbf{V}$ from line 7 of Algorithm 1 to save work in line 17.

Another speedup for our vector-vector operations consists of combining mul-

tiple operations into one step. We see on line 7 that both $\tilde{\mathbf{R}}_0^\top \mathbf{V}$ and $\tilde{\mathbf{R}}_0^\top \mathbf{R}$ are computed. As described earlier in the context of multiplication of vectors by electronic noise, it is possible to take advantage of caching and speed up vector operations by packing multiple vectors together into a more square-shaped matrix. In this case, rather than computing these two products separately, we can pack \mathbf{V} and \mathbf{R} together and compute

$$\tilde{\mathbf{R}}_0^\top \begin{pmatrix} V & R \end{pmatrix}$$

as one step. The rest of the algorithm will not be affected by the fact that these two matrices are stored contiguously in memory.

3.8 Denoising in Practice

The preceding description of denoising has been intended to convey our fullest current understanding of denoising as it should be performed. However, due to the computational intensity of this algorithm it is not feasible to conduct routine data processing of the full EXO-200 dataset whenever updates to the code base are implemented. As a result, the most recent denoised data available from EXO-200 demonstrates certain deviations from the description above. It is known, and has been demonstrated, that correcting some of these flaws can lead to further improvements in resolution, but no physics analysis will be performed with those improvements until the computational cost of denoising is again deemed worthwhile.

In this section we outline the places where the denoising used for the current physics analysis differs from the description above. Differences in implementation

also exist, but will not be described here. The differences of denoising are:

- The signal variance coming from sources internal to the APDs was not fully understood by this author when denoising was first implemented, and as a result the signal variance is significantly underestimated. Specifically, in place of equations 3.9 and 3.11 we take

$$\left\langle P_{ia}^{(3)} P_{jb}^{(3)} \right\rangle = (1.9)^2 \cdot G_i^P(t_a) G_j^P(t_b) \left\langle P_{ia}^{(1)} P_{jb}^{(1)} \right\rangle.$$

- We have described with equation 3.15 that the electronic gain is treated as having a constant value of $1.1 \cdot 10^{-3}$ ADC counts per electron emitted from the APDs. The wires use a similar set of electronics; however, their gain is nominally set to a different value of roughly $6.3 \cdot 10^{-4}$ ADC counts per electron collected on the wires, and this author confused the two numbers. As a result, $G_i^E(t)$ was underestimated by almost a factor of two; the effect of this is to overestimate by almost a factor of two the number of photons being deposited on APDs, which again causes us to underestimate the signal variance introduced within the APDs.

The effect of both of these issues is, loosely speaking, to fool denoising into believing its photon statistics are greater than they truly are; this, in turn, leads it to prefer a higher concentration of signal (more weight on fewer channels) than is ideal. Thus, the resolution is negatively impacted by these mistakes; the impact has been measured in subsets of the EXO dataset and this negative impact is apparent.

However, neither of these mistakes have any impact on the correctness of the constraints. As a result, the denoised energy measurements should still be unbiased, even if they have worse variance than necessary. Results from the use of this data will be described in chapter 6.

3.9 Future Plans

As outlined here, denoising is capable of producing optimal estimates of the total energy emitted in scintillation by a particular event; however, it should be noted that this algorithm can be applied to a more general range of problems in the EXO-200 detector with only minor modifications.

3.9.1 Anticorrelated Cluster Energies

One important generalization is in our definition of “signals.” In the body of this chapter, we have worked on the assumption that a signal consists of a simultaneous set of energy deposits in the bulk of the detector, possibly at multiple locations. We do this because it must be possible for denoising to break degeneracies between signals – by specifying that two different signals must have occurred at different times, we give the algorithm a means to discriminate between light coming from the two different signals and assign energy properly to each of them.

Historically, time was the only useful variable for this sort of discrimination; because multiple APD channels were added together and all APD channels were treated as identical in this sum, a significant amount of information was discarded

and there were no remaining parameters to use for signal separation except for the signal time.

However, this denoising algorithm makes use of additional information: the relative magnitudes of each APD gang. By depending on a highly detailed lightmap, we have incorporated information about which channels should see light most from energy deposits at different positions. As a result, if we permit two “signals” which are simultaneous in time, it should be possible to separate their energy content by comparing their positions to the set of channels which see more light. This would allow us to produce anti-correlated energy measurements of individual clusters, which should give a significant improvement in the energy resolution achievable for clusters within an event.

In principle, this is entirely feasible – in the extreme case, when two clusters are at opposite ends of the detector we can expect them to produce light on an entirely different set of channels, and it should be quite easy to separate light produced by each. However, this extension of our algorithm does present some practical challenges.

In EXO’s reconstruction, light signals which are found close together in time are aggressively merged together, ensuring that denoising will never encounter light signals which are very close in time; this assures us that two signals separated in time will be well-separated, and there will not be a near-degeneracy which could render the solver algorithm unstable.

However, charge clusters are merged much less aggressively, and some bugs exist which have minimal effect on the main analysis but permit the existence of

clusters very near to each other. For denoising to separate simultaneous light signals solely based on their relative position, they must be separated far enough that their respective light yields on nearby APD channels are significantly different, which is not at all guaranteed by reconstruction. As a result, denoising can only fit simultaneous signals separately if it performs a re-clustering process in which clusters occurring near each other are artificially merged together for the purpose of denoising. The threshold for merging clusters together would require further study, and might be different in each of the three coordinate directions.

Such an analysis would not have a significant impact on single-site data, so it would have minimal impact on our primary goal of searching for double-beta decay. However, it could have a significant impact on a search for excited-state two-neutrino double-beta decay by improving the resolution of gamma lines associated with Barium de-excitation. Barabash states in [59] that the dominant mode of excited-state $2\nu\beta\beta$ decay will be to the 0_1^+ state, which in ^{136}Ba would lead to the emission of a 760 keV and 819 keV gamma in coincidence; if denoising could be accomplished on individual clusters, the sensitivity to these gamma lines could be significantly enhanced.

There are also potential benefits to our understanding of the detector itself. Currently the only mono-energetic beta calibration available for EXO is the double-escape peak, formed when a gamma particle enters the detector, pair-produces an electron and positron, and the positron interacts with an electron and emits gammas which travel sufficiently far from the initial interaction site so that the initial electron interactions and gamma interactions can be clearly separated. Currently we have

the ability to separate charge yield from gammas and the initial electron in some of these events, allowing us to understand the different charge yields from gammas and betas. However, we have no similar capabilities for light yield because the gamma and beta interactions are treated as just one “signal.” If we could separate the light yield from these spatially separated clusters, we could use these events to understand both the light and charge yield for different types of interactions.

Another type of detector study which might benefit from anticorrelated cluster energies is the Compton telescope. This is a technique that combines our knowledge of cluster energies and scattering angles, along with the Compton scattering formula [60], which allows us to produce estimates of the origin of the incident gamma. Such a technique permits us to study the sources of our backgrounds, informing future attempts to reduce them by indicating which materials had the most significant negative effect. The accuracy by which we place the origin of the incident gammas is strongly related to the accuracy of our measurements of the energies of the individual clusters, so it is expected that improving the accuracy of our cluster energies would have a positive impact on our ability to locate the backgrounds of our experiment.

The last benefit to this approach is more technical: evaluating the lightmap for a multi-site event requires an energy-weighted combination of the values of the lightmap at individual cluster locations. This process is complicated and error-prone, and can be avoided entirely when we treat each signal instead as having a single well-defined position.

3.9.2 Wire Denoising

The current EXO-200 resolution is limited by the scintillation resolution of the APDs. As a result, little benefit is anticipated from denoising the wires. However, it is possible that a future detector could reduce the scintillation noise to a point where resolution of the wires is non-negligible; alternatively, a future detector could have noise which is correlated between wires and APDs, making it possible to use noise information from the wires to improve our scintillation resolution even though no direct benefit is expected to the wire resolution itself.

In any case, it is possible to apply equations 3.23 to a system with a combination of wires and APDs without significant adjustment. The template functions $Y[t]$ will of course be significantly different, and must include a time offset to account for the different time of arrival of the electrons and photons. The “lightmap” of charge will be far less diffuse than for APDs because charge from any location generally drifts directly to only a small number of wires along externally imposed field lines. And finally, because electron statistics should be negligible and signal amplification should not be a noisy process, for wire channels we would modify equation 3.22 to state that $q(i_{\text{wire}}, b) = 0$. In this sense, denoising of wires consists of minimizing the variance in the energy estimator due to electronic noise, and using the wires to improve our denoising of APDs consists of using information about the wires to reduce variance due to electronic noise without expecting any correlations between APD and wire signals, all while ensuring that the energy estimates are unbiased by retaining the same constraints.

Chapter 4: Noise Measurements

We have described in chapter 3 the principles and algorithm behind denoising. Among the points made is that a detailed noise model is required to perform denoising. Equation 3.5 specifies that the correlations in electronic noise will be taken as inputs to denoising; in this chapter we will describe the measurement of the noise correlations. Section 4.1 will specify the desired measurement; section 4.2 will identify the time-dependent behavior of noise; and section 4.3 will describe the algorithm employed to measure noise from data. We conclude in section 4.4 with some possible future work to improve the quality of the noise measurements or use them in other aspects of the EXO-200 analysis.

4.1 Mathematical Framework for Noise Correlations

A waveform on channel i with no pulse on it consists entirely of a noise function $N_i[\tau]$. The noise is a random function: its value at each time τ is a random variable. Our goal, then, is to describe the joint probability distribution of those random

variables. It has also been observed that noise on different channels is correlated, so our joint probability distribution should describe not only the noise for all time samples τ on a particular channel i , but also the relation between noise on any distinct pair of channels i and j .

We can guarantee that the noise is stationary because the waveforms are all subject to shaping which removes low-frequency noise components, as described in section 2.5. It is conventional to study stationary noise in Fourier space. This can often lead to sharper features because noise often originates from environmental factors which demonstrate periodic behavior: in EXO-200, example of possible sources of periodic waveform noise include acoustic noise from the cleanroom, mechanical vibrations of the various wires under tension in the TPC, or switching noise from the digital power supplies. It also can lead to a simpler characterization of noise correlations: in a steady-state environment it is impossible for noise at two different frequencies to be correlated because the L_2 inner product of two sinusoidal functions with different frequencies is always zero.

We will write the discrete Fourier transform of $N_i[\tau]$ as $\tilde{N}_i[f]$, consistent with the notation described in section 3.1. Although the specific choice of convention will not matter for any of the analysis in this work, for completeness we specify explicitly the definition of the discrete Fourier transform as

$$\tilde{N}_i[f] = \sum_{\tau=0}^{T-1} N_i[\tau] e^{-2\pi\tau f \sqrt{-1}/T}, \quad (4.1)$$

where T is the (unitless) number of samples in the time domain waveform. The index f takes integer values from 0 to $\lfloor \frac{T}{2} \rfloor$, where $\lfloor \rfloor$ indicates that rounding is

performed downward. This set of conventions matches the conventions of the real-to-complex discrete Fourier transform implemented by the popular FFTW library, available on all computational platforms we have attempted to use. [61]

Our sampling frequency of 1 MHz means that we can associate $\tilde{N}_i[f]$ with noise at a frequency of f/T MHz (where we again recall that T and f are unitless). The accuracy of this association is dependent on the accuracy of the nominal 1 MHz sampling. This is controlled by a nominal 80 MHz oscillator in the master TEM unit; preliminary investigations indicate that this frequency changes over time, and may deviate from a true 80 MHz period by as much as ten parts per million. [51, 62] Since we apply low-pass filters with a combined effective cutoff frequency around 167 kHz, as described in section 2.5, this is expected to have a negligible effect on our noise measurements.

The first moments of the four

We have seen from equation 3.23 that denoising requires knowledge of the following expectation values as input:

$$\left\langle \tilde{N}_i^R[f] \tilde{N}_j^R[f] \right\rangle \quad (4.2)$$

What are we computing with the noise correlations. Symmetries; why the results aren't quite phase-symmetric for finite traces.

4.2 Time Windows of Constant Noise

Noise windows used. Plots to support this.

4.3 Algorithm for Measuring Noise

General algorithm to create noise matrices. Selection cuts on events. Data format.
(Yes, this is probably useful in the category of unifying notation.) U-wire noise
collected as well, to support occasional studies.

4.4 Future Directions with Noise Measurement

stripping the glitch from noise traces. using noise in monte carlo? Studying the
smoothness of the noise functions vs f (for truncated waveforms). Check noise
temperature dependence, other rapidly-varying environmental factors. Resolution
time-dependence can be used to check time windows; other approaches? (KZ tests
for consistency with flat.)

Chapter 5: The Lightmap

The EXO detector was designed with roughly 450 APDs ganged into 74 data channels of six to seven APDs each. Three of the APD ganged channels were disabled due to noisy components before physics data collection began; a fourth channel was disabled in February 2012 due to increasing noise in its components. All of the APDs were set into the two endcaps of the cylindrical EXO detector. To improve light collection, teflon sheets cover the sides of the detector and reflect light back into the liquid xenon rather than allowing it to be absorbed by the vessel walls.

The different positions of the APDs means that given the same amount of energy deposited into the detector, channels whose APDs are nearest to the deposited energy may show significantly larger signals than channels with APDs far from the deposit. As a result, it is critical to map out the response of the APDs as a function of deposit position \vec{x} .

Furthermore, the APDs and APD electronics will show time-dependent changes: gain will drift in each APD at independent rates, and stepwise changes to the APD signals comes from disabling of channels and changes to the electronics which have been implemented multiple times during the course of the experiment. This means

that in addition to mapping the response of the APDs as a function of deposit position \vec{x} , we must also map it as a function of deposit time t .

Early attempts to generate this mapping focused on periodic campaigns to collect large amounts of known-energy data and characterize the APD response at a moment in time. These campaigns would generally consist of days of source data. The strong Thorium-228 source would be used, and an expert would be on-site to position the source in a wide range of locations, to ensure that a single campaign was independently sufficient to characterize the APD response. The 2615-keV single-site gamma line of the Thallium-208 daughter product of Thorium-228 was isolated in offline analysis, and signals from these events were used to measure the signal magnitude from a known-energy single-position deposit in the detector.

Even with such a significant quantity of source data, statistics were found to be insufficient. Some regions of the detector were difficult to illuminate, and signals on individual channels were small. To simplify the problem, signals on each endcap were summed together (without gain corrections) so that the 70 or 71 active APD channels could be treated offline as two large-magnitude APD channels instead. This increased the size of the signals; it also made the spatial dependence of the response smoother, so that a sparser distribution of data could still be sufficient to characterize the response. This permitted the creation of an APD-plane lightmap which allowed EXO to produce its first position-dependent corrections to scintillation energy. [63]

Although the APD-plane lightmap produced significant improvements in the energy resolution achieved by the EXO detector, inevitably it was only an incomplete

characterization of the APD response. Indeed, because for $\beta\beta0\nu$ studies we place our fiducial cut as close to the edges of the detector as possible, in certain regions of the detector our scintillation signal might be highly concentrated on one or a small number of channels. Summing together multiple channels is, in this sense, a lossy form of compression of the data, and it is tempting to see whether we can extract better physics if it is avoided. The denoising algorithm described in chapter 3 describes one such analysis which can exploit knowledge of the behavior of individual APD channels; others might include reducing our scintillation thresholds by allowing us to search for signals in subsets of the APDs rather than only in sums across entire endcaps. Thus, characterizing the APD yield on individual APD-gang channels is not in itself an important component of our analysis, but may be expected to provide a critical tool for more advanced scintillation analysis.

5.1 Four-Dimensional Lightmap

As described above, in constructing an individual-APD lightmap we face two conflicting needs: we must use as much data as possible to handle the faster spatial dependence and smaller signals expected, but if too much data is included then we run the risk of combining data taken when an APD or the electronics had a different gain. If we truly wish to use all available data, then we will need to simultaneously understand the full time-dependence of the gain. In other words, rather than forming a small number of independently-measured three-dimensional lightmaps, we will need to measure a four-dimensional lightmap $L(\vec{x}, t)$. Since we will use Thorium-228

source data to generate the lightmap, we require that our lightmap should predict the magnitude of the signals on each APD gang induced by a single-site deposit of energy 2615 keV; figure 3.2 shows our definition of a unit-magnitude signal, which is the same as was used in chapter 3.

This may at first seem infeasible. After all, adding an extra time dimension to the arguments of the lightmap is equivalent to generating a new lightmap for every time bin, which is exactly the situation we wished to avoid. But we can make a key simplifying assumption that the lightmap is separable. In a physical sense, we can assume that:

1. From a given position \vec{x} photons deposit on each APD channel at a constant rate.
2. Each APD channel in turn magnifies and shapes its signal with a gain which may vary in time, but does not depend on the point of origin of the photons.

So, we demand that the lightmap have the much simpler form

$$L(\vec{x}, t) = R(\vec{x})S(t) \quad (5.1)$$

Is this simplification fully motivated by the detector? Although it is a reasonable approximation, there are details which it omits. The first point is fairly accurate: we must trust that the electric field and the reflectivity of detector surfaces are constant in time, but these conditions are assumed to hold within EXO-200.

However, each channel can draw its signal from multiple APDs, each of which has an independent time-varying gain. Photons from a deposit may preferentially

sample the gain from the closest APD within a channel, so deposits in different locations may track more closely the gain of the closest APD within a channel, and the second point may not be accurate. Studying the impact of this effect should be a topic for future study, particularly to understand to what degree it limits the effectiveness of a lightmap; it may be relevant to nEXO planning to understand how ganging together APDs reduces the quality of the approximation of equation 5.1. The current analysis will treat it as a small effect.

So, treating equation 5.1 as valid, one simple general scheme to find R and S iteratively is described in algorithm 2. Step 1 of that algorithm is to select 2615-keV single-site events; it is understood that compton-scattered events will inevitably leak into our selection window, but we use the best available energy measurements to reduce that likelihood and trust that as analysis improvements continue to sharpen our resolution, the number of compton-scattered events leaking through becomes smaller and the quality of the lightmap will continue to improve. The rest of the algorithm then describes how we can efficiently converge on estimates of $R(\vec{x})$ and $S(t)$ through an iterative approach. We do not prove that the algorithm is guaranteed to converge; however, in practice $S(t)$ is close to constant, resulting in fairly rapid convergence.

5.2 Algorithm Details

The previous section outlines a general algorithm for computing a four-dimensional lightmap from source data. In this section we will specify the implementation choices

Algorithm 2 Generating a Lightmap

- 1: Tabulate, using the best energy measurement available, a list of single-site 2615-keV events from Thorium-228 source data.
 - 2: Set $S(t) = 1$ for all APD channels.
 - 3: **repeat**
 - 4: For each APD channel, estimate $R(\vec{x}) = L(\vec{x}, t)/S(t)$ from the set of events tabulated in line 1.
 - 5: For each APD channel, estimate $S(t) = L(\vec{x}, t)/R(\vec{x})$ from the set of events tabulated in line 1.
 - 6: **until** convergence is reached.
-

which are made in the code currently being used. In attempt to encourage future experimentation, alternative options will also be listed in some detail, along with some motivations for these alternatives. Time has not permitted testing of all of these options, but it is hoped that they will be explored in the future.

5.2.1 Event Selection

The single-site Thorium-228 spectrum is well-peaked at 2615 keV, making it an excellent monoenergetic calibration line. Our challenge is to select truly 2615-keV events as efficiently as possible, while simultaneously avoiding near-2615-keV events which may leak into the dataset.

This is an inherently iterative process. The first lightmap had to be constructed from an ionization-only spectrum because no useful position-corrected scintillation measurement existed; the resolution of the ionization-only spectrum was

quite poor, roughly 3.5% (sigma) of the energy, as described in Steve Herrin's thesis, and severe compromises had to be made to keep the Compton-shoulder leakage down to acceptable levels. That work required events to have ionization between 0.33σ and 3σ to the right of the ionization peak. [63]

Such a strongly asymmetric cut was chosen to avoid leakage from compton shoulder events, which it did successfully. However, because of anticorrelation between scintillation and ionization, choosing events whose ionization had oscillated high means this cut was also preferring events whose scintillation had oscillated low, introducing a bias in the lightmap magnitude. Additionally, the cut permits less than 37% of desired events to be accepted, which is a substantial loss of efficiency that has a significant impact in certain low-statistics regions of the detector.

The current work has had the benefit of an existing position-corrected scintillation measurement, leading to a rotated energy spectrum with resolution of roughly 1.8%. As a result, it is possible to accept a wider cut (in sigmas) while still keeping Compton shoulder leakage small. We currently accept all events within 2σ of the peak, with better than 95% acceptance and only small leakage. An additional benefit is that this improved resolution allows us to use a symmetric acceptance region, avoiding the implicit bias introduced from the earlier asymmetric cut window.

Preliminary investigations have been conducted to see what impact is observed from using the denoised scintillation measurements which are the subject of this work. Presently the improvement in resolution (**to roughly 1.4% UPDATE WITH REAL NUMBER when the paper is finalized**) has not demonstrated any significant improvement in the quality of the lightmap beyond what we could achieve with

1.8% resolution; however, this is a topic of continuing study which will certainly be revisited.

Beyond the cuts described above (single-site within an appropriate energy window), other basic cuts are applied to ensure only well-behaved scintillation signals are selected:

- Charge and light must individually lie within a reasonable range.
- The charge-to-light ratio must not identify an event as an alpha decay.
- The scintillation time must be well-separated from any other scintillation signals in same event frame.
- All charge signals which are assigned to this scintillation signal must be assigned unambiguously.
- All three position coordinates must be known. (No fiducial cut is placed, since that would restrict the volume where the lightmap is specified.)

Many of these cuts are probably no longer necessary – as the resolution has improved, the chances of contamination have decreased and we can be a bit less cautious about accepting events. It is worth remembering, though, that our main analysis only accepts events with a single scintillation signal, something which for us would carry too high a cost in lost statistics. (Strong Thorium runs produce a significant rate of events with multiple scintillation signals. These statistics are quite valuable, particularly because they are the primary source of statistics in some hard-to-reach

regions of the detector.) As a result, it is important to maintain some caution with cuts designed to handle those events more robustly.

5.2.2 Function Parametrization

Because we are attempting to empirically measure the functions $R(\vec{x})$ and $S(t)$ from a finite dataset, we need to specify some more limited form for them to take. All current approaches to describing $R(\vec{x})$ first bin the detector volume into three-dimensional voxels, and then define $R(\vec{x})$ to interpolate linearly between known values at the center of the voxels. The size of these voxels must be chosen with some care; if they are too small, then low per-voxel statistics will cause the statistical errors on the signal magnitude to dominate, whereas if the voxels are too large then the spatial variation of the lightmap will not be fully captured.

In the current lightmap, the detector is binned into 1cm^3 voxels; the detector is easily contained within a box with sides 40cm long, leading to 64,000 voxels (of which roughly 20% lie outside of the detector and will be empty). The choice of voxel size was made based on the size of an individual APD. The APDs are roughly 2.5cm in diameter, so very near the anode we would like for the size of a voxel to be much smaller than 2.5cm . When this is done, much of the detector has entirely sufficient statistics per voxel; however, there are some regions of the detector with fewer than ten hits per voxel, indicating that $R(\vec{x})$ may have quite significant statistical error in these regions.

It is possible to justify a choice of larger voxels. The APDs lie at $\pm 204\text{mm}$

from the cathode, which means that there is more than 2cm between our fiducial volume and the APDs. At this distance, the dependence of the lightmap on x and y is expected to be much slower than at the APD plane, indicating that perhaps 2cm binning in x and y may be sufficient. Additionally, z -dependence of the lightmap is expected to be fairly smooth throughout the detector; since we interpolate linearly between voxels, it may be possible to use a z -binning much coarser than 1cm . This may be a topic for future investigation.

It is also worth mentioning that less intuitive voxel geometries have been tried in the past. The older APD-plane lightmap [63] used a cylindrical-coordinate binning; binning in r was selected to make the bin volumes roughly constant along the r axis, binning in the angular coordinate was uniform, and binning in z was chosen to be coarser near the anodes and finer near the cathode to reflect faster variation there. In all cases the binning was coarser than with the current cubic voxels being used; our finer binning is made possible by the larger quantity of available statistics from using the full dataset, and is justified by the potential for the yield on a single APD gang to vary more rapidly than the yield averaged across an entire APD plane.

It is well-known [64] that when it is necessary to estimate a multivariate function from limited statistics, a choice of binning can have a significant impact on the result. It is preferable to use an unbinned technique such as kernel regression. In particular, our data density is highly non-uniform, and it should be possible to measure the lightmap which high fidelity in regions of high statistics, while smoothly transitioning to a coarser interpolation in regions of low statistics to minimize the impact of uncertainty from individual hits. State-of-the-art solutions to this problem

would rely on locally adaptive kernel regression; see [64] for a detailed explanation of the related issues in non-parametric multivariate regression. Attempting to use a locally adaptive kernel regression for $R(\vec{x})$ should be considered a highly appealing extension to the algorithm for generating a lightmap.

The parametrization of $S(t)$ presents a very different set of choices. Thorium data is taken in bursts, with the time between mostly filled by low-background runtime. When we choose to treat $S(t)$ as a smoothly varying function, it becomes critical to interpolate properly – after all, the low-background runtime is the critical part of the experiment. (If we only produce a lightmap accurate during source runtime, we will measure an energy resolution from source data which is not borne out in the low-background data, so we should in fact be able to give some guarantee that $S(t)$ is almost as accurate during the low-background runtime as during the source runtime.) Fortunately, it is generally true that the time variation of the APD response is quite slow; exceptions are generally due to changes in the electronics which should occur at well-specified times.

Currently each source run is treated as a burst of data taken at the midpoint of the run, and $S(t)$ is measured at that point only from the data of that run; then $S(t)$ is linearly interpolated between those points. In principle it is possible that between two source runs an electronics change may have been performed, which would mean that a better interpolation would be to assume $S(t)$ is flat except for a step at the time of the electronics change; in practice, though, EXO has generally taken a source run immediately before and after an electronics change, so no high-value data is taken during that interval and this detail can be ignored.

Another concern with this method is what should be done with short source runs. If a run is too short, then the measurement of $S(t)$ coming from that run may have significant errors. We currently mitigate this issue by entirely throwing out all data from runs with fewer than 100 usable events. We justify this approach by claiming that even though those events might in principle have contributed some useful information on $R(\vec{x})$, without a good measurement of the relevant $S(t)$ it is impossible to use that data.

It would be better if we made use of our knowledge that $S(t)$ changes slowly or at well-defined moments. In the future, it would be useful if instead we performed smoothed interpolations between electronics changes. This could be done in the same style as EXO’s lifetime corrections, using polynomial fits, where the degree of the polynomial could be determined by eye. A candidate set of time intervals when $S(t)$ might be treated as constant could be the same as the set of constant noise windows described in chapter 4. It would be possible to check whether this time binning is fine enough by looking at the Thorium scintillation peak position versus time in denoised data – if it appears to drift in time within a window where $S(t)$ is treated as constant, then it is likely that $S(t)$ needs to be binned more finely.

Alternatively, often there will be a long string of consecutive source runs which should be combined into one higher-statistics dataset. This process would need to be done essentially by hand, and has not been performed for the current analysis, but it could benefit the accuracy of the $S(t)$ function and also recover some statistics in cases where the individual runs might be too short for inclusion in the lightmap dataset.

The choice of binning or parametrization for $R(\vec{x})$ and $S(t)$ can have a profound impact on the accuracy of the lightmap, and the current analysis has only skimmed the surface in trying options. It is hoped that further work on the lightmap will include significant investigation in these topics.

5.2.3 Convergence and Error Estimation

Our treatment of the convergence of algorithm 2 and the resulting statistical errors in $L(\vec{x}, t)$ is extremely rudimentary. Broadly convergence is checked not by analysis of the lightmap itself, but by verifying that the energy resolution from denoising is not improved by further iterations through algorithm 2. Lightmap errors do not directly enter into the calculations of denoising (which treats the lightmap as perfectly known), so they are not estimated at all in the current analysis.

As a proxy for estimation of the statistical errors in the lightmap, we instead study the number of hits observed in each position voxel of the detector (see section 5.4), and presume that the most significant source of error comes from low-statistics regions of the detector. This information can motivate future data-taking campaigns to probe the light response in those regions of the detector and reduce these uncertainties. However, no explicit estimation of the lightmap uncertainty has been attempted.

One difficulty with estimating the errors in the lightmap function $L(\vec{x}, t)$ comes from the correlation between errors in $R(\vec{x})$ and $S(t)$. If one of those two components were known perfectly, then we could treat the fit uncertainties of each hit as

independent errors, and propagate those errors into an uncertainty for each voxel of $R(\vec{x})$ (if $S(t)$ is assumed to be perfectly known) or $S(t)$ (if $R(\vec{x})$ is assumed to be perfectly known). But in reality, all of the measurements of $R(\vec{x})$ are correlated with all of the measurements of $S(t)$, meaning that even the errors of different voxels of $R(\vec{x})$ or different times in $S(t)$ are correlated with each other. Fully characterizing these errors could evolve into a significant project in itself, and it is not clear that the payoff could justify such an investment of effort or computation.

Although a full estimate of lightmap errors with correlations would probably be computationally quite intensive to produce, it might be possible to estimate the independent errors of each voxel of the position lightmap $R(\vec{x})$ or each independent run making up $S(t)$ by treating the other function as perfectly known, as described above. This would generally produce an underestimate of the uncertainty in each, but the estimate might still give some benefit.

To produce a more accurate estimate of errors, it would probably be necessary to do a simultaneous fit by varying both $R(\vec{x})$ and $S(t)$ together. In the current scheme, $R(\vec{x})$ contains far more complexity than $S(t)$ with roughly 50,000 non-empty voxels, so for each APD gang we would need to simultaneously vary roughly 50,000 parameters to obtain the optimal lightmap. It is exactly this time-intensive process which was avoided by choosing the iterative approach for measuring the lightmap; however, it would only need to be performed occasionally when deriving a new lightmap, so it is not infeasible to imagine attempting this project. The prospect of feeding in a high-quality guess obtained from the iterative method presents an additional significant time-saver. This method would not fully account for the cor-

relations between errors of the different voxels of $R(\vec{x})$ or runs in $S(t)$, but it would come closer than the naive method described earlier.

However, it is also possible that identifying the error of each voxel or run is heading down the wrong path. As described earlier, it is likely that the optimal (lowest-error) method for estimating the lightmap will be an unbinned method such as a locally-adaptive kernel regression method. Error estimation in kernel regression presents significant additional challenges compared to errors from binned parametrizations. At present, I am not aware of any simple scheme to manage this difficulty, meaning that there may be a paradoxical tradeoff that using the best method for minimizing lightmap errors simultaneously makes those errors infeasible to estimate.

Note that under the iterative method, the most naive method for estimating errors is not valid. It might appear that when $S(t)$ is initialized to a constant value of 1, we could also assign to it some constant error. Then when we compute $R(\vec{x})$, we could propagate independent errors from the fit uncertainties of signals and from $S(t)$; and when we compute $S(t)$ we could propagate independent errors from the fit uncertainties and from $R(\vec{x})$; and so forth. However, such a scheme provides no compensating feedback mechanism to force the iterated errors to a reasonable or accurate value, so there is no reason to believe the errors from such a system (if, that is, they converge at all). This difficulty may underscore the fundamental challenge associated with measuring the lightmap errors within our scheme – iterative methods are well-suited to solving a system, but when correlated errors are mistreated as uncorrelated an iterative method can easily magnify the

impact of that mistreatment.

On the topic of convergence, it has been mentioned already that by starting with a generally accurate initial guess for $S(t)$ as constant, the iterative solution method tends to converge rapidly. As a result, and because iterations take only a few hours to perform on a single machine, we currently perform three iterations and claim that convergence is approximately reached. Ideally, we would require that none of the position voxels or runs change value within an iteration by more than some fraction of their estimated errors; but in the absence of estimated errors, this is of course impossible.

It would be possible, in a conservative approach, to require each value to converge to some small fraction of an ADC unit, ensuring that the convergence is better than our ability to measure signals. Such a requirement might force us to compute more iterations than are truly warranted by our lightmap errors, but given the reasonable speed of each iteration, such a method still might not be unreasonable.

5.3 Implementation for this Analysis

The physics analysis which will be described in this paper includes data from EXO runs 2464 to 5597, which were taken between October 5, 2011 and September 1, 2013. However, at the time when the initial denoising processing was begun, the tentative range of runs to be used only extended up to 5367 on June 24, 2013. As a result, calibrated data at that point was only available up to June 24, 2013, and the lightmap had only been generated using the same set of Thorium source data.

When the run range for the present analysis was extended, a significant portion of the dataset had already been denoised with the lightmap based only on data extending to June 24, 2013. Although the possibility of creating a new lightmap was considered, this would have required a re-analysis and re-verification of the existing denoised dataset. As a result, the existing lightmap continued to be used. The functions $S(t)$, which had only been directly measured up to June 24, 2013, were assumed to remain constant between June 24 and September 1, 2013; no known changes to the APDs occurred during this time, nor did any known environmental factors change, so this assumption was considered acceptable. Future lightmaps of course will make use of a more complete dataset rather than relying on extrapolation.

Furthermore, one bug was discovered in the lightmap which was used for denoising. A set of Radium-226 source data was taken before the corresponding identifier could be set in data files, and as a result they were provisionally labeled as Thorium runs. These runs were mistakenly incorporated into the generated lightmap, and events from the 2204-keV gamma line of the Bismuth-214 daughter product of Radium-226 were selected and handled as though they were legitimate 2615-keV events.

It was possible to partially remedy this after the fact: since currently there is a one-to-one relationship between individual source runs and their corresponding points in the functions $S(t)$, it was possible to artificially erase the data points of $S(t)$ originating from Radium runs. It is not so easy to remove the impact they may have had on $R(\vec{x})$. However, the Radium runs were taken at a location which is extremely well-populated by Thorium data throughout the life of the detector; since

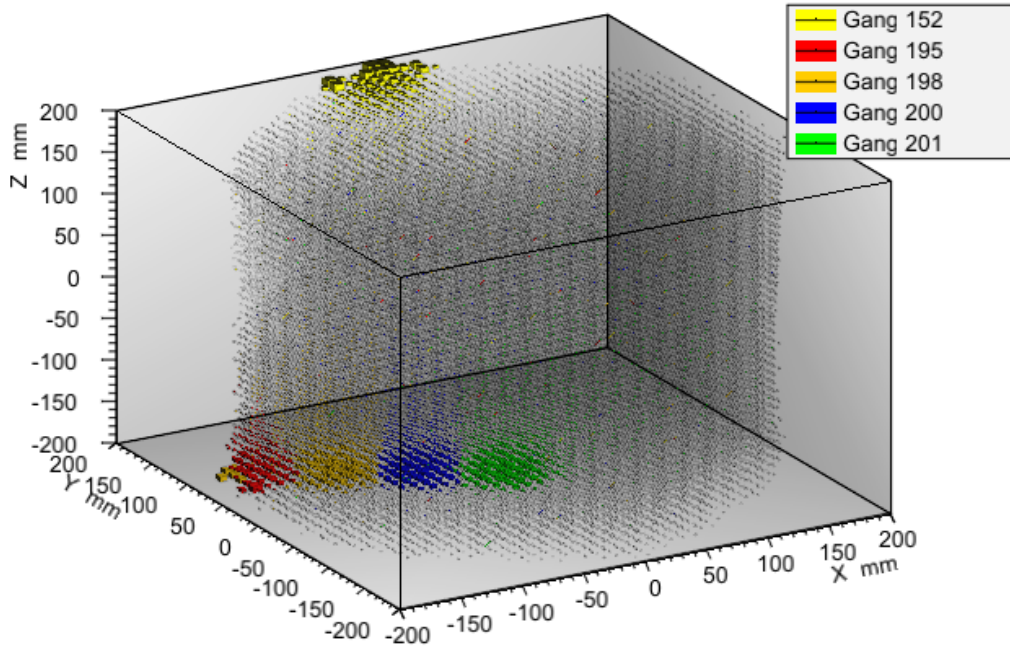


Figure 5.1: Lightmap position-dependence $R(\vec{x})$ for selected APD gangs.

the quantity of Radium data is small by comparison, the effect on $R(\vec{x})$ is presumed to be quite small. Subsequent studies using a correctly-generated lightmap on small subsets of data indicate that the effect is indeed negligible, as expected.

5.4 Visualization

Although it is not strictly necessary to be able to visually inspect the lightmap for it to be useful, nevertheless it is reassuring to see that the lightmap is qualitatively similar to intuitive expectations of how light should propagate through the detector. We have chosen to store the position-dependent $R(\vec{x})$ for each APD gang as a set

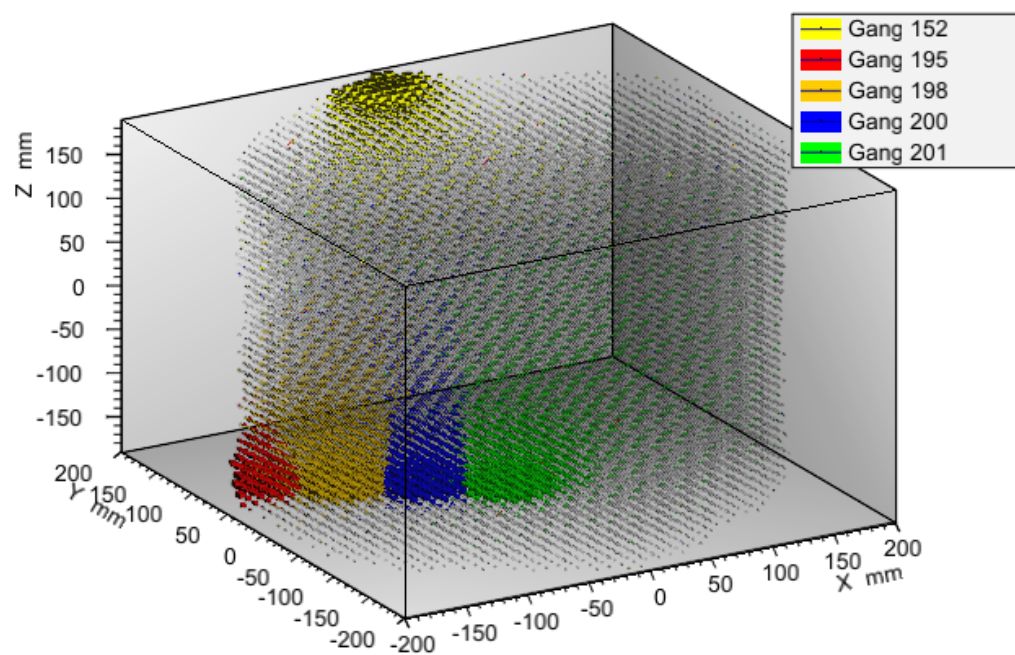
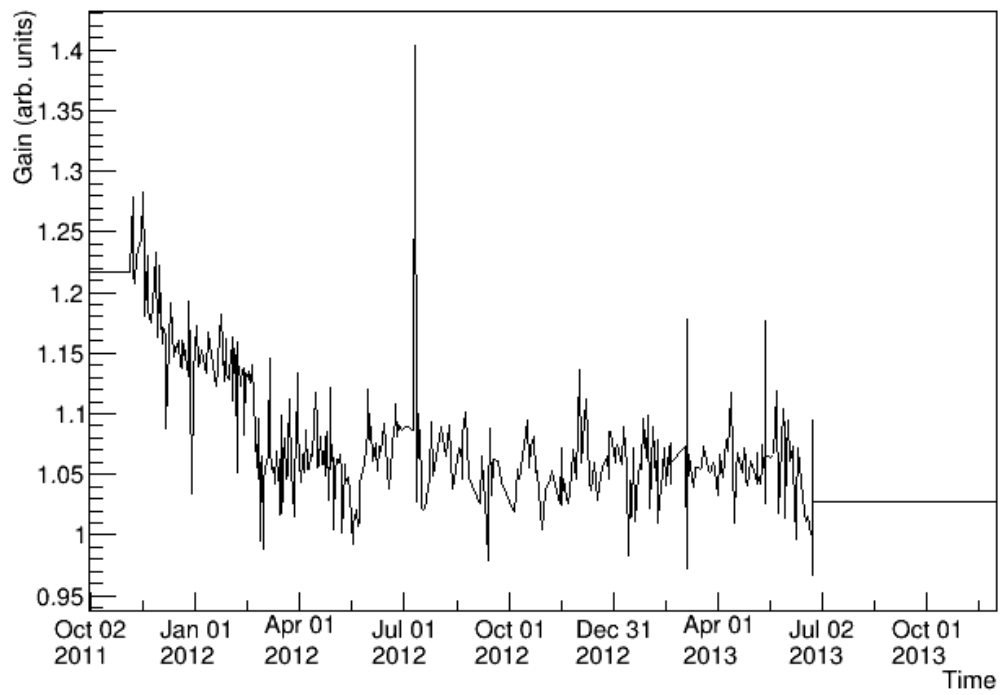


Figure 5.2: Lightmap position-dependence $R(\vec{x})$ for selected APD gangs. Here extreme anode positions are omitted to permit better contrast for the lightmap in the fiducial volume.

Gain on Channel 152



Gain on Channel 195

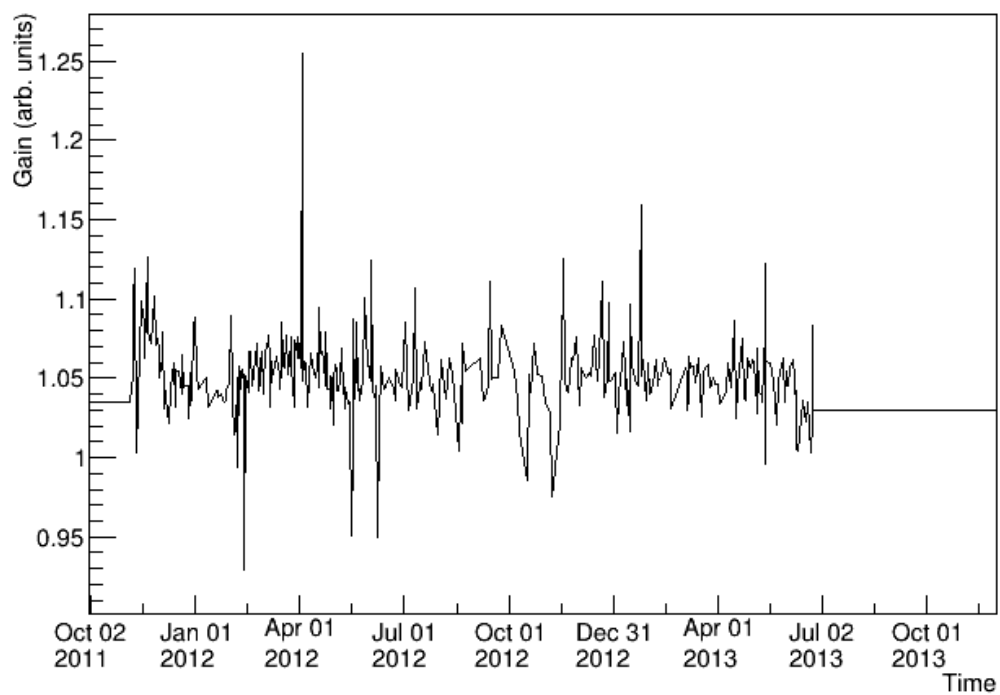
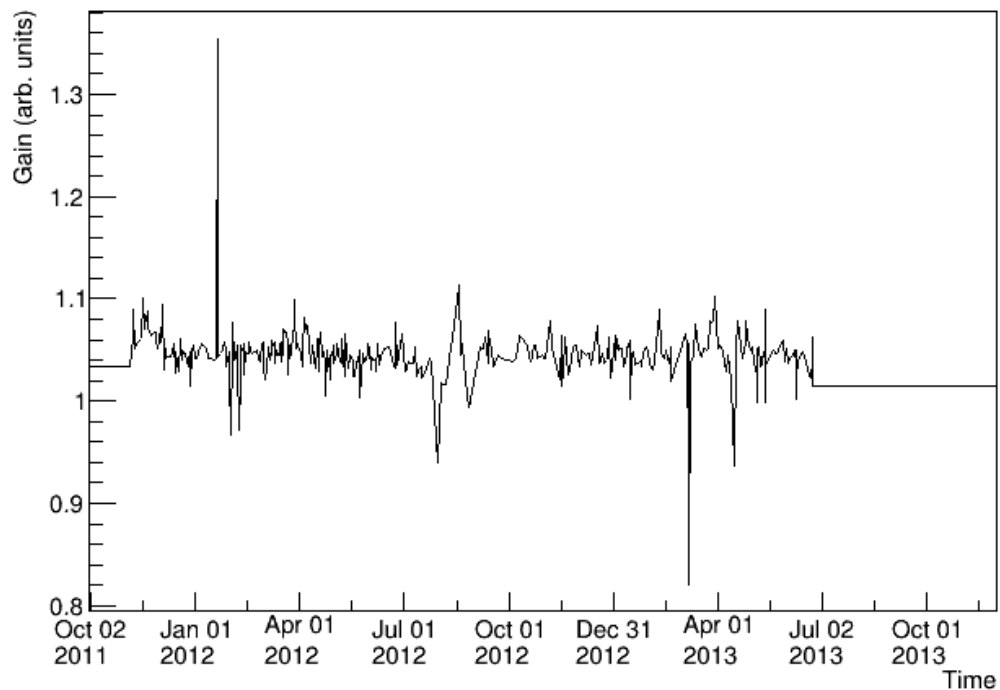


Figure 5.3: Functions $S(t)$ for selected channels.

Gain on Channel 198



Gain on Channel 200

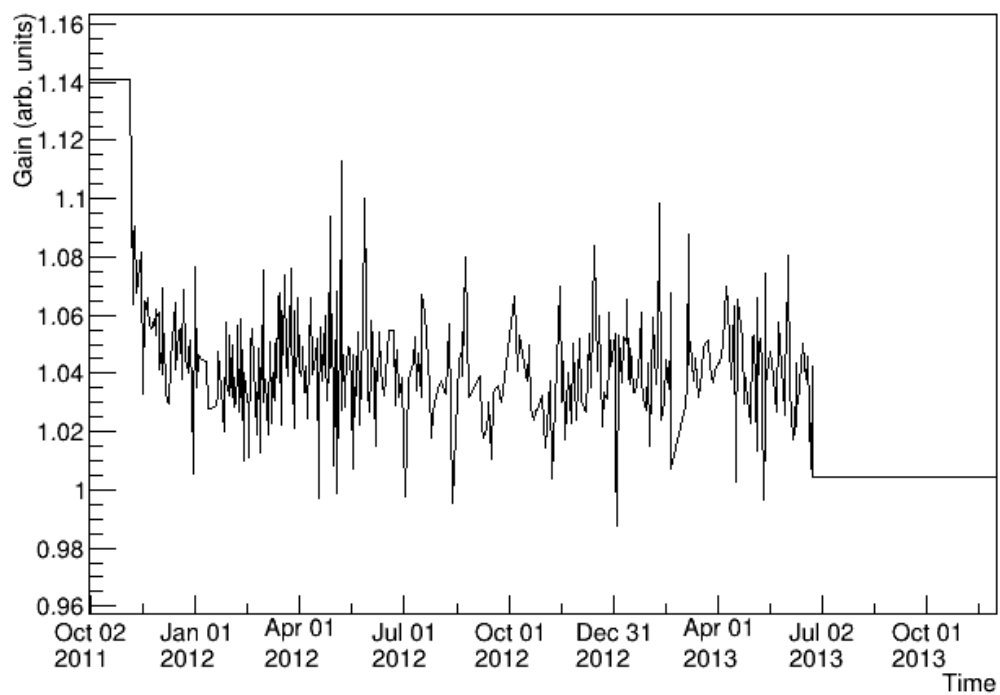


Figure 5.4: Functions $S(t)$ for selected channels.

Gain on Channel 201

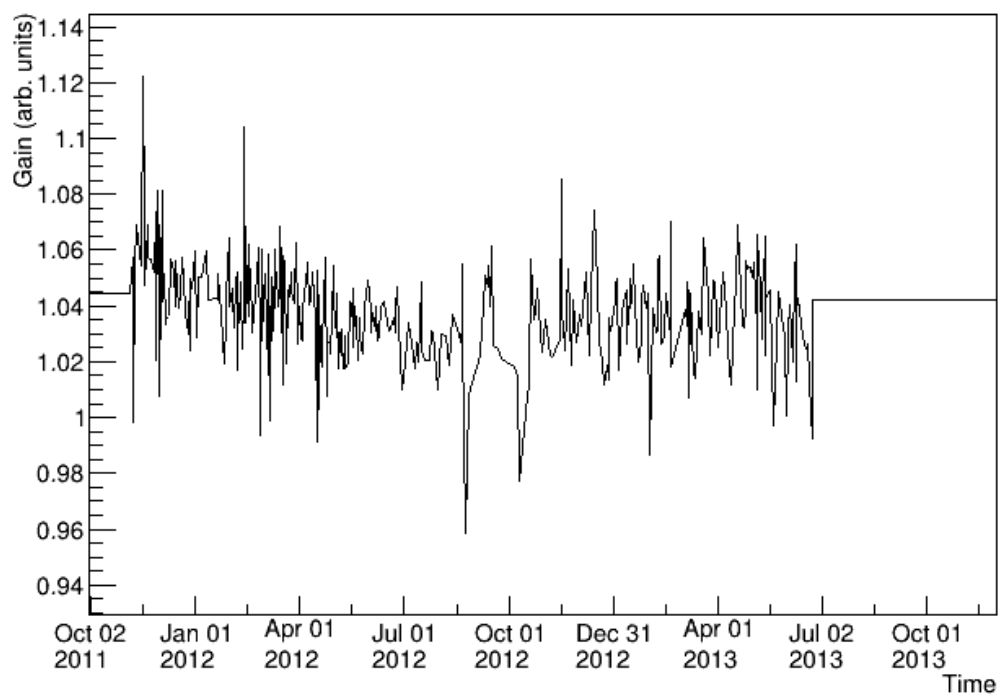


Figure 5.5: Functions $S(t)$ for selected channels.

of ROOT TH3D objects, and fortunately ROOT provides a number of excellent plotting features suitable for a three-dimensional dataset. In figure 5.1, it is possible to view the values of $R(\vec{x})$ for a sample of gangs on top of each other. Larger boxes and denser color indicates a higher yield on the APD gang in question, and it is immediately apparent that events near the anodes produce light which is highly concentrated on a single APD gang.

Figure 5.1 shows the highest yield on the very boundary of the detector, well outside of our fiducial volume; to permit us to more easily view contrast inside of the detector, figure 5.2 shows the same map while omitting the most extreme bin near either anode. Viewing this map, we can see more interesting characteristics of the lightmap:

- Events near the anodes show a high signal concentration on the one gang nearest to their position; however, even deep into the detector near the cathode it is still possible to see the higher concentration of signal on the gang directly aligned with the event.
- We can also see, from gang 201 (green) in this visualization, that events can produce significant signal on APD gangs which which they are not directly aligned (in the Z direction); yield on gang 201 can be seen to decrease smoothly in all directions.
- APD gangs in the corners of the detector, such as gang 195 (red), are not effective at measuring light from events which are far away; even directly above gang 195, it is clear that gang 198 is more effective at collecting light

farther away than about five to ten centimeters. This can be attributed to the reflection of photons by teflon, which may enhance the light yield on gangs which are not hidden in corners.

Figures 5.3, 5.4, and 5.5 show the functions $S(t)$ for the same sample of gangs. The vertical scale can be treated as having arbitrary units; we note that all of these functions lie roughly around 1, which is attributed to the initial placement of $S(t) = 1$ in algorithm 2. We draw the following primary observations from these plots:

- Many of the gangs show their values of $S(t)$ decreasing rapidly up to around February 2012; some of the gangs also show a sharp decrease in value at that point. The decrease in gain corresponds with observations which were made at the time, leading to a decision to replace electronics on some APD channels on February 23, 2012. Thus, we do see “real” features from these plots.
- The functions $S(t)$ are otherwise dominated by jitter between points, indicating that we do not collect enough statistics from each run to sufficiently constrain $S(t)$. This is taken as the strongest evidence that we should use a coarser time binning for $S(t)$, as described in section 5.2.2. Preliminary work has been performed to do this with more recent lightmaps, but no studies have evaluated the impact on energy resolution.
- Individual points on these functions may spike by as much as 40%. These points have been investigated, and their cause is not understood. These jumps,

along with the overall jitter, will certainly be reduced by the use of a coarser time binning.

Chapter 6: EXO-200 Analysis and Results from Denoising

Data analyzed for the present work extends from October 5, 2011 to September 1, 2013. In this chapter, sections 6.1-6.4 describe the basic elements of the EXO-200 analysis. Section 6.5 will present the results from this set of data. In section 6.6 we compare the results obtained using the denoising scheme of chapter 3 to the results which would have been obtained without that algorithm applied, and demonstrate that denoising has contributed to the strength of our physics reach.

6.1 Simulation

Here we will describe the simulation of radioactive sources in the EXO-200 detector. We begin by describing the framework for simulating the deposition of energy from primary decay particles into the liquid xenon and surrounding materials. From there, we continue to describe the simplified electric field model which permits us to model the drift of ionization towards the anode wires.

6.1.1 Simulation of Particles using GEANT

To simulate the deposition of energy from primary decay particles, version 4.9.3p02 of the GEANT software package is used. [65, 66] This package includes a database containing attenuation properties of many common materials as well as detailed decay modes for most radioactive isotopes. Angular correlations between gammas are not modeled with this version of the software, but that is expected to be a minor detail and will be corrected by upgrading to a newer version of GEANT in the future. Forbidden beta decays are generated with an incorrect beta spectrum in the default GEANT software; this is addressed by the EXO collaboration by using our own beta spectra where appropriate.

A model of the EXO-200 detector is simulated in GEANT with a collection of simple geometric volumes, which can be composed to form more complicated structures. Simulation speed decreases as more volumes are generated, and we expect that it is unimportant to simulate details much smaller than the distance between the detail and the liquid xenon. We attempt to find a balance between accurate modeling of detailed features and simplification of distant features. In figure 6.1 we see the full geometry described in GEANT, where distant objects are constructed from a small number of geometric pieces. Figure 6.2 shows how the TPC is described in GEANT, and we can see the level of detail is much greater.

To simulate particles, GEANT uses a Monte Carlo method. It models particles as taking a sequence of steps, where each step is randomly generated; the probability distribution of each choice of step is determined by known properties of the particle,

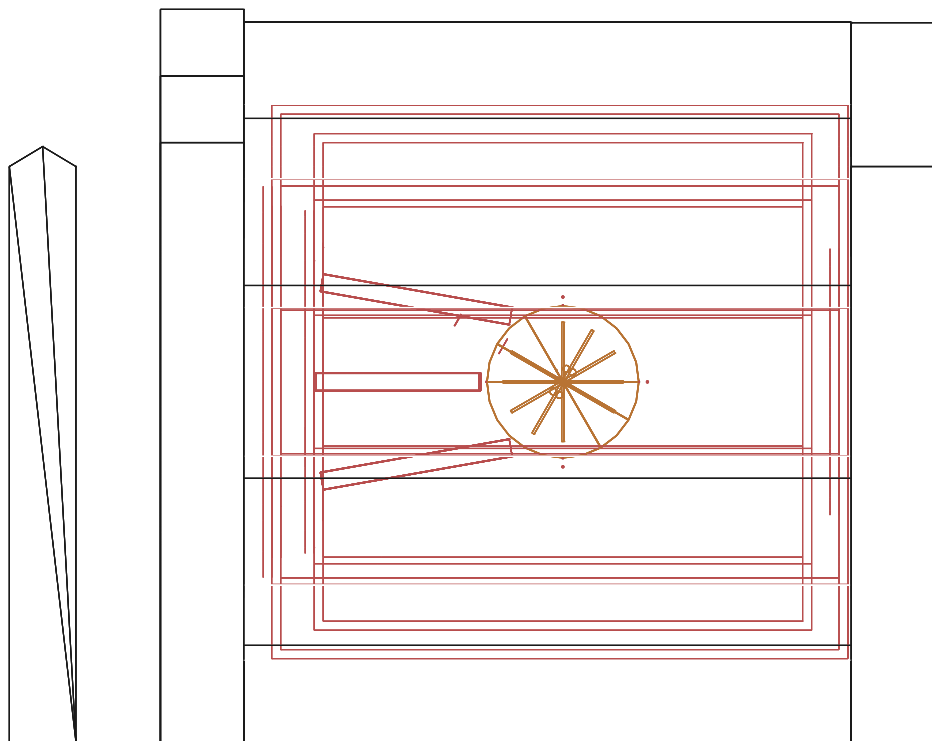


Figure 6.1: The GEANT simulation includes large-scale features of the EXO-200 detector, including the outer and inner lead wall (black), outer and inner cryostat and TPC legs (red), and the TPC itself (brown). Components are assembled from simple geometrical shapes, and distant objects are only described coarsely. [49]

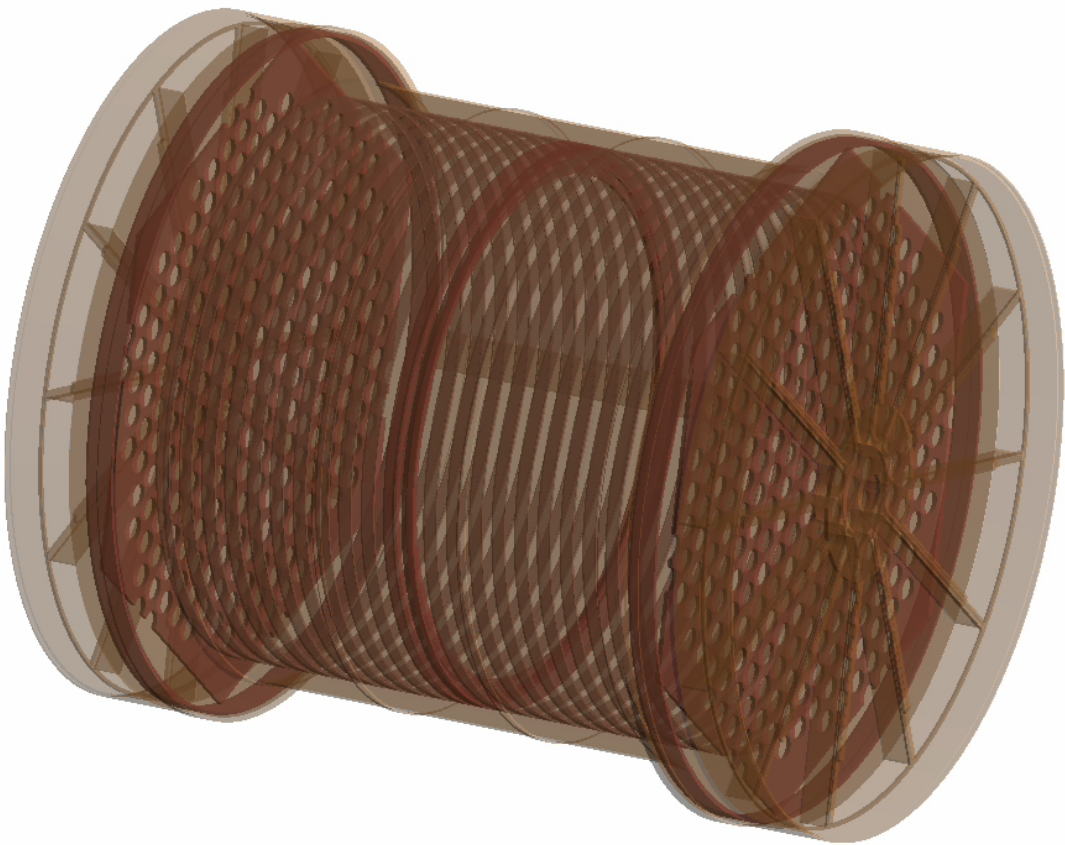


Figure 6.2: Detector components which are close to the liquid xenon are simulated in GEANT with far greater accuracy than distant objects, to reduce computational time. [49]

the energy of the particle, and the properties of the attenuating material. The precise set of physical processes which determine the probability distribution is user-selected, and in EXO-200 has been chosen to include all processes which are significant within our energy range of 10 keV to 10 MeV. [49]

Only energy which deposits in the liquid xenon is observable. When primary decays are simulated far from the detector, it may be that most of those simulated events deposit no energy in the liquid xenon and are not observable; the simulation must continue running until a sufficient number of simulated events deposit energy in the liquid xenon. This means that sources which are farther from the liquid xenon require significantly more computational time to accumulate a usable number of statistics. We find that sources outside of the HFE are subject to 4.5 attenuation lengths before reaching the liquid xenon, and events reaching the liquid xenon from the inner cryostat can only be simulated at 0.01 Hz/core by this approach. [49]

To improve this rate, importance sampling is employed for distant sources. This approach consists of the following techniques to magnify statistics from a fixed simulation time:

- Low-energy beta and alpha particles outside of the TPC may be “killed”, or prematurely eliminated from the simulation based on an expectation that they will not deliver any energy to the liquid xenon.
- The detector is surrounded by importance sampling “boundaries”: when a particle passes into a boundary it may be cloned (with a user-selected probability), where the rate of cloning is tracked by a corresponding decrease in

particle “weight.”

- To avoid biasing the spectrum, it is also necessary to kill particles which pass out of a boundary with the same probability, and increase their weight accordingly.

This approach has the effect of using GEANT to simulate the properties of particles reaching the outermost boundary; then draw samples from that distribution and simulate the properties of particles reaching the next boundary; and so forth, amplifying the impact of statistics at each stage. Further details on this approach can be found in [67]; it has the effect of increasing simulation speeds from the inner cryostat from 0.01 Hz/core to a few Hz/core, and makes simulations of backgrounds from outside the lead wall feasible. [49]

The result of these GEANT simulations is a measurement of the efficiency with which events from various sources reach the liquid xenon, and also an understanding of the energy and position distributions of energy deposits from these sources. Representative spectra of our primary backgrounds, ^{238}U and ^{232}Th , are shown in figures 6.3 and 6.4 respectively.

6.1.2 Digitization of Waveforms

After energy deposits are simulated using GEANT, it is necessary to model the conversion of those energy deposits into collection of scintillation and ionization, and then the generation of digitized waveforms resembling the waveforms which are collected in real data.

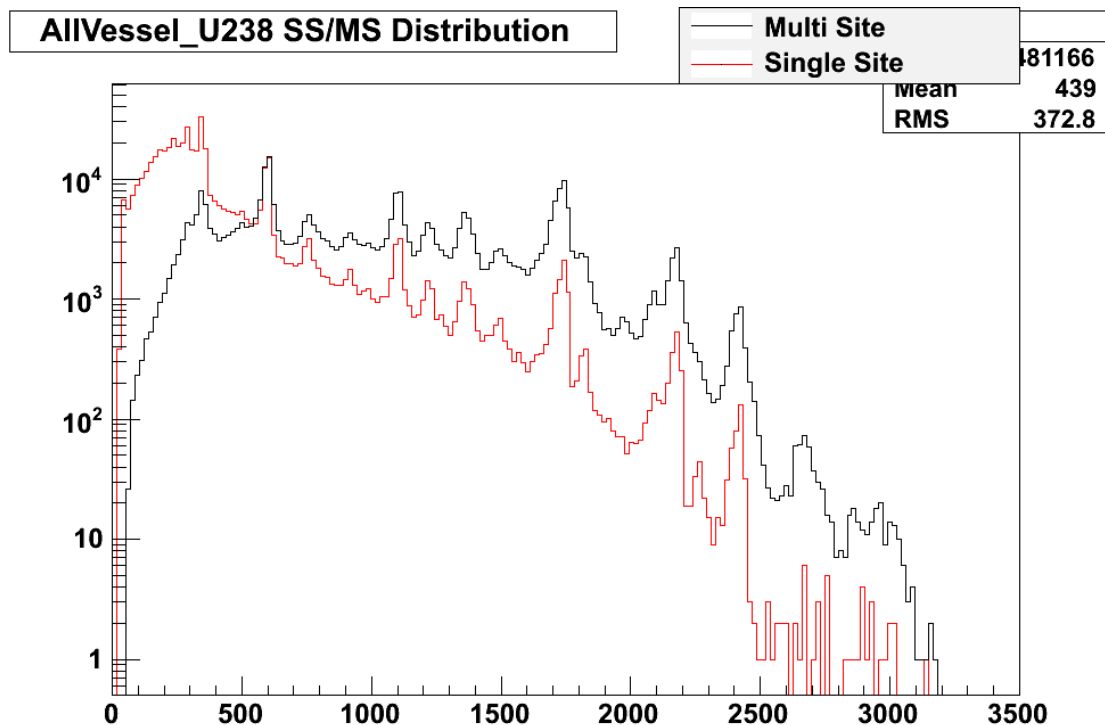


Figure 6.3: Energy spectra from ^{238}U in the TPC vessel; single-site and multi-site energy spectra are shown separately. [49]

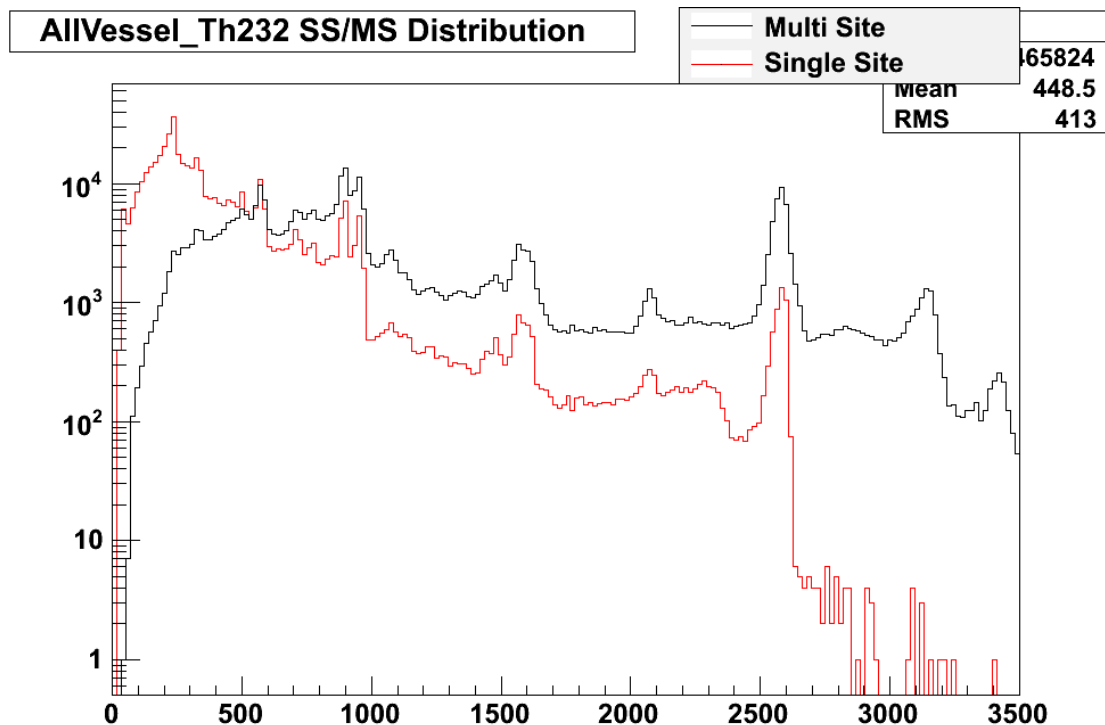


Figure 6.4: Energy spectra from ^{232}Th in the TPC vessel; single-site and multi-site energy spectra are shown separately. [49]

To generate a scintillation signal, a purely empirical model is used to estimate the relative signal magnitudes on the north and south APD planes. This model only takes into account Z -dependence of the light collection, and does not incorporate the different light yields expected on each individual APD channel. This model is therefore rather crude, and can only be used as a rough check on the signal-finding efficiency for scintillation as a function of energy. Attempts to track optical photons in the TPC have met with only partial success which is insufficient to justify their significant computational cost. Thus, the EXO simulations are unable to model most aspects of scintillation signals. Section 6.4 will describe the methods used to cope with this aspect of simulation.

Simulation of charge signals is better-understood. The detector is modeled by a two-dimensional geometry where, rather than one-dimensional wires arranged in two-dimensional planes, we have wire “points” at fixed voltage which are grouped in a one-dimensional pattern. The v-wires are treated as stacked directly on top of the u-wires; it is impossible to model the true orientation of the v-wires which is rotated relative to the u-wires, but this has generally proven to be a negligible detail for us. Only one TPC half is modeled because of the approximate mirror symmetry of the detector across the cathode. Only a few wires are simulated in the second dimension because the electrostatic effect of any one wire will not extend beyond a few wire spacings. This model is illustrated in figure 6.5. [49]

Electrostatic effects are simulated using the ANSYS Maxwell field simulator. To simulate the electric fields in the detector, wires are treated as circles with a radius matching the approximate radii of the physical wires, with a constant voltage on

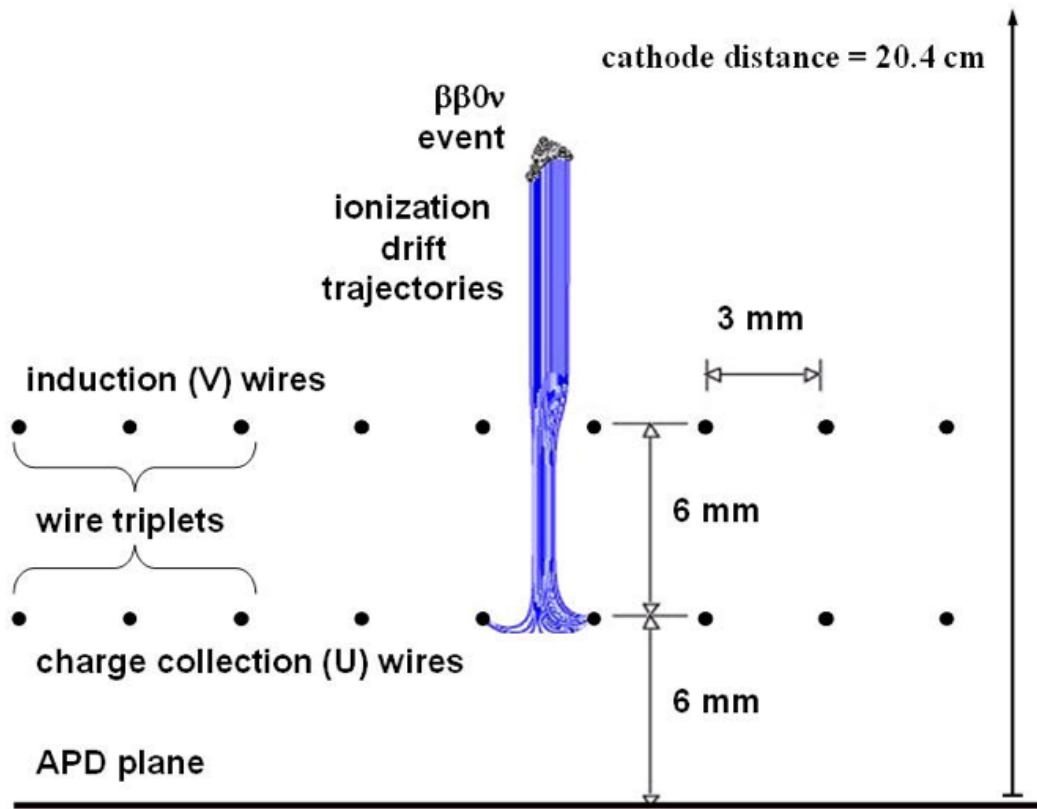


Figure 6.5: The wire planes are modeled in only two dimensions; charge drifts along the field lines, which are arranged to terminate only on the u-wires. [49]

their surfaces. The APD plane and cathode plane are treated as constant-voltage boundaries, and a periodic boundary condition is established on the two remaining boundaries of the model geometry.

These electric fields can be used to trace the paths followed by charge deposits in the detector. Charge deposits are drifted in small steps based on the direction of the electric field. The speed of drift is taken from external measurements rather than from the magnitude of the electric field; in most of the bulk of xenon, the electric field and drift velocity are treated as constant, but near the u-wire plane the drift velocity is increased slightly to account for higher electric fields experienced in that region of the detector. Charge attenuation due to finite purity can be modeled at this step, but generally is treated as infinite here; charge diffusion effects are ignored.

We have discussed in section 2.5 that charge is induced on the u-wires and v-wires; this means that we must record the amount of charge induced at each step along the drift path of the charge deposit. This is done based on the Shockley-Ramo Theorem, which states that the change in induced charge δq_i on an electrode i is equal to:

$$\delta q_i = Q \delta W_i, \quad (6.1)$$

where Q is the total drifting charge and W_i is the weighting potential of electrode i , defined as the potential which would be induced in our geometry if the potential on electrode i were set to 1 and the potential on all other boundaries were set to 0. [68, 69] Figures 6.6 and 6.7 illustrate the weighting potentials of a u-wire and

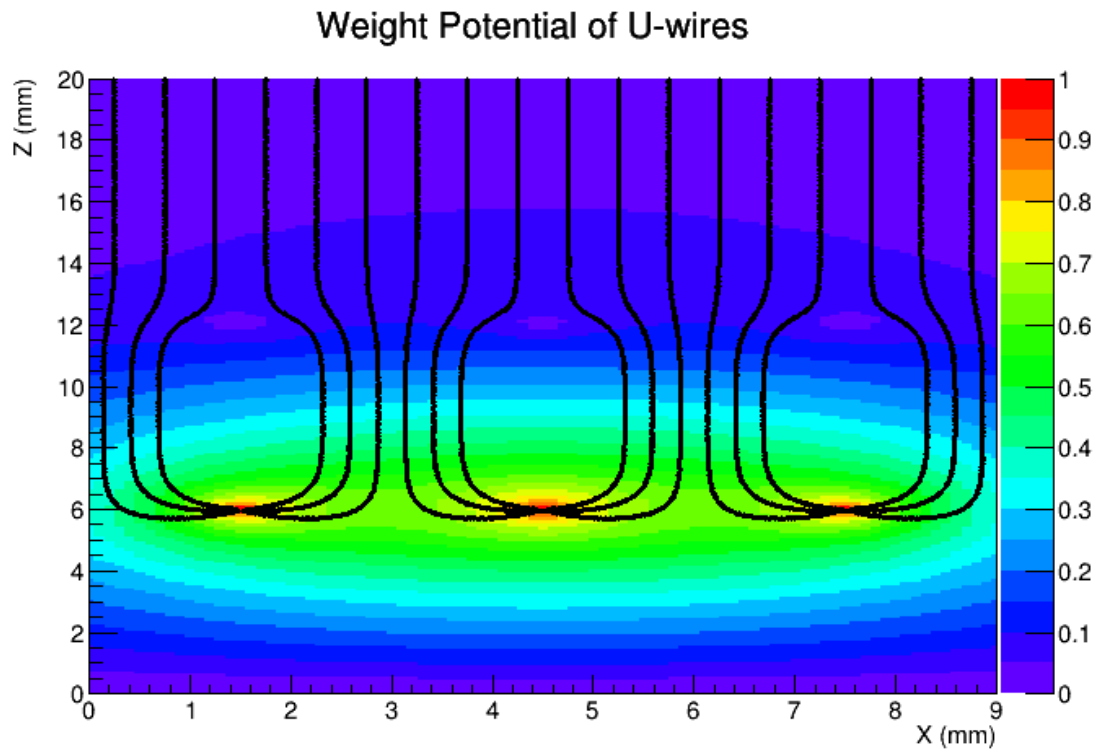


Figure 6.6: Weight potential of a u-wire channel consisting of three ganged wires. Electric field lines are superimposed. [49]

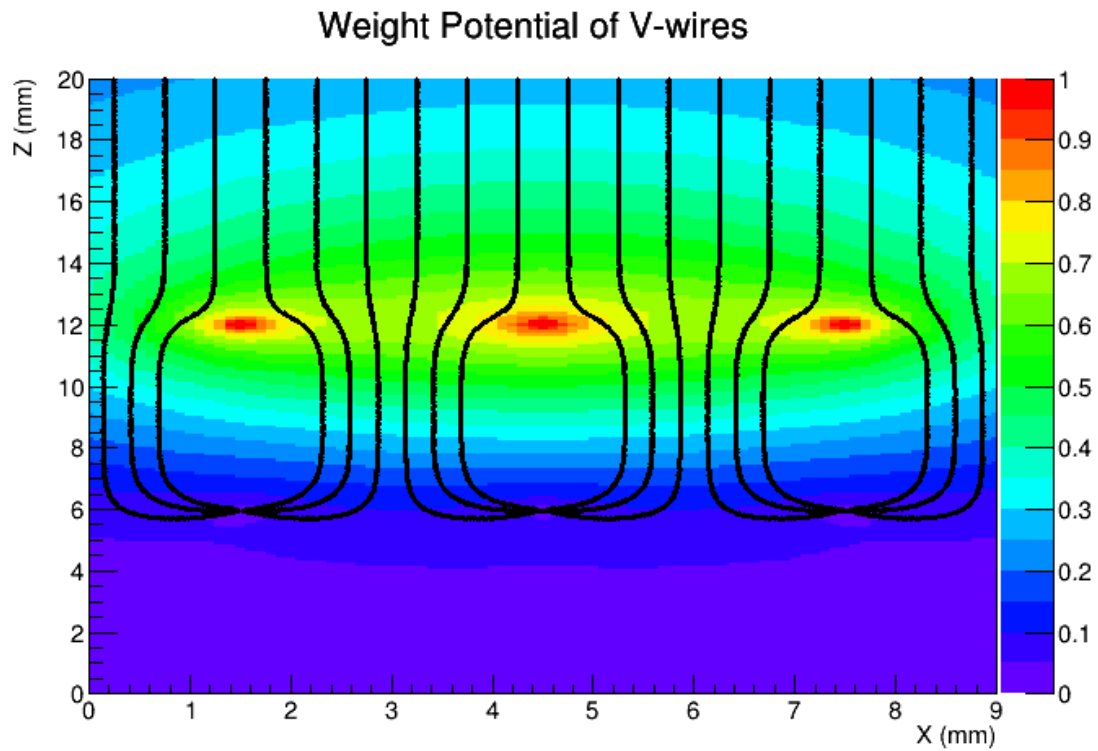


Figure 6.7: Weight potential of a v-wire channel consisting of three ganged wires. Electric field lines are superimposed. [49]

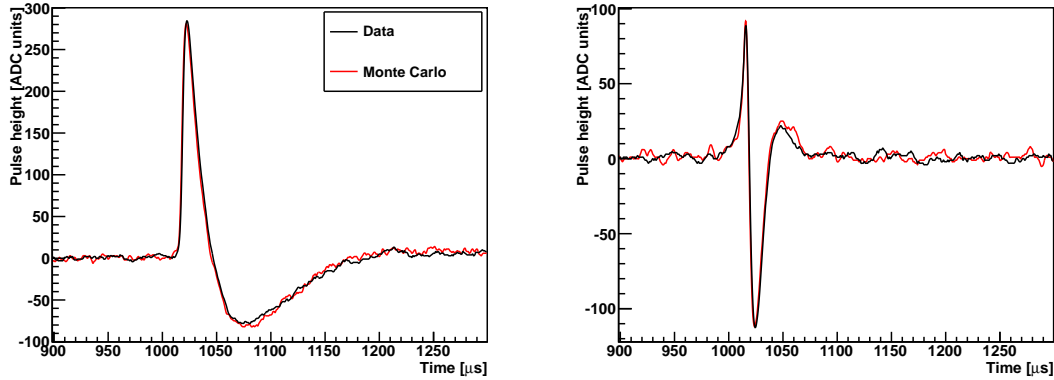


Figure 6.8: Comparison between simulated and observed waveforms on a u-wire (left) and v-wire (right) from ^{228}Th sources. The events are chosen to have similar energies so that the magnitudes match. [49]

v-wire channel, respectively.

Finally, the functions of integrated charge versus time must be converted to shaped digitized waveforms, and noise must be added. The shaping and gain amplification is performed to match the electronics described in section 2.5. To ensure accurate time shaping, the functions are all sampled at a bandwidth of 10 MHz, and then downsampled after shaping to the nominal 1 MHz. Digitization is performed by converting voltages into units of ADC counts, then truncating to an integer value. To model saturation effects, this number is pulled into the integer range $[0, 4096]$.

Finally, we have found that the most effective way to add electronic noise to the signals is by extracting a set of representative noise waveforms from real data. These are taken from a large number of solicited triggers which have been checked for the absence of a coincident event. To increase the number of noise signals available, the noise waveforms sampled from the detector are spliced together, and simulated

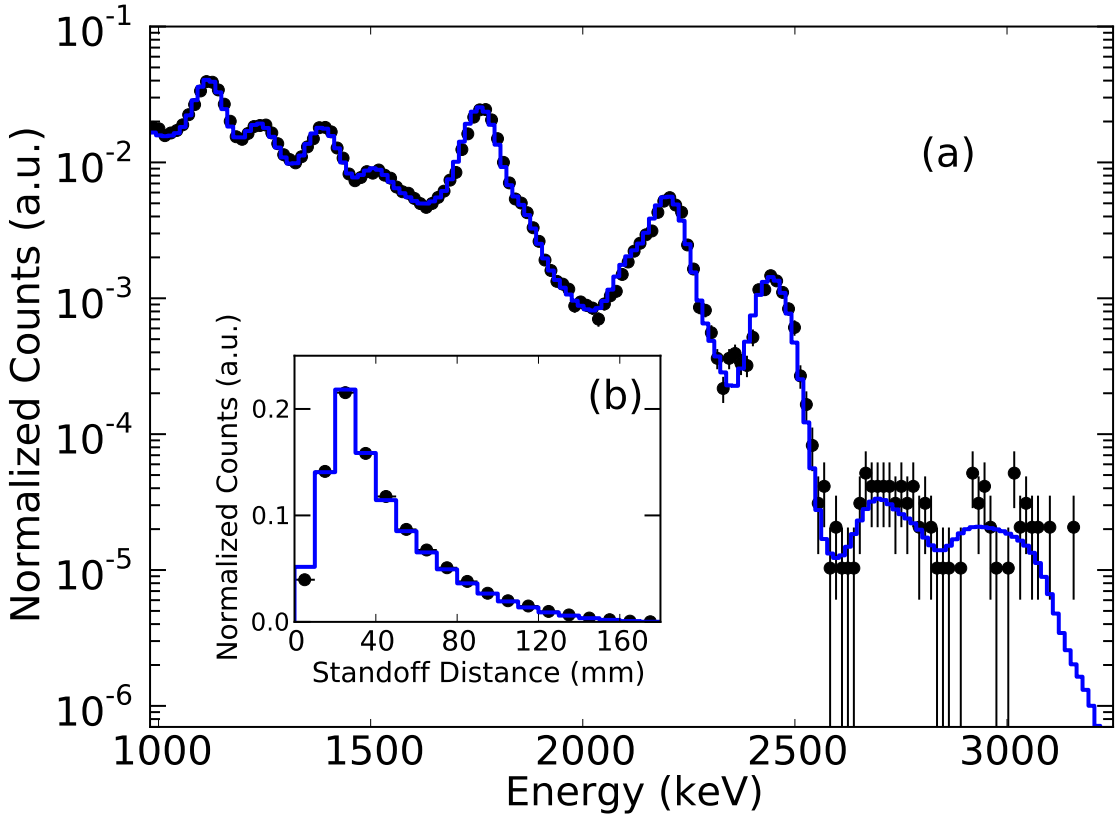


Figure 6.9: Comparison between simulated and observed energy spectra (a) and standoff distance (b) in single-site ^{226}Ra events from a source located at position S5. [35]

events may draw their noise from any subrange of the spliced-together noise waveform. This method has been found to agree better with data than noise simulations using a random-number generator. Figure 6.8 compares waveforms observed from a sample event in data and simulation. [49]

In this way, we are able to generate simulated data which in most respects resembles real data collected from the detector. The EXO-200 simulation has shown remarkable agreement with the detector in the properties of energy and cluster location, as illustrated in figure 6.9. A significant effort has been made to achieve

excellent agreement between simulation and data, and the result is that we can claim a strong understanding of the behavior of the EXO-200 detector.

6.2 Cluster Reconstruction

The first stage of data processing involves locating candidate pulses in its waveforms, and fitting for the magnitude and time of any candidate pulses which are found. The methods of accomplishing this will be described in sections 6.2.1 and 6.2.2. We will complete our description of cluster reconstruction with a brief explanation of the approach to the clustering of waveform pulses into three-dimensional clusters in section 6.2.3.

6.2.1 Pulse Finding

Pulse-finding proceeds in two steps. First, on all waveforms a matched filter is applied to do a preliminary search on all channels. Then, a secondary search is performed on the u-wire signals to improve sensitivity to multiple signals near in time.

The matched filter algorithm was first described by D.O. North in 1943. [70] It attempts to decide between the null hypothesis that a waveform $X[\tau]$ consists of only noise and an alternative hypotheses that the waveform contains both signal and noise:

$$\begin{cases} H_0 : & X[\tau] = n[\tau] \\ H_1 : & X[\tau] = s[\tau] + n[\tau]. \end{cases} \quad (6.2)$$

We search for a linear functional L_0 which will act on $X[\tau]$ and maximize the expected signal-to-noise ratio,

$$SNR = \frac{(L_0 \{s[\tau]\})^2}{\langle (L_0 \{n[\tau]\})^2 \rangle}. \quad (6.3)$$

In other words, if a waveform is composed of only noise, the functional should result in a small value; however, if the waveform contains signal then the functional should result in a large value.

The functional which maximizes the expected signal-to-noise ratio can be expressed as:

$$L_0 \{X[\tau]\} = \mathcal{F}^{-1} \left\{ \frac{\mathcal{F}\{X\}[k] \mathcal{F}\{s\}^*[k]}{\langle \mathcal{F}\{N\}[k] \mathcal{F}\{N\}^*[k] \rangle} \right\} [0], \quad (6.4)$$

where \mathcal{F} represents the Fourier transform. This expression has an added benefit that if instead we'd like to test the hypothesis that the translated signal $s[\tau - \Delta]$ is contained in the waveform, we can do so with the test statistic:

$$L_\Delta \{X[\tau]\} = \mathcal{F}^{-1} \left\{ \frac{\mathcal{F}\{X\}[k] \mathcal{F}\{s\}^*[k]}{\langle \mathcal{F}\{N\}[k] \mathcal{F}\{N\}^*[k] \rangle} \right\} [\Delta]. \quad (6.5)$$

Finally, we can define a test statistic T for the waveform $X[\tau]$ to have a signal anywhere with:

$$T = \max_{\Delta} L_\Delta \{X[\tau]\}. \quad (6.6)$$

This expression can be computed efficiently using the fast Fourier transform. The time of the pulse is guessed as the value of Δ which led to the largest value of $L_\Delta \{X[\tau]\}$.

The first phase of pulse-finding performs a search using the matched filter on:

- All u-wire channels.

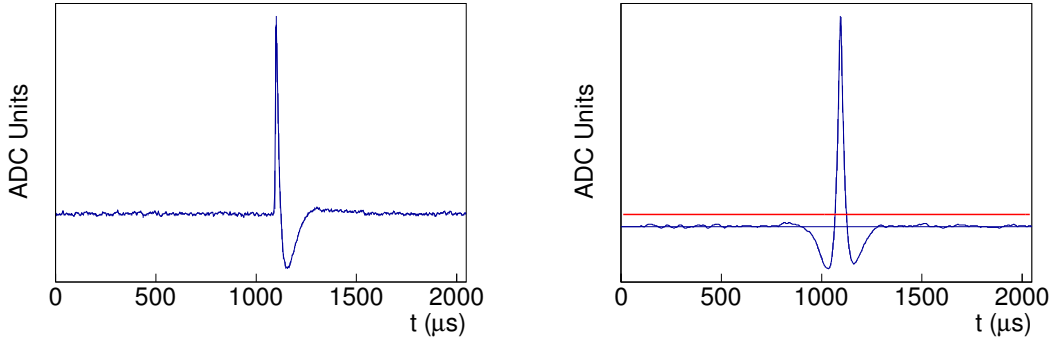


Figure 6.10: A u-wire waveform (left) and the output from operation of the matched filter (right). The red line on the right indicates our signal threshold; the matched filter output exceeds the threshold, so this waveform is determined to contain a signal. [50]

- All v-wire channels.
- The sum of all APD channels in the North plane.
- The sum of all APD channels in the South plane.

An example application of the matched filter to a u-wire waveform is shown in figure 6.10.

The matched filter has proven to be an excellent metric for deciding whether a waveform has a signal on it or not. However, it is not as effective at distinguishing between the cases where one or multiple signals occur on a waveform. We would particularly like to be able to classify u-wire waveforms by the number of distinct signals they contain because these generally provide the best sensitivity for single-site/multi-site discrimination. The matched filter output function is designed to have a tall peak in the presence of a signal, but it may also be a broad peak which is difficult to resolve as the sum of two distinct signal contributions.

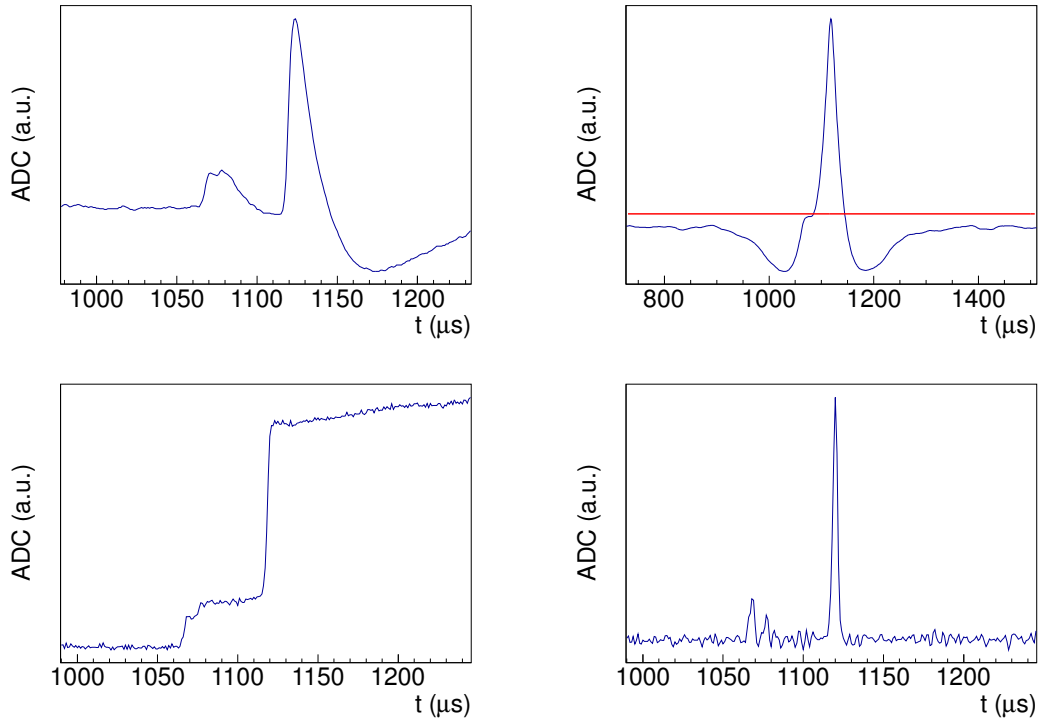


Figure 6.11: A u-wire waveform composed of two signals near in time is shown (top left); the matched filter (top right) correctly detects the presence of signal, but does not detect the presence of two distinct signals. At bottom left, the waveform is unshaped; at bottom right the waveform is reshaped with shorter differentiation times, leading to easier detection. [50]

To improve sensitivity to multiple signals in u-wire waveforms, a second pass is performed on u-wire channels using a multiple-signal finder. This scheme consists of first, unshaping the waveform offline to remove the effect of the shapers; and second, reshaping the waveform using shorter differentiation times than employed by hardware. In a multiple-signal waveform, this has the effect of damping signals faster to reduce their overlap in time. It is then possible to search for signals using a simple threshold which is not as sensitive to small signals as the matched filter, but is capable of detecting additional signals to complement the matched filter. This process is illustrated in figure 6.11, and is the last procedure for finding signals. [50]

6.2.2 Pulse Fitting

After finding signals, it is necessary to perform a fit to the expected signal shape. Fits are performed allowing both the signal magnitude and signal shape to float freely, where only the initial guesses for these parameters come from the finding step. The metric for fits is a simple chi-square between waveform data and the expected signal shape, where error on each point is estimated by the root-mean-square noise of the channel.

To minimize the impact of signal templates which may be imperfect, and also to reduce the effect which waveform noise may have on our fit, we do not fit the entire waveform to our signal model. Instead, we use only an $80\mu\text{s}$ fit window in the case of v-wires and APDs, and a $180\mu\text{s}$ fit window in the case of u-wires. The fit windows are illustrated in example events in figure 6.12.

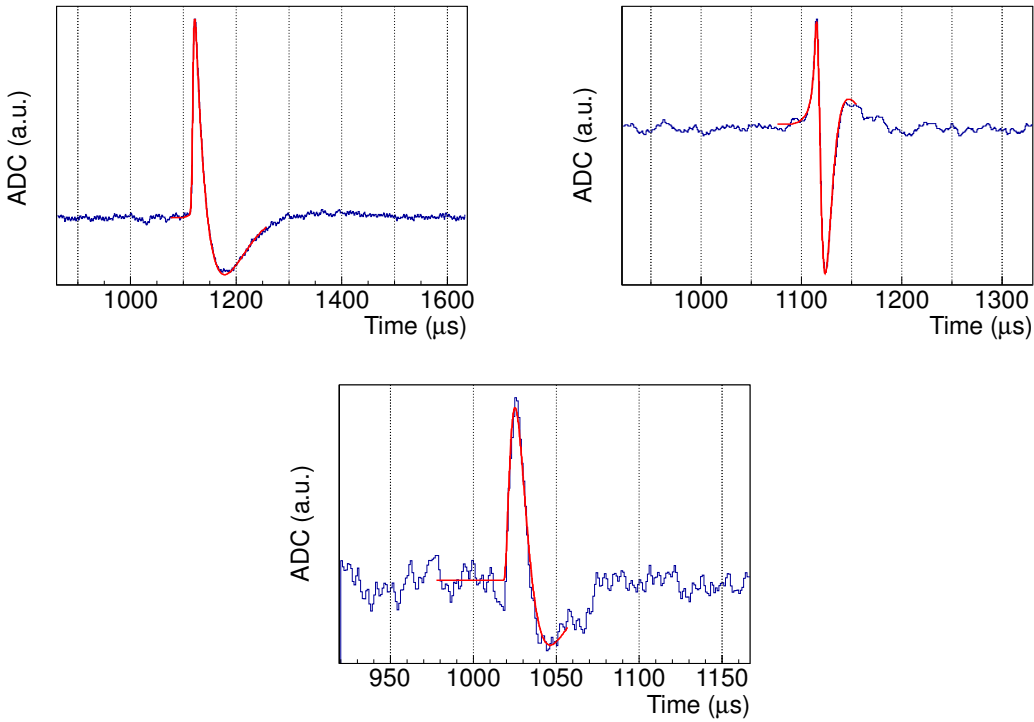


Figure 6.12: Fits to data for a u-wire (top left), v-wire (top right), and summed-APD waveform (bottom). The red model line indicates the time extent of the fit window. [50]

As signal times and magnitudes are extracted, it may be discovered at this phase of processing that two signals which were reported by the finding phase are extremely close together in time. In this case, we can generally conclude that the finding phase inadvertently reported the same signal multiple times; the multiple candidate signals should then be merged together, and the waveform refit. The specific criteria for merging candidate signals includes a combination of signal timing and fit errors from a preliminary fit where all candidate signals are included; details can be found in [50].

6.2.3 Clustering Pulses into Deposit Sites

The result of pulse finding and fitting is a list of pulse magnitudes and times for each channel. It remains for reconstruction to combine this information into three-dimensional clusters, where each cluster should have a three-dimensional position, time, and estimates for charge and light signal magnitudes.

We begin by bundling groups of similar u-wire, v-wire, and APD pulses. Multiple u-wire pulses may be bundled together when they occur on neighboring channels close together in time. This may represent a cluster which occurred halfway between two u-wire channels and was split, with some charge being collected by each u-wire channel; it may also represent a combination of charge being collected on one channel and an induced charge signal on a nearby u-wire channel due to the proximity of the charge drift path to that neighboring channel. V-wire pulses are bundled together based on a combination of signal magnitude and time to account for the

observation that the passage of a single charge cloud will induce pulses on many nearby v-wires. APD pulses are bundled based on time only, particularly to ensure that when a pulse is observed on both the North and South APD planes, the pulses are interpreted as originating from the same event in the detector.

We then attempt to join u-wire pulse bundles and APD pulse bundles into two-dimensional charge clusters, identified by their U-Z positions and the time of the energy deposit. The algorithm to do this is simple: for each u-wire pulse bundle, we join it with the most recent APD pulse bundle in the event. The maximum difference in time is the maximum drift time of charge clusters in the detector, $116\mu\text{s}$. To allow for fit errors in the time parameters of the APD and u-wire pulses, an additional $3\mu\text{s}$ allowance is added on either end of the permitted time difference; thus, an APD and u-wire pulse bundle may be joined if the APD occurred between $119\mu\text{s}$ before and $3\mu\text{s}$ after the u-wire collection time, and from these candidates the latest APD pulse bundle is selected for each u-wire pulse bundle. The cluster's charge energy is the sum of the energies attributed to all of the u-wire pulses in the u-wire pulse bundle; no attempt is made to measure the cluster's scintillation energy.

Finally, we cluster v-wire pulse bundles with two-dimensional charge clusters to form three-dimensional clusters possessing X-Y-Z positions, deposit time, and charge energy. The only information taken from the v-wire pulse bundle is the third position coordinate; it is not used to adjust our estimates of energy. The challenge to this portion of clustering is that charge clusters may arrive at the same u-wire or v-wire at the same time, yet from two different locations. For example, it may be that what appeared to be one u-wire pulse bundle in fact comes from two charge

clusters with common U-Z positions and different V-positions. So, in addition to searching for the most likely associations between u-wire/APD clusters and v-wire pulse bundles, we must consider the possibility of splitting a two-dimensional cluster or v-wire pulse bundle into pieces before performing this association.

To do this, every possible combination of u-wire/APD cluster and v-wire pulse bundle is considered, along with every possible choice of split for clusters or pulse bundles. A likelihood is assigned to each possible combination; this likelihood takes into account:

- The ratio of v-wire and u-wire pulse magnitudes. These pulse magnitudes are expected to be linearly related because they both are observations of the same charge drift cloud, and deviations from that linear relation are penalized by a decreased likelihood.
- The time difference between the v-wire and u-wire pulses. There is an expected drift time between the v-wires and u-wires which is measured from data; if the observed time difference deviates from this expectation, the likelihood is decreased to reflect a preference for a more realistic pairing.
- The two-dimensional position which the pairing implies. Due to the geometry of the detector, not all pairs of u-wire and v-wire can be hit by the same charge cluster. When a u-wire and v-wire lie in different halves of the TPC, it is of course impossible for the same charge cloud to induce pulses on both. In some cases a u-wire and v-wire may almost overlap, and it may be considered possible yet unlikely that the same charge cloud could induce pulses on both;

these instances are penalized as well.

Further details of the clustering criteria may be found in [50].

This section has described the situation where the pulses of an event may be reconstructed as a set of three-dimensional clusters with well-defined position, time, and charge energy. Although every effort has been made to accomplish this whenever possible, in practice there are events for which some clusters may not be fully reconstructible. Primarily this occurs because charge deposited on a u-wire near the edge of the detector where no v-wires exist; because a cluster fell below the threshold for v-wire signal-finding, or the event fell below the scintillation threshold; because the signal finder reported a false positive, yielding a non-physical pulse; or because an event has extremely high multiplicity and it is not possible to select a preferred clustering. Such events are difficult to use in higher-level analyses and will generally be removed, with an associated energy-dependent efficiency loss of 9.1%. [35]

6.3 Energy Corrections

Each cluster which is found can be assigned a preliminary energy estimate based on the fit magnitudes of its pulses. However, to achieve the best possible energy resolution it is necessary to make an assortment of energy corrections. These corrections will be identified in this section. We will first describe the corrections which are made to charge energies on a cluster-by-cluster basis, and then the corrections made to the denoised scintillation energy. Section 6.3.3 describes the calibration of

a combined energy measurement using charge and light together. Finally, in section 6.3.4 we describe the measurement of the energy resolution and compare the resolutions obtained with and without denoising.

6.3.1 Charge Corrections

The preliminary charge cluster energy measurements come from the sum of the u-wire signal magnitudes described in section 6.2.2. These magnitudes reflect the quantity of charge which was collected by the u-wire.

However, each u-wire channel has its own set of electronics, so pulse magnitudes must be adjusted by a gain correction which depends on the channel. These gains are extracted from source data by selecting pair production events from the thorium source, in which a 2615-keV gamma pair-produces an electron and positron, and the positron subsequently annihilates with another electron to emit two 511-keV gammas. The high multiplicity of these events makes it possible to select them accurately, and the process guarantees that a single 1593-keV cluster at the site of the pair pruduction must be truly single-site because it originates from a single energetic electron. These properties make it ideal for producing an accurate u-wire gain measurement. Using the resulting gain corrections, individual u-wire pulse magnitudes are corrected based on their gain, and the charge cluster energy measurements are corrected according to the corrections on their bundled u-wire pulses. [48]

There are also two Z-dependent energy corrections which must be applied to clusters. The first accounts for charge attenuation due to the imperfect purity of

Electron Lifetime measurement, total

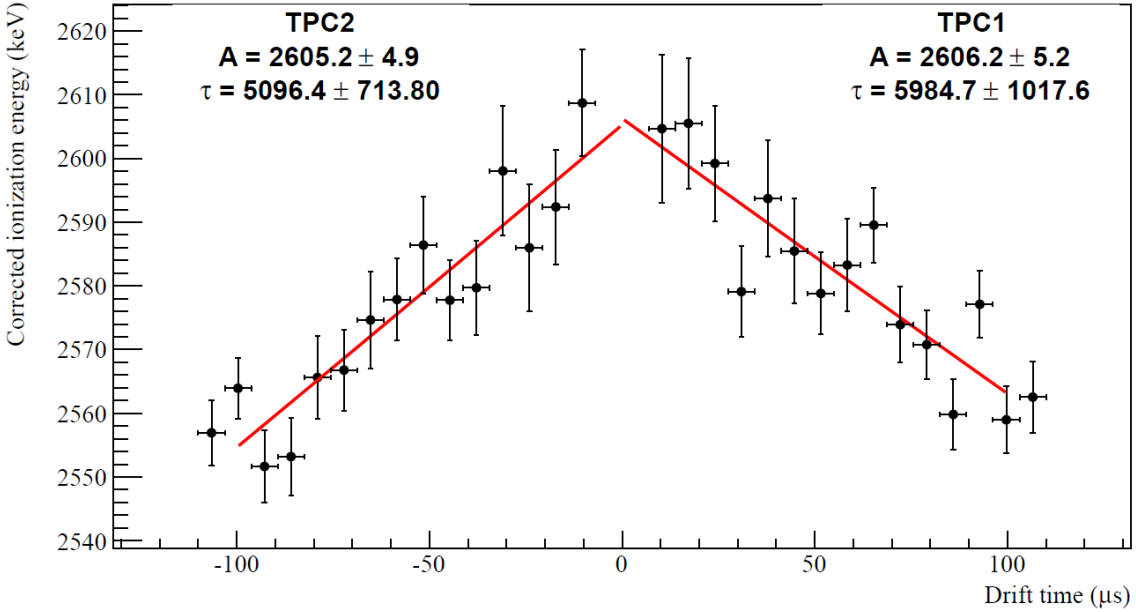


Figure 6.13: The purity charge correction is measured by fitting the 2615-keV ^{208}Tl gamma line as a function of Z-position. [71]

the xenon. As electrons drift, they may attach to electronegative impurities such as water, oxygen, and methane; the exact nature of the electronegative impurities in EXO-200 are not known. The level of impurities in the xenon are time-dependent due to the strong effects which the xenon pump speed and periodic xenon feeds may have.

To extract the purity correction, the dataset is divided into time windows when the pump speed was constant and no feeds occurred; the purity is assumed to be constant during these time intervals. It is then possible to combine all thorium source data during these time windows and fit for the 2615-keV single-site ^{208}Tl gamma line in Z-bins ranging from the North to the South anode. An illustration

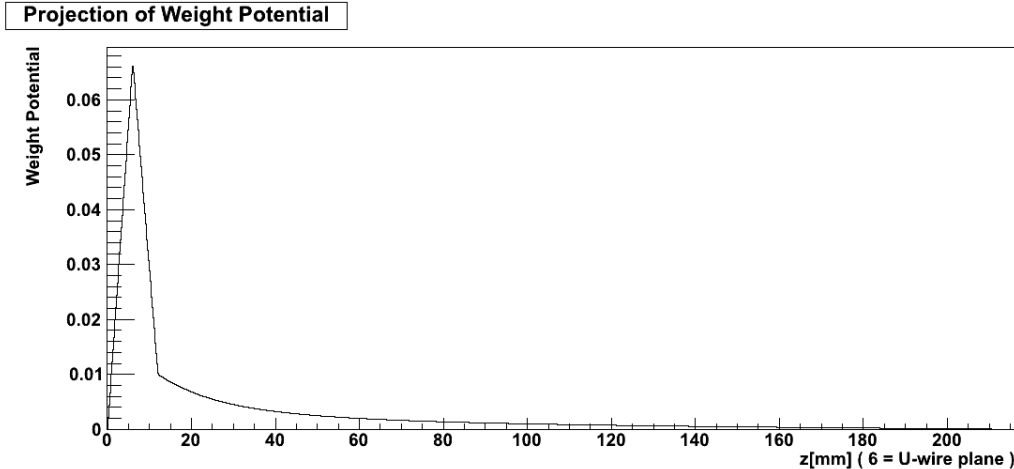


Figure 6.14: The expected grid correction of a u-wire as a function of Z-position. In this plot, $Z = 6$ mm represents the position of the u-wire plane and $Z = 12$ mm is the position of the v-wire plane. [48]

of the ionization peak position versus Z is shown in figure 6.13. Charge attenuation is exponential with a typical e -fold attenuation occurring in $4 - 5$ ms drift time; the purity correction to charge energy is typically $2 - 3\%$ for charge deposits at the cathode. [71]

The other Z -dependent charge correction is from the shielding grid. Section 2.5 described the process by which both electron clouds and ionized xenon will induce signals on the wires. The electron cloud drifts rapidly, and its pulse is observable; the ionized xenon will drift quite slowly, and will not produce an observable pulse in our electronics. However, the ionized xenon will counteract the induced current pulse from the drifting electrons by holding some electrons on the wire; the degree to which they are able to influence the observed current signal depends on the weight potential of the wire evaluated at the position of the xenon ions. The weight

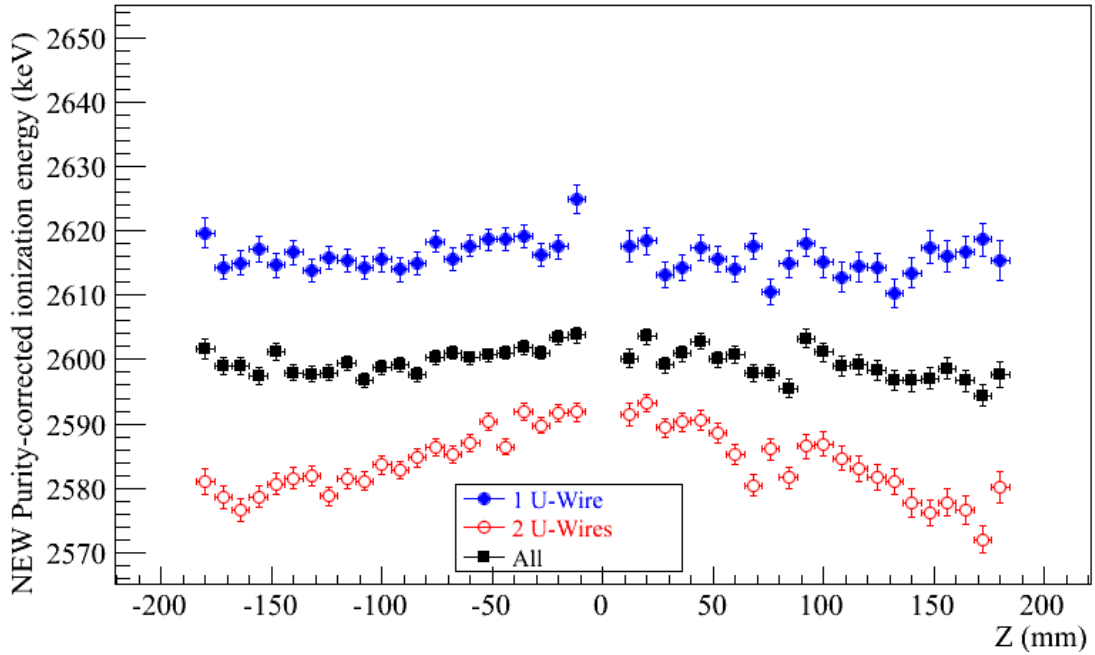


Figure 6.15: After applying all charge corrections, we find that the 2615-keV ^{208}Tl ionization peak is observed at the expected location for single-wire events; however, for two-wire events a residual bias is observed which also exhibits Z-dependence. [71]

potential of a u-wire is shown as a function of Z in figure 6.14, and we can see that inside the v-wire plane this correction is expected to remain below 1%. [48]

These are all of the known corrections to the charge energy. However, we find that after applying them, there remains a residual z-dependence in the charge calibration. Figure 6.15 shows that although the 2615-keV ^{208}Tl ionization peak has been properly corrected for clusters which deposit on only one u-wire, for clusters which are split between two u-wires there is a residual offset in peak position of roughly 1% and an additional z-dependent effect of up to roughly 0.3%. These effects are not presently understood; however, they are believed to induce a Z-

dependent bias effect in the lightmap which is used for scintillation denoising, which is believed to cause the scintillation z-bias described in section 6.3.2. [71]

6.3.2 Light Corrections

Although scintillation measurements are made from fitting the magnitudes of the scintillation pulses found in reconstruction, as described in section 6.2.2, these scintillation measurements are superceded by the denoised scintillation energies estimated using the denoising method of chapter 3. This subsection will describe evaluations of the success of that denoising effort and subsequent corrections made to the denoised scintillation energy.

When the denoising algorithm operates properly, it should be constrained to produce scintillation energy measurements calibrated in keV. This calibration is accomplished by the lightmap, which retains information about the magnitude of pulses produced by 2615-keV energy deposits. However, in practice it is seen that the denoised scintillation measurements are not properly calibrated; this can be seen in figure 6.16, where it is clear that events of all types (alpha decays in low-background data and both one-wire and two-wire single-site gamma decays from an external source) measure a scintillation energy which is systematically too low and displays significant Z-dependence. The thorium data, which provides more the best measurement statistics, shows a mis-calibration which ranges from 2.5% near the anodes to 6.5% at the cathode. [71]

The cause for the discrepancy in scintillation energy measurements is not cur-

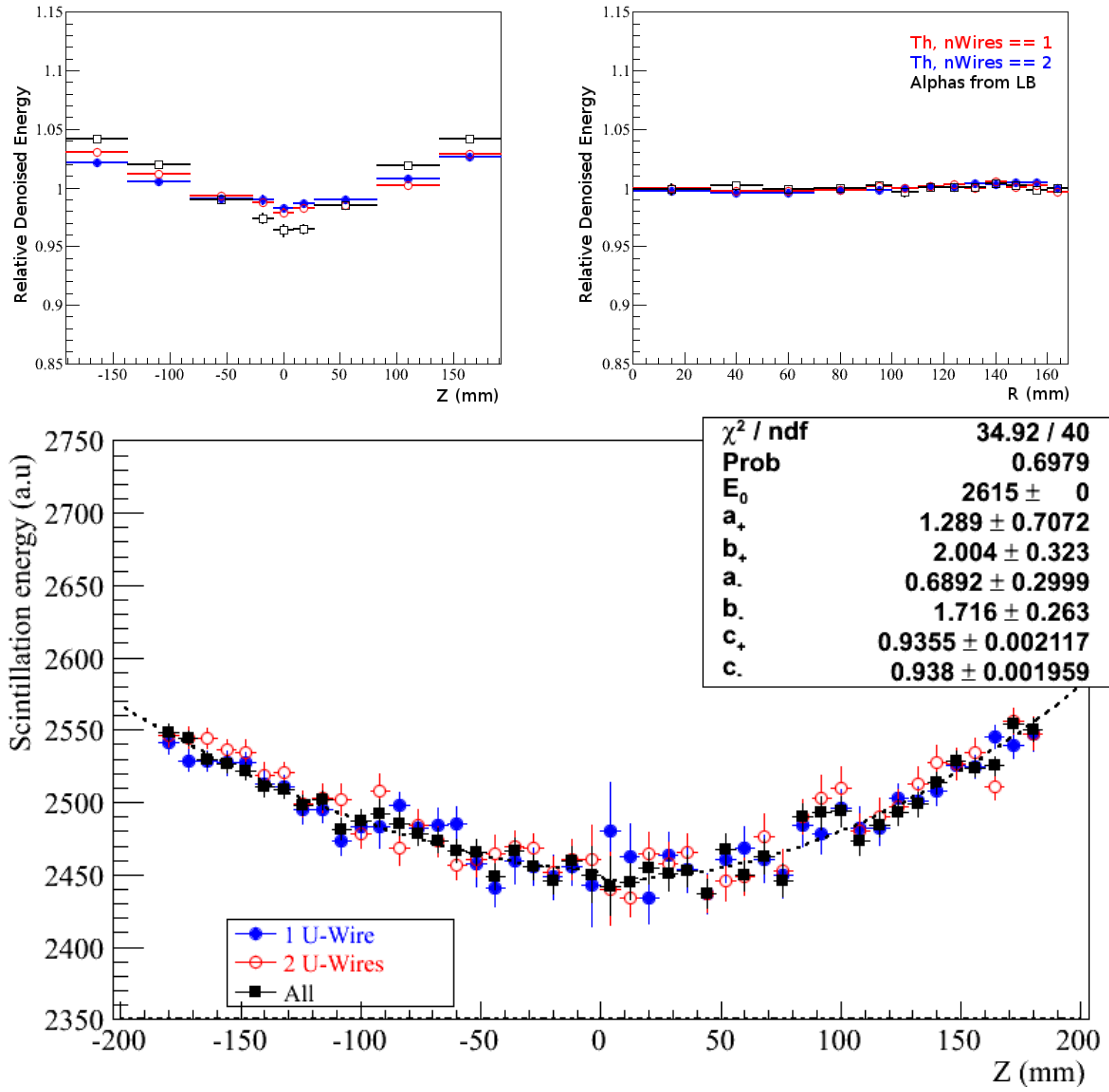


Figure 6.16: A residual calibration offset and Z-dependent behavior is observed in the denoised scintillation measurements. The top plots show the relative peak position of the scintillation-only 2615-keV ^{208}Tl peak (one-wire and two-wire) and average alpha energy from ^{222}Rn versus Z (top left) and R (top right). The bottom plot shows the absolute denoised scintillation energy from the 2615-keV ^{208}Tl peak for one and two wires, with the measured correction function overlaid. [71]

rently known. One hypothesis is that the discrepancy in two-wire charge cluster measurements described in section 6.3.1 may lead to inaccurate event selection in the generation of the lightmap described in section 5.2.1; poor event selection would lead to a systematic error in the lightmap which could depend on Z , and would be capable of creating the observed bias. Attempts to address this Z -bias within the generation of the lightmap or investigate alternative explanations for its origin have so far been unsuccessful, but these investigations continue, and it is hoped that this issue can be fixed for the next analysis.

In the meantime, for this analysis an empirical correction of the discrepancy is applied. The scintillation correction function takes the form:

$$E_{corr} = E_{meas} \cdot \begin{cases} [(c_-) + (a_-) \cdot |Z|^{b_-}]^{-1} & \text{if } Z < 0 \\ [(c_+) + (a_+) \cdot |Z|^{b_+}]^{-1} & \text{if } Z > 0, \end{cases} \quad (6.7)$$

where we measure from data $c_- = 0.9380$, $c_+ = 0.9355$, $b_- = 1.71$, $b_+ = 2.00$, $a_- = 0.69$, $a_+ = 1.3$, and Z is in units of meters. The bottom plot of figure 6.16 shows this empirical correction overlaid on one-wire and two-wire thorium source data, demonstrating the function agrees well with the observed Z -dependent offset. [71]

6.3.3 Rotated Energy Calibration

From the corrected scintillation and charge energy measurements, it is necessary to form a calibrated rotated energy measurement which combines them. This combination will take advantage of anticorrelation between charge and light to achieve an optimal energy resolution. To accomplish these measurements, it is necessary to use

multiple calibration points; we use the 2615-keV gamma line from regularly-taken thorium source runs to measure time-dependent calibration parameters, and the 1173-keV and 1332-keV gamma lines from cobalt source runs and 661-keV gamma line from cesium source runs to characterize the energy dependence of calibrations. The linear combination of scintillation and charge will be selected to optimize energy resolution; the precise measurement of energy resolution will be described in section 6.3.4, but for this purpose we will simply seek to make energy peaks as narrow as possible.

The calibrated rotated energy E is computed by a calibration function of the form:

$$E_{rot} = E_S \cdot \sin(\theta(t)) + E_C \cdot \cos(\theta(t)) \quad (6.8)$$

$$E_{ratio} = \frac{E_{rot}}{E_{rot}^{th}(t)} \quad (6.9)$$

$$E = (E_{thorium} - E_{bias}) \cdot (p_0 + p_1 E_{ratio} + p_2 E_{ratio}^2), \quad (6.10)$$

where E_C and E_S are the measured charge and scintillation energies (with corrections applied as described in sections 6.3.1 and 6.3.2), $\theta(t)$ is a time-dependent rotation angle measured to optimize the fractional energy resolution of the thorium gamma line, $E_{rot}^{th}(t)$ is the time-dependent location of the thorium peak in the spectrum of E_{rot} , $E_{thorium}$ is the true thorium peak position equal to 2615 keV, and E_{bias} , p_0 , p_1 , and p_2 are time-independent calibration parameters. Entirely separate calibration parameters are obtained for single-site and multi-site events.

The result of this calibration is shown in figure 6.17. We can see here that a projection is performed from the two-dimensional charge-light spectrum along an

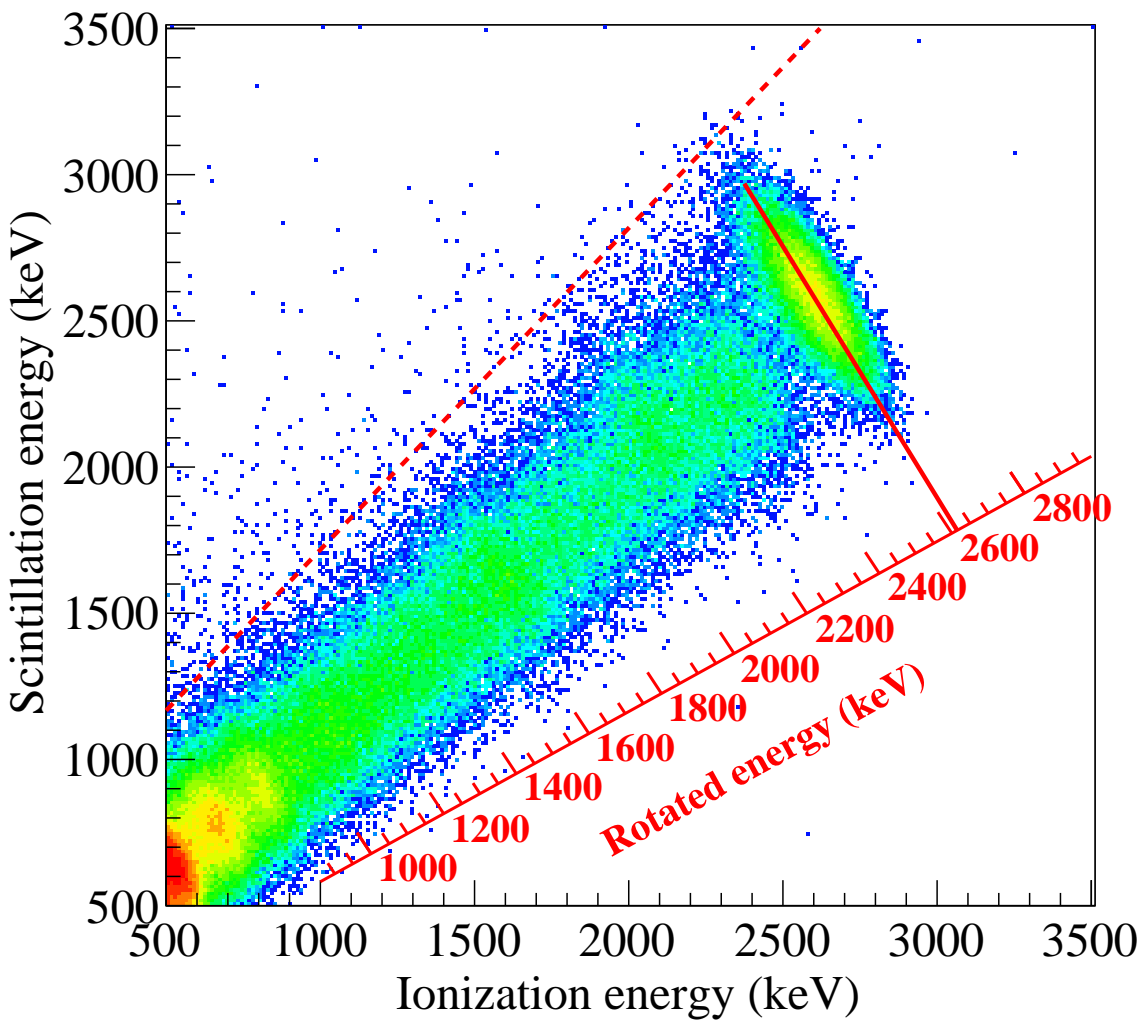


Figure 6.17: Corrected scintillation versus charge energy are shown for a thorium run. The projection angle for the rotated energy measurement is illustrated at the 2615-keV peak; the projection onto a calibrated axis is shown. Figure provided by Liangjian Wen.

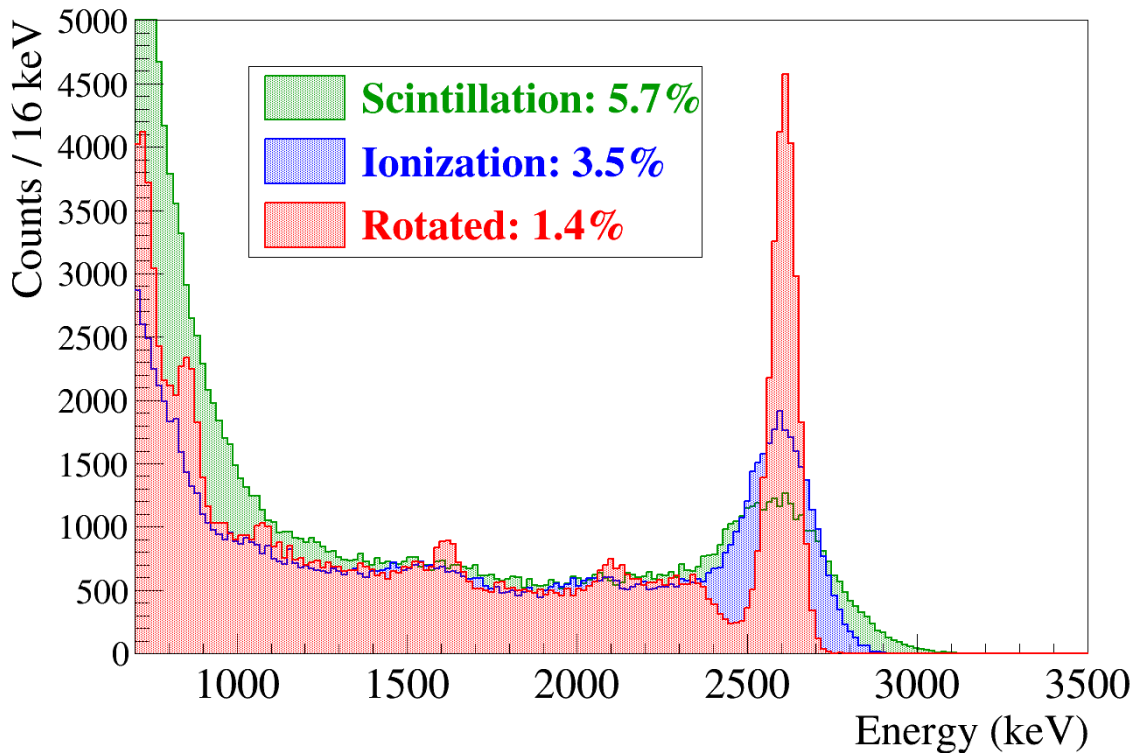


Figure 6.18: Charge-only, scintillation-only, and rotated energy spectra are shown from a thorium source run; the significant improvement in energy resolution with the rotated energy measurement is apparent, as are low-energy features which are washed out in the lower-resolution spectra. The dotted red line indicates the diagonal cut described in section 6.4. Figure provided by Liangjian Wen.

axis that minimizes the width of the thorium gamma line. Figure 6.18 demonstrates the spectra we obtain from projections only in scintillation, only in ionization, and using the optimal linear combination we have described; the improvement in resolution from using an appropriate linear combination of scintillation and ionization is apparent, as the peak at 2615 keV becomes sharper and additional low-energy features of the spectrum become apparent which were washed out with worse resolution. The next section will describe the process of measuring the energy resolution.

6.3.4 Measurement of Rotated Energy Resolution

Along with the energy calibration, we must also measure the energy resolution of the rotated spectrum. The resolution is assumed to be energy-dependent; if a monoenergetic deposit is made in the liquid xenon, we hypothesize that the observed spectrum should be gaussian and define the energy resolution at that energy to be the value of σ . We can parametrize the dependence of σ on energy as:

$$\sigma(E) = \sqrt{p_0^2 E + p_1^2 + p_2^2 E^2}, \quad (6.11)$$

where typically we interpret the parameters p_1 to come from electronic noise (which contributes a smearing independent of energy), p_0 to come from statistical fluctuations in the number of photons or electrons observed (which follows a Poisson distribution), and p_2 to come from mis-calibration of components of the detector (whose effect does not diminish with increased energy). [72] We also often find it useful to refer to the relative or fractional energy resolution, defined as:

$$\sigma(E)/E = \sqrt{p_0^2/E + p_1^2/E^2 + p_2^2}. \quad (6.12)$$

Parameter	Undenoised		Denoised	
	SS	MS	SS	MS
p_0	0	0	0.628	0.602
p_1	39.8	43.0	20.8	25.8
p_2	0.0107	0.0096	0.0011	0.0040

Table 6.1: Time-averaged resolution parameters for denoised and undenoised data.

For undenoised data, measurements were consistent with $p_0 = 0$, so this parameter was not used in the analysis of undenoised data. [73]

The resolutions of single-site and multi-site events differ, so there are separate resolution functions measured for both classes of events.

The resolution functions are measured from the same set of calibration gamma lines (at 661, 1173, 1332, and 2615 keV) that are used for the energy calibration. The resolution parameters are time-dependent; average resolution parameters are computed by weighting the resolutions observed in different time windows by the fraction of EXO-200 low-background data taken within that window. The resulting resolution parameters are listed in table 6.1. Figure 6.19 compares the denoised and undenoised resolution functions. The strongest effect is the reduction of p_1 by roughly a factor of two in the denoised data, consistent with the interpretation that denoising improves the energy resolution primarily by reducing the impact of electronic noise.

We note that p_0 shifts from negligible to measurable when denoising is applied. It is suggestive to interpret this as meaning denoising increases noise due to

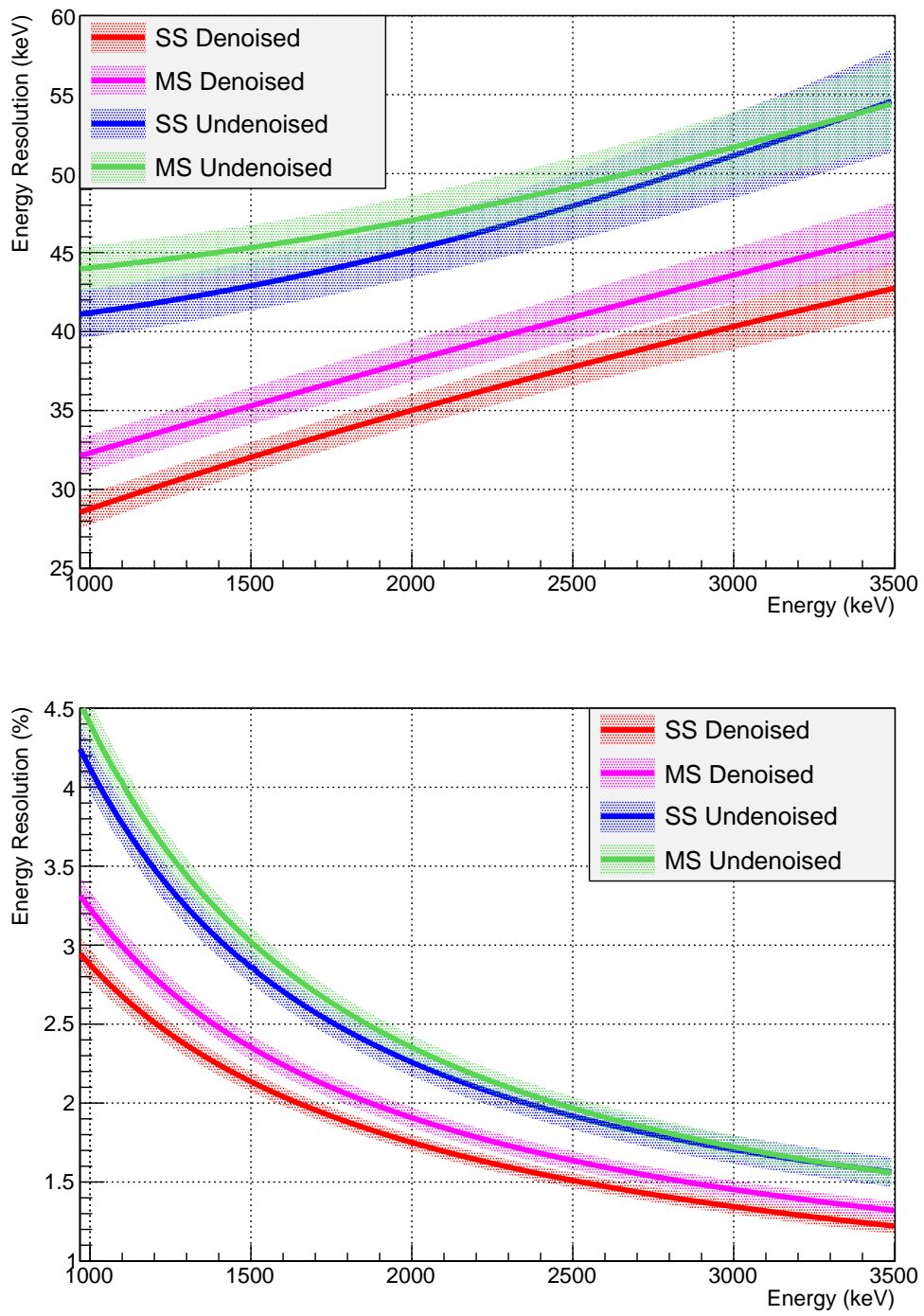


Figure 6.19: The resolution functions (top) and relative resolution functions (bottom) are compared for denoised and undenoised data.

statistical fluctuations in the number of collected photons. The undenoised scintillation measurements are made from summed waveforms, so it uses the full photon statistics of all channels; as a result, we can expect that p_0 is as small as possible in the undenoised data. By contrast, denoising may choose to concentrate its scintillation measurement on a smaller number of channels, reducing electronic noise at a cost in greater statistical fluctuations. Furthermore, we recall in section 3.8 that the current analysis mistakenly underestimates Poissonian noise produced inside the APDs, and this would manifest itself by subjecting the scintillation estimate to even more statistical fluctuations than would be ideal. It is therefore possible that the increase in p_0 may demonstrate denoising has sacrificed photon collection efficiency for the purpose of reducing electronic noise.

The parameter p_2 seems to be significantly reduced by denoising. This can be interpreted as demonstrating a better understanding of APD gain in denoised scintillation measurements. In the undenoised scintillation measurements, all APD channels are summed together without regard to the different gains of each APD channel; we can expect this to lead to a significant variation in gain depending on which APD channel was nearest to an energy deposit, which would appear as a significant contribution to p_2 . On the other hand, the denoised scintillation measurement is build around a channel-by-channel APD lightmap which contains information about the gain of every APD channel, which could reduce the impact of local variations in gain and, consequently, the magnitude of p_2 .

It should be noted that, although these interpretations of p_0 , p_1 , and p_2 are highly suggestive, the naive interpretations of their meaning may not be fully ap-

plicable to the rotated energy measurements. Other energy-dependent quantities may not be fully understood; for example, it has been suggested that the rotation angle may be energy-dependent, and our failure to include this dependence may be reflected by an energy dependence in the resolution function. [48] Also, the error bands in figure 6.19 are still somewhat broad, and more accurate resolution measurements or resolution measurements from a wider energy range would be useful to constrain the values of these parameters better. Further investigation will be required to verify that the scintillation energy measurement accuracy is still the dominant contributor to energy resolution at all energy scales.

Although we have identified the energy resolution functions averaged over our entire dataset, it is also instructive to study the time-dependence of the energy resolution. We cannot produce a full resolution function which is time-dependent because the cesium and cobalt source calibrations were only occasionally taken, but it is possible to study the time dependence of the resolution at the 2615-keV ^{208}Tl line of the thorium source which was deployed much more frequently. This resolution is shown as a function of time in figure 6.20. We can see that the energy resolution is improved for all time periods. We can also see that the variations in resolution are much smaller in denoised than undenoised energy; in particular, the period of worse resolution between October 2012 and June 2013 is brought closer to the resolution during the rest of the data run by the denoising process. Time fluctuations in the undenoised energy resolution are attributed to fluctuations in the electronic noise on the APDs, and this flattening-out of the resolution's time dependence after denoising shows that denoising is capable of removing the impact

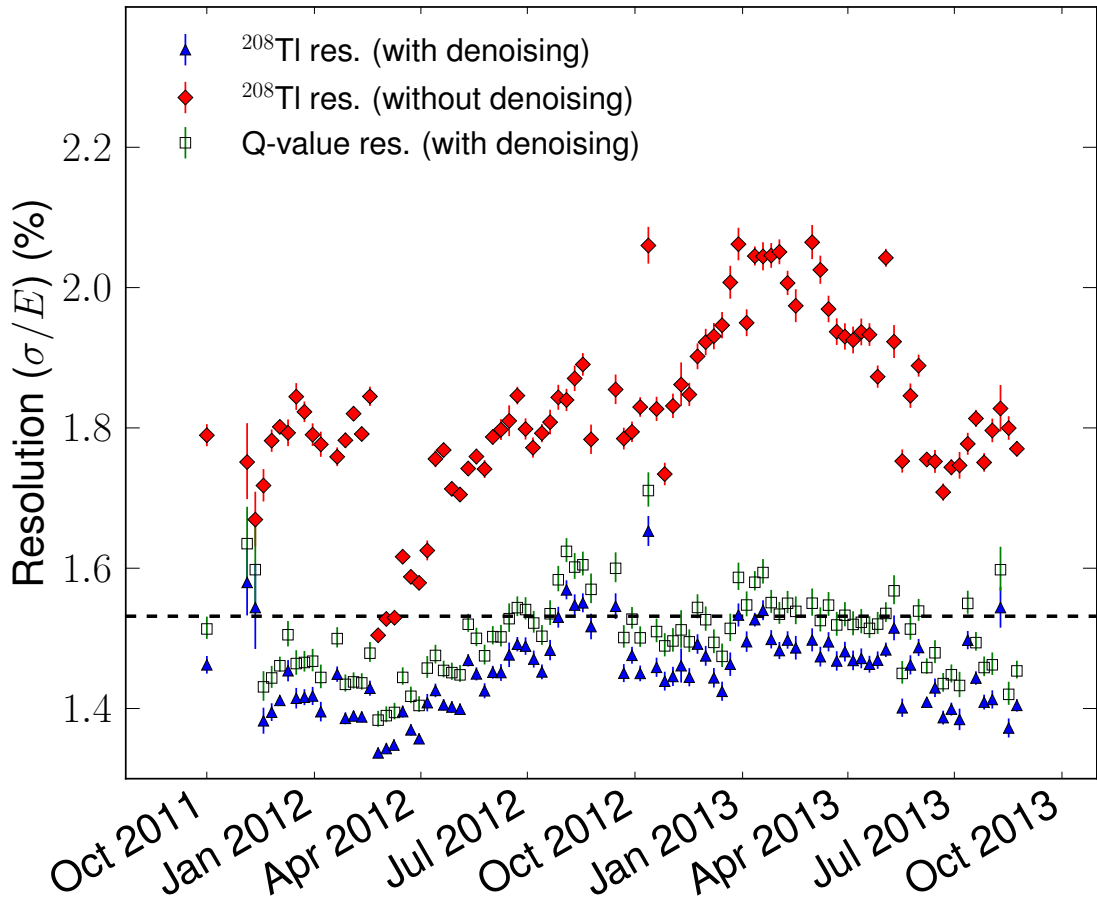


Figure 6.20: Time dependence of the single-site energy resolution at 2615 keV with denoised (blue) and undenoised (red) scintillation. The denoised energy resolution at the $\beta\beta0\nu$ Q -value is estimated (open square) from the time-dependent energy resolution measured with thorium data combined with the time-independent shape of the average resolution function. [35]

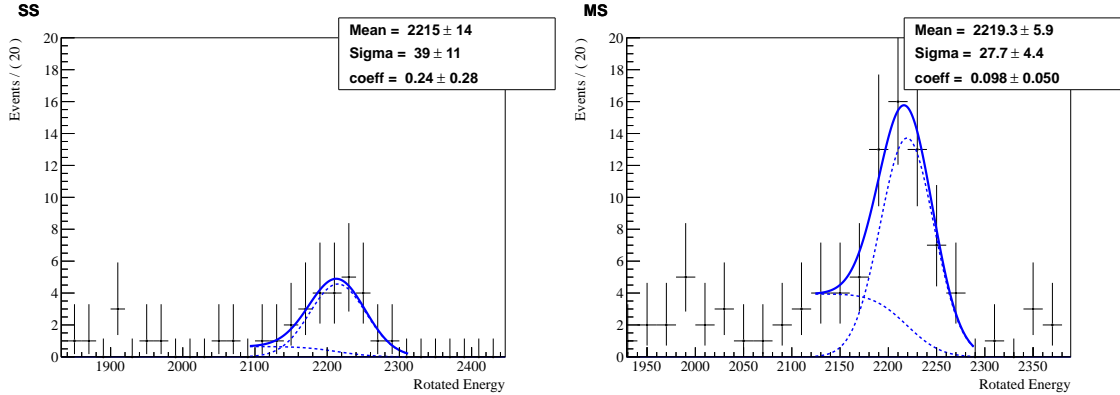


Figure 6.21: The single-site (left) and multi-site (right) gamma line at 2.2 MeV from neutron capture on hydrogen can be used as a low-background cross-check on the resolution calibration. [71]

of this time-varying noise. [35]

Besides the energy resolution measurements from source data described above, it is possible to identify gamma lines in the low-background data. These are currently used as a cross-check on the source calibrations rather than additional input into the calibration procedure. They can serve the additional purpose of verifying that calibrations from a wide range of times can be combined to produce coherent peaks; they can also verify that the average resolutions extracted from source data are accurate because low-background sources are inherently averaged over the duration of the data run. Two energy lines from the low-background spectrum have been identified as particularly useful.

One gamma line in the low-background data comes from neutron capture on hydrogen in the HFE refrigerant. Such events are generally vetoed by the coincidence cuts, primarily the veto panels, so their impact on the low-background data

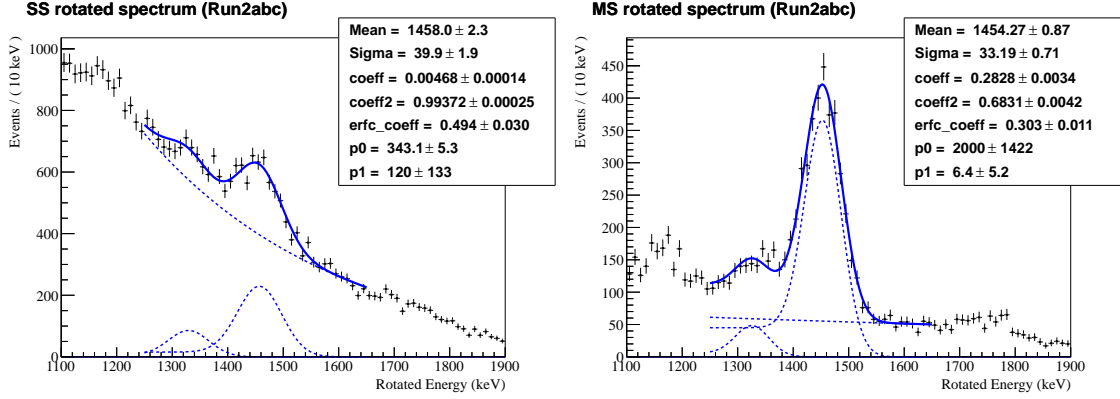


Figure 6.22: The low-background potassium peak at 1461 keV is used as a cross-check on the single-site (left) and multi-site (right) energy calibrations. Fits also include the nearby 1332-keV cobalt peak. [71]

is suppressed; conversely, it is possible to study only events which occur in coincidence with muon detection by the veto panels, thereby enriching our dataset in neutron capture spectra. Neutron capture on hydrogen can emit a 2.2 MeV gamma; figure 6.21 shows the spectra from this source. [39, 71]

The other gamma line which has been used as a cross-check is the 1461-keV ^{40}K gamma line. ^{40}K is expected to occur in the copper of the TPC at some low level, and this gamma line is readily visible in the multi-site spectrum of low-background data. The improved energy resolution of denoised data allows us to also identify the ^{40}K single-site peak over the $\beta\beta2\nu$ background, which was not previously possible. These peaks are shown in figure 6.22.

6.4 Fitting

After the energy calibrations have been performed, it is possible to produce a set of data with calibrated energy measurements. We will now describe the selection of usable events from this dataset, the creation of corresponding background probability distribution functions (PDFs), the fitting of data to extract the best-fit number of $\beta\beta0\nu$ events in the dataset, and the association of errors with that number. Results from the current analysis will be demonstrated along the way, leading to a limit for $\beta\beta0\nu$ decay.

It is necessary to perform a number of cuts on the dataset before it is usable. These cuts are intended to reject events which may not agree with the model used to generate background PDFs. These cuts include: [74]

- A fiducial volume cut to remove events with any energy deposits outside of a pre-defined volume. We choose to define a fiducial volume defined in Z by $10\text{mm} < |Z| < 182\text{mm}$ and in the X-Y plane as the area within a hexagon with an apothem of 162 mm, as illustrated in figure 6.23. These cuts allow us to ignore regions near the detector walls or v-wire plane where the electric fields may not behave as expected. They also ensure that beta or alpha backgrounds from the walls of the detector do not penetrate into our fiducial volume, allowing us to simplify the set of backgrounds modeled and included in fits.
- A “diagonal” cut to remove events with excessive scintillation relative to ion-

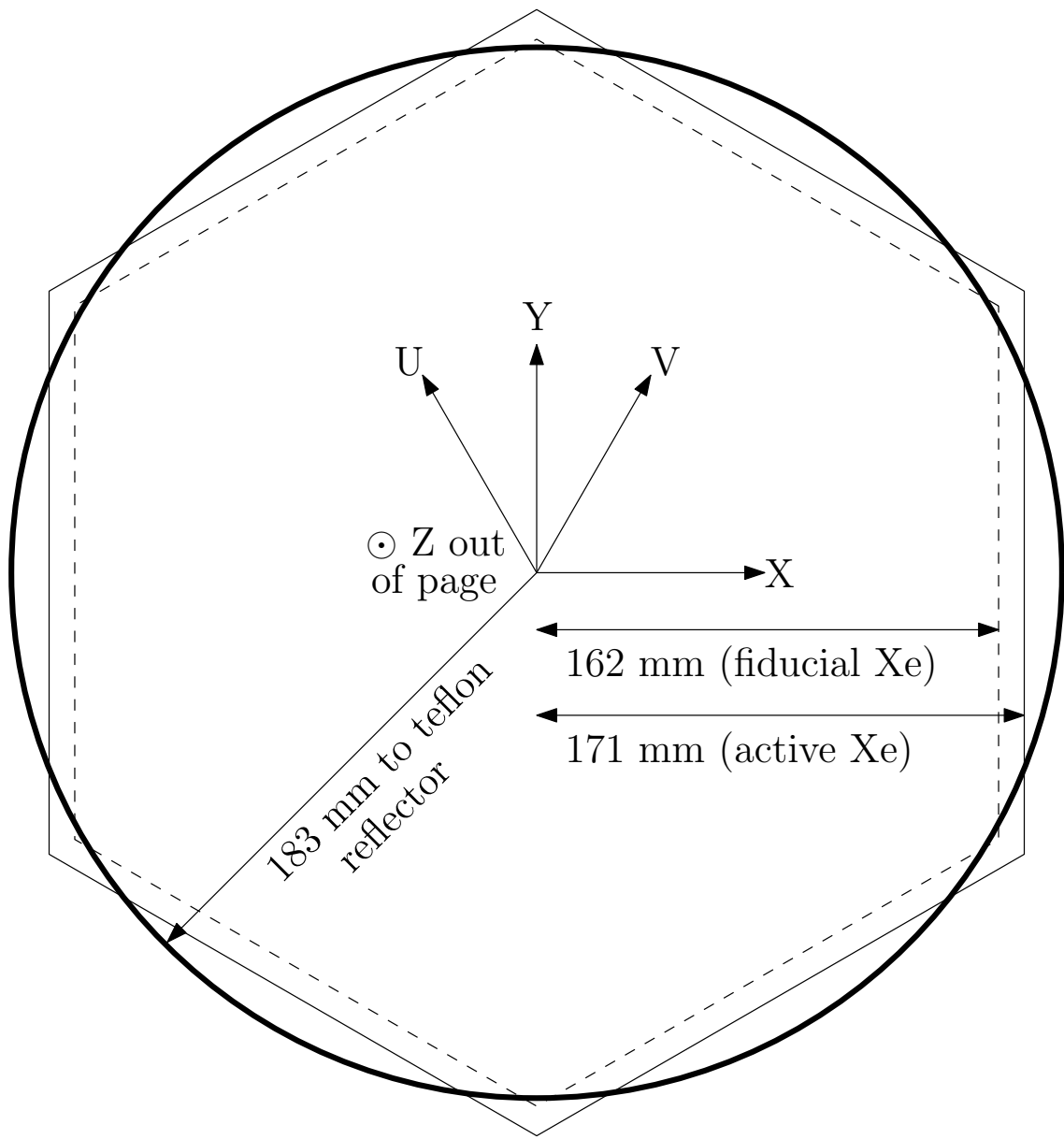


Figure 6.23: The X-Y fiducial cuts applied to the data do not include the entire active volume; however, for the $\beta\beta0\nu$ search we find that aggressive fiducial cuts optimize our sensitivity.

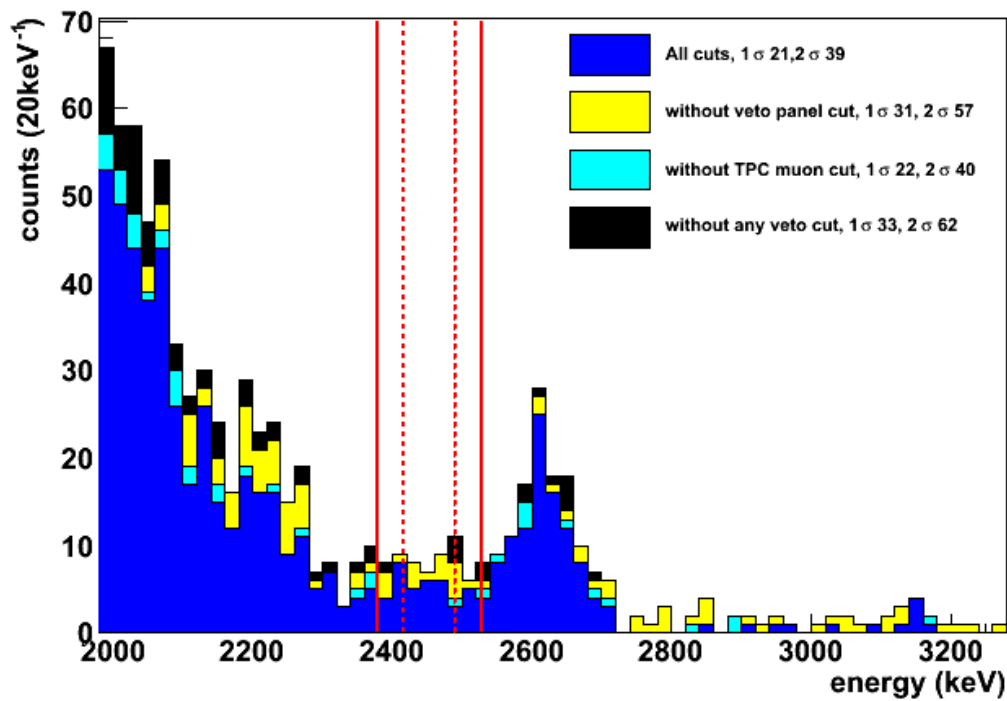


Figure 6.24: Vetoing events coincident with muons can reduce our 1σ and 2σ event counts. Figure provided by David Auty.

ization. Alpha decays produce a light-to-charge ratio much higher than beta and gamma decays, as described in section 2.4, so excluding events with excessive light permits us to neglect alpha-decay backgrounds dissolved in the xenon. Events with excessive light can also be caused by decays outside of our active xenon, where charge is not collected efficiently; these events will be difficult to calibrate, and should not be included. Both are excluded by a cut on the light-to-charge ratio, as shown in figure 6.17.

- A coincidence cut to remove events occurring near in time to a passing muon.

Muons and their spallation products can produce a wide range of backgrounds which is difficult to model; most of these backgrounds are quite short-lived, so a coincidence cut can provide an effective means of reducing them. Currently we cut all events occurring within one minute of a muon observed passing directly through the TPC and within 25 ms after a muon observed passing through the veto panels. Furthermore, events which occur within one second of each other are both cut based on the expectation that the events were probably correlated and therefore more likely to be some form of background. Figure 6.24 demonstrates the significant reduction in data rate which is achieved by applying this coincidence cut.

Fits are then performed using the profile-likelihood method, as described in [75]. Each data point is assigned a likelihood $\text{pdf}(x)$ equal to the evaluation of the normalized pdf at that point; the test statistic of interest is the negative

log-likelihood, defined by:

$$\text{NLL} = - \sum_i \ln [\text{pdf}(x_i)] + \text{constraints.} \quad (6.13)$$

Constraints for us will consist of gaussian penalty terms applied to parameters whose value is constrained by independent studies external to the fit. The best fit will be the one which minimizes the NLL. Fit errors on parameters can be extracted by observing how the NLL changes when those parameters are forced away from their best-fit values. In cases where the best-fit value of a parameter is near its boundary, these errors may not provide a good estimate of the true confidence interval or limits, so when this situation occurs for a parameter of significant interest (specifically, the rate of $\beta\beta0\nu$, which fits near to zero) we can verify that the confidence limit is not overstated using toy monte carlo studies. [74]

The fits make use of three observables. The first, event energy, has been discussed at length in section 6.3.3. The second is the event classification as single-site or multi-site; we define an event as single-site if reconstruction located only one cluster, and that cluster deposited charge on no more than two u-wire channels. [74]

The third observable is called standoff, and it attempts to capture the nearness of an event to the TPC walls. Most backgrounds are external, and can be expected to deposit energy preferentially near the walls of the TPC; by contrast, $\beta\beta0\nu$ and $\beta\beta2\nu$ decay come from the xenon, and should be distributed uniformly through the detector. We define the standoff distance to be the shortest distance between some deposit cluster and either the v-wire planes or the teflon walls. Ideally, it would be possible to capture finer position information by using all three

position coordinates as observables; however, in practice it is difficult to construct a pdf with sufficient statistics in so many dimensions, so the standoff observable has been constructed to capture the most interesting distances in a single observable. The exact definition is not too important provided it is modeled properly by the simulation; figure 6.9 demonstrates that standoff distance is simulated well for all but the smallest values (closest to the TPC walls or anode), and this is accounted for as a shape systematic. [74]

Fit parameters include the number of counts observed from each pdf and the fraction of counts from each pdf which populate the single-site spectrum; the latter is constrained based on the agreement between simulated and observed single-site fraction from source runs, but is allowed to float within those uncertainties. The pdfs which are included are:

- ^{136}Xe $\beta\beta2\nu$ decay.
- ^{136}Xe $\beta\beta0\nu$ decay.
- ^{232}Th from the TPC vessel.
- ^{232}Th from distant sources (HFE refrigerant or cryostat).
- ^{238}U from the TPC vessel.
- ^{214}Bi from the TPC cathode (^{238}U chain).
- ^{214}Bi from the air gap inside the lead wall (^{238}U chain).
- ^{214}Pb dissolved in active xenon (^{238}U chain).

- ^{222}Rn dissolved in inactive xenon (^{238}U chain).
- ^{60}Co from the TPC vessel.
- ^{40}K from the TPC vessel.
- ^{65}Zn from the TPC vessel.
- ^{54}Mn from the TPC vessel.
- ^{137}Xe from neutron capture on ^{136}Xe .
- ^{135}Xe from neutron capture on ^{134}Xe .
- Various neutron captures on xenon, copper, and hydrogen.

Similar pdfs from different locations are included because the sharpness and relative intensity of peaks can be affected by intervening material. The rate of ^{214}Bi from the air gap is constrained by measurements of radon levels in air, and the rates of ^{214}Bi from the TPC cathode, ^{214}Pb dissolved in active xenon, and ^{222}Rn dissolved in inactive xenon are jointly constrained by independent searches for ^{214}Bi - ^{214}Po rates. The overall rate of neutron captures is allowed to float, but the relative intensities of the captures on xenon, copper, and hydrogen are constrained by simulation, and the single-site fraction is fixed because there are not expected to be sufficient statistics in the single-site spectrum to constrain it. [74]

In addition to the magnitude and single-site fraction parameters of the fit, there are a few global parameters which are also allowed to float. There is a normalization constant which is allowed to float within constraints and accounts for

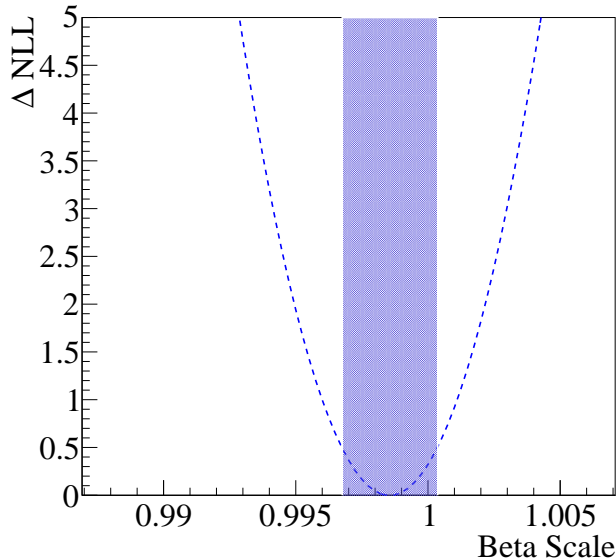


Figure 6.25: The fit provides constraints on the beta-scale. Figure provided by Liangjian Wen.

uncertainty in the fiducial volume or detection efficiency. Constraints on this term come from comparisons between the predicted and observed event rate from sources. Denoising does not currently operate on events whose waveforms are shorter than the standard length of $2048\mu\text{s}$; since these occur more in source data than low-background data, an additional correction to the simulated event rate must be generated, and denoising may in this way worsen the event rate agreement in source data even though it is not expected to show a significant effect in low-background data. Additionally, the normalization constants for gamma and beta particles are allowed to float separately because their reconstruction efficiency may be different.

Furthermore, it is expected that betas and gammas may need to be calibrated separately. To a first approximation, gammas deposit energy in the detector by exciting electrons, so these processes should be quite similar. However, to account

for possible differences, we define a beta-scale β which quantifies a linear calibration offset between beta and gamma deposits:

$$E_\beta = \beta E_\gamma. \quad (6.14)$$

The beta scale is permitted to float, and is constrained by the fit; figure 6.25 shows the NLL profile with various choices of beta scale, and demonstrates that it is possible to constrain the beta scale to a value close to 1 using only the spectral information in the fit. Uncertainty on the beta scale is incorporated by permitting it to float freely. We note that currently the beta scale is implemented by shifting beta-like pdf components ($\beta\beta0\nu$, $\beta\beta2\nu$, ^{135}Xe , ^{137}Xe) relative to the other components which are gamma-like; this ignores the detail that some events may contain clusters generated through both beta and gamma interactions, such as pair production from energetic gammas. These issues will be addressed in a future analysis, but for now the beta scale is assigned only to decays whose primary particle is a beta. [74]

When all of this is done, it is possible to obtain a fit to the low-background spectrum; the maximum-likelihood fit is shown in figure 6.26. The best-fit expected background in the 2σ single-site energy window around our Q -value is $31.1 \pm 1.8(\text{stat}) \pm 3.3(\text{sys})$ counts, corresponding to a background rate of $(1.7 \pm 0.2) \cdot 10^{-3} \text{keV}^{-1} \text{kg}^{-1} \text{yr}^{-1}$. The backgrounds in this 2σ energy window come from the thorium decay chain (51%), uranium decay chain (26%), and ^{137}Xe (23%), with other contributions negligible. The observed event count in the 2σ single-site energy window is 39 counts. [35]

(We remind the reader at this point that the quoted limit on $\beta\beta0\nu$ is not

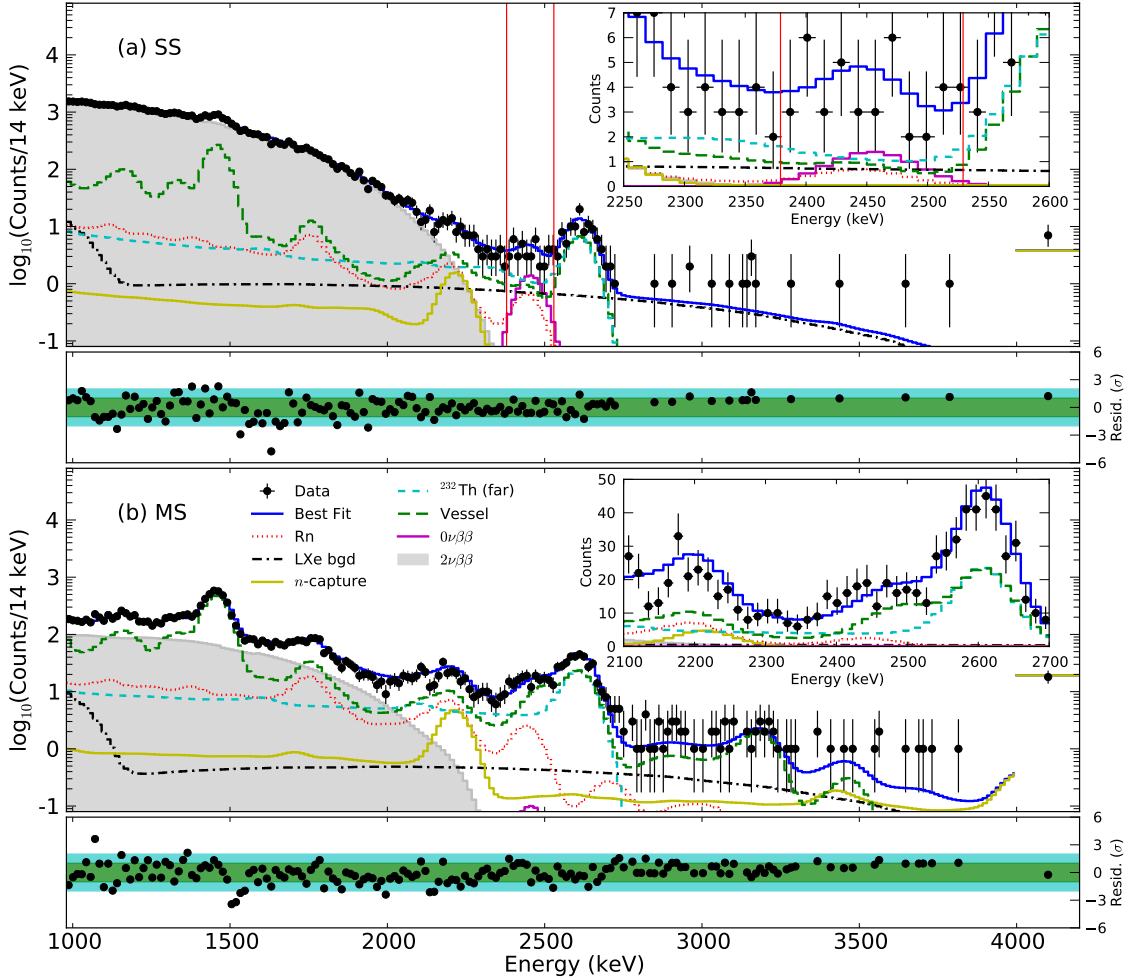


Figure 6.26: Energy spectra with best-fit pdfs for single-site (top) and multi-site (bottom). Residuals between data and the combined pdfs are shown below the spectra. The last bin of the spectra is an overflow bin. The 2σ region of interest around the Q -value is shown on the single-site spectrum. Insets for single-site and multi-site zoom around the Q -value. The simultaneous standoff-distance fit is not shown. [35]

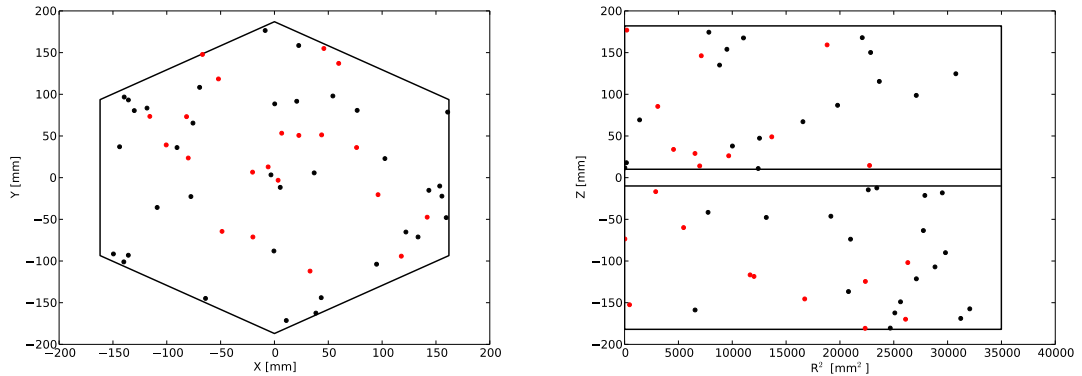


Figure 6.27: The positions of events in the 1σ region of interest (red) and wider energy range $2325 - 2550$ keV (black) are shown projected onto their X-Y (left) and R^2 -Z (right) coordinates. Lines indicate the fiducial volume, with the dotted lines indicating the fiducial cut away from the cathod that is not used as a component to the standoff distance observable. Figure provided by Dave Moore.

simply based on this comparison of counts, but based on the full set of energy and standoff-distance spectral information. Representative position information can be seen in figure 6.27. However, the simple comparison of counts can be instructive as an easier-to-understand approximation to the following limits.)

The likelihood profile for the total number of $\beta\beta0\nu$ counts occurring in our detector during the lifetime of the experiment is shown in figure 6.28. Based on the profile, we can see that a 1σ confidence interval for this parameter would exclude the null hypothesis of zero $\beta\beta0\nu$ counts; however, only 1σ exclusion of the null hypothesis is far too weak to make an inference of a non-zero signal. Instead, we follow the conventions of the field and quote a 90%-confidence upper limit of 24 total counts from $\beta\beta0\nu$. This corresponds to a 90%-confidence lower limit on the halflife of ^{136}Xe decay by the $\beta\beta0\nu$ mode of $1.1 \cdot 10^{25}$ years. [35]

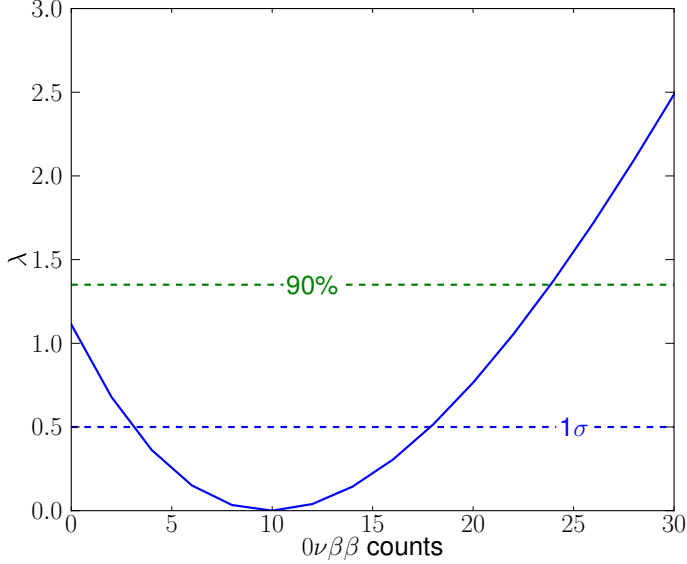


Figure 6.28: Profile scan of negative log-likelihood as a function of the number of fit $\beta\beta0\nu$ counts. [35]

6.5 Results and Physics Reach

We have stated the half-life limit on $\beta\beta0\nu$ decay of ^{136}Xe , which is the main result of the present analysis. We shall now continue to put this result in context with the expected sensitivity of the experiment and compare it to the limits and sensitivities achieved by other leading $\beta\beta0\nu$ experiments.

To place the limit derived with the current dataset in context with the overall strength of the experiment, we generate a number of toy monte carlo datasets. We assume that our best-fit backgrounds are fully accurate and that the null hypothesis (no $\beta\beta0\nu$) is true; we then use this best-fit background as our pdf and generate toy datasets. These can be used to study the “typical” results our detector would have produced if the same experiment could be repeated many times.

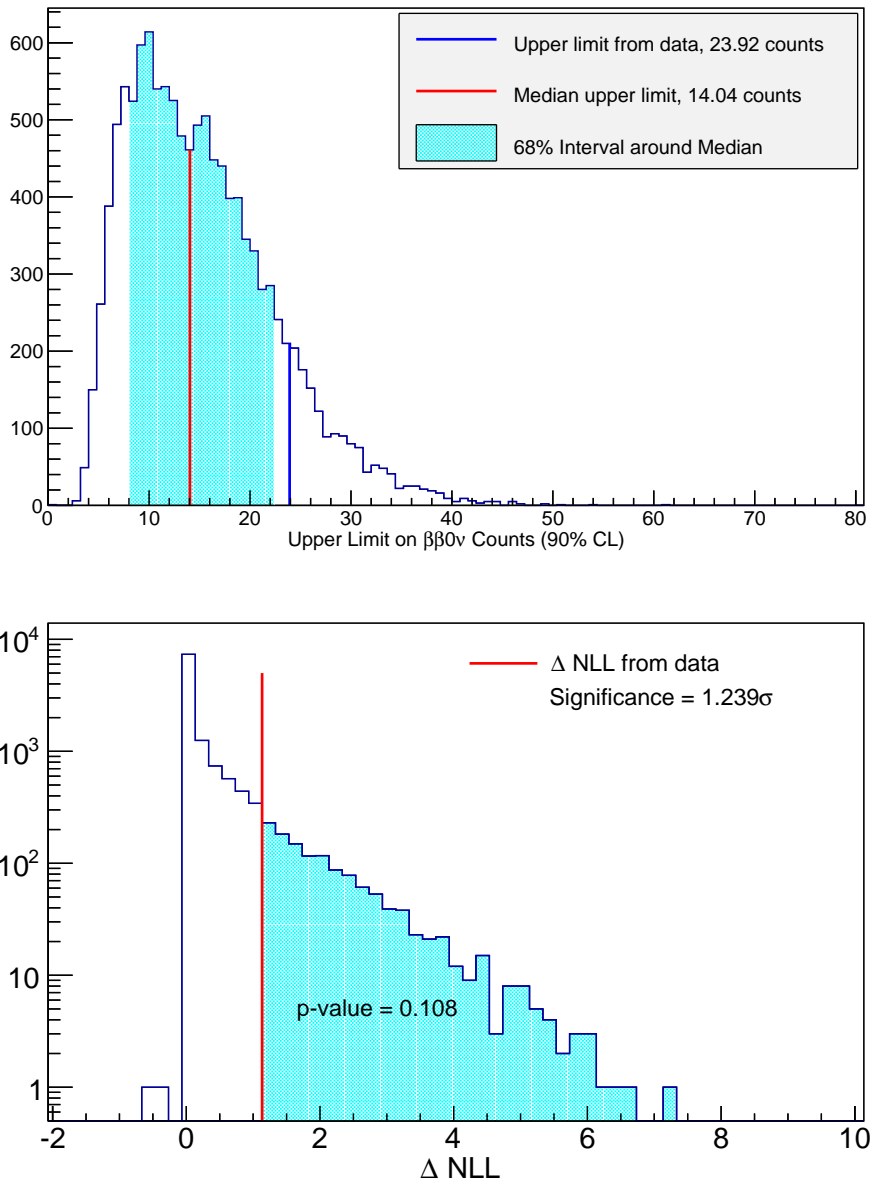


Figure 6.29: Assuming that the background measurements of EXO-200 from this analysis are accurate, toy datasets are simulated. The top plot shows the probability distribution of our 90% confidence limit; we find that our median upper limit is 14.04 counts attributed to $\beta\beta0\nu$, compared to our observed upper limit of 23.92 counts. The bottom plot shows the probability distribution of our ability to reject the null hypothesis (no $\beta\beta0\nu$) based on the negative log-likelihood; we find that the present dataset rejects the null hypothesis with probability less than 90%. Figures provided by Ryan Killick.

The resulting distributions are shown in figure 6.29. The top plot shows the distribution of 90%-confidence upper limits on the number of $\beta\beta0\nu$ counts; we can see that typical datasets from the EXO-200 experiment result in limits ranging from 8 to 22 counts. The median limit, is 14 counts; this value is called the median sensitivity, and it illustrates the overall strength of an experiment. We contrast this with the observed limit of 24 counts; as is apparent from the distribution, this limit is consistent with an unlucky upward fluctuation in the backgrounds observed by EXO-200.

We saw in the NLL profile on the total number of $\beta\beta0\nu$ counts in figure 6.28 that the NLL for the hypothesis of no $\beta\beta0\nu$ counts is about 1.1 higher than for the best fit; this quantity reflects how well we can reject the null hypothesis in favor of the best fit. To put this in context, we also observe the distribution of this value from toy monte carlo datasets in the bottom plot of figure 6.29. Here, we see that 10.8% of identical experiments will yield an NLL profile which is at least 1.1 worse for no $\beta\beta0\nu$ than for the best fits even though no $\beta\beta0\nu$ is simulated. We can conclude that this difference in NLL is not strong enough to reject the null hypothesis with high confidence.

The wide spread of limits produced in toy monte carlo studies illustrates the significant role that luck plays in the limits set by low-statistics experiments such as EXO-200. To compare EXO-200 to other experiments, it is useful to compare both the limits and the median sensitivities (median 90%-confidence limits). This is done in figure 6.30. Vertical lines correspond to the reported median sensitivities of the two leading ^{136}Xe experiments, KamLAND-Zen and EXO-200; right-pointing

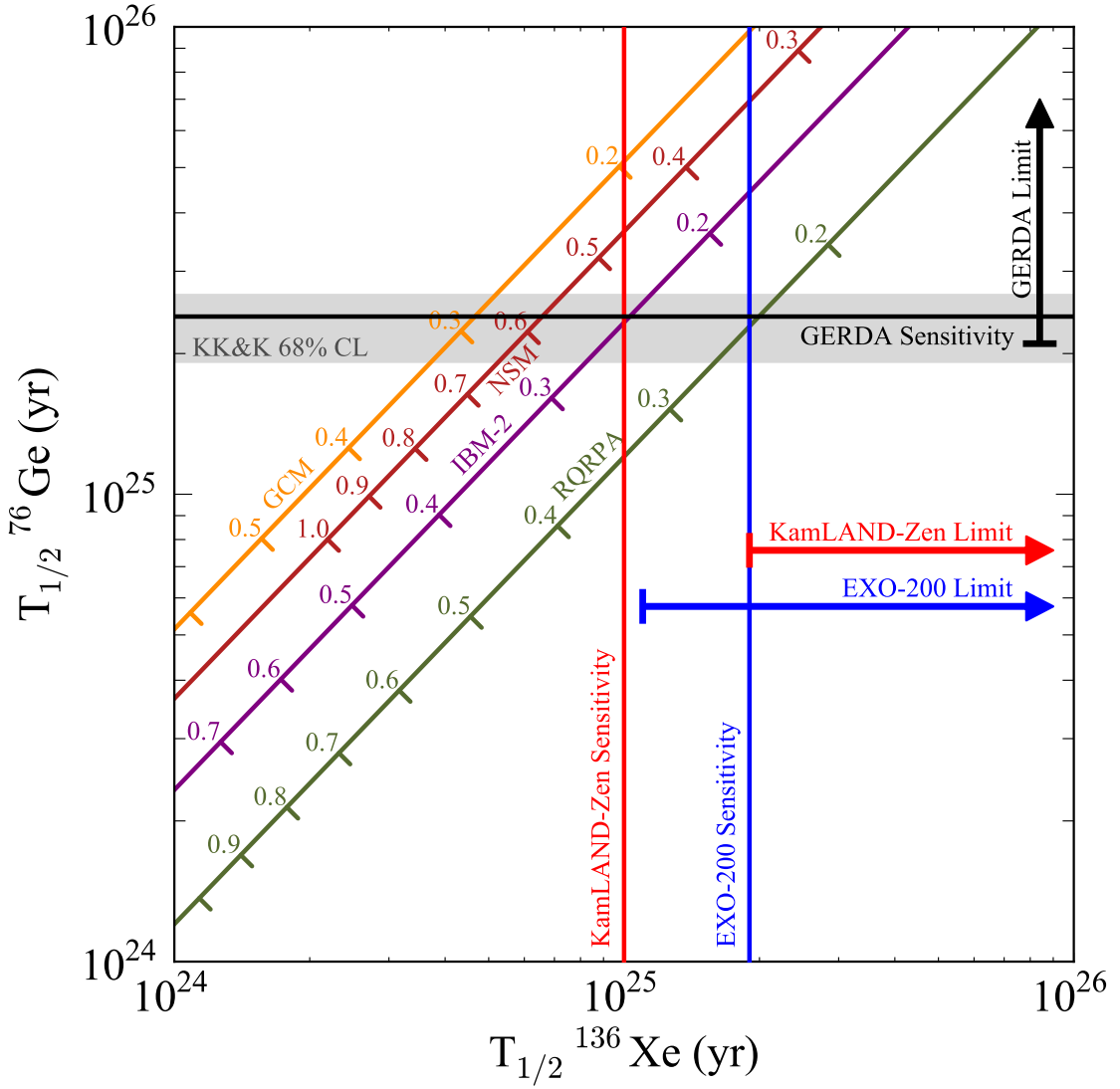


Figure 6.30: $\beta\beta0\nu$ constraints are shown from ^{136}Xe (horizontal) and ^{76}Ge (vertical). The four diagonal lines represent four recent matrix element computations [76–79] and one recent phase-space factor [22] relating the two half-lives; tick marks along the diagonal represent the corresponding mass $\langle m_{\beta\beta} \rangle$. 90% confidence limits and median 90% sensitivities are shown for the KamLand-Zen [31], GERDA [26], and EXO-200 experiments [35]; the claimed 2006 discovery by Klapdor-Kleingrothaus and Krivosheina is shown as a 1σ confidence interval. [80]

arrows indicate the actual limits set by each. For both experiments we can see that statistical fluctuations in the background account for factor-of-two differences between median sensitivity and observed limits; EXO-200 claims to be the most sensitive ^{136}Xe experiment, but KamLAND-Zen currently reports the strongest limit. Both experiments intend to continue running, and EXO-200 hopes that their next dataset is atypical in the other way.

Nuclear matrix elements are difficult to compute, as described in [the section I need to expand](#). However, figure 6.30 illustrated four diagonal lines corresponding to four different modern nuclear matrix calculations, and uses these values to relate the half-lives of ^{136}Xe and ^{76}Ge . The current median sensitivity and limit on the $\beta\beta0\nu$ half-life of ^{76}Ge from GERDA are shown as a horizontal line and vertical arrow, respectively. This is contrasted with the 2006 claimed discovery by Klapdor-Kleingrothaus and Krivosheina of $\beta\beta0\nu$ decay, which is not excluded by the more recent GERDA limit.

Furthermore, the nuclear matrix elements permit us to translate half-life lower limits into upper limits on the effective Majorana neutrino mass $\langle m_{\beta\beta} \rangle$. The relation is indicated, for each choice of nuclear matrix elements, by tick marks on the corresponding diagonal line. We can see that the GERDA and EXO-200 experiments are of similar strengths, depending most on the choice nuclear matrix elements; KamLAND-Zen is comparable in strength to GERDA for the RQRPA nuclear matrix elements, and stronger for all other choices in this plot. The 90%-confidence mass limit quoted by EXO-200 is $\langle m_{\beta\beta} \rangle < 190 - 450$ meV, depending on the choice of matrix elements. Recalling figure 1.8, this corresponds to a 90%-confidence limit

on the mass of the lightest neutrino eigenstate of $m_{min} < 0.691.63$ eV under the most conservative choice of Majorana phases. [35]

6.6 Comparison to Results without Denoising

I should do this – but need to finalize plots, which still needs a little more processing.

6.7 Summary

Chapter 7: Conclusions and Future Plans

Future plans to mention:

- Run1 contains up to 90 livetime-days, which is not negligible; denoising should have a significant improvement in resolution to offer even though APD gains were lower then. (Personal view – our next paper should include a combined analysis of Run1+Run2abcd, and whatever of Run3 is salvagable.)
- Further improvements in denoising are known to be achievable.
- Electronics upgrade could be a future hardware improvement.
- Restate some of the things listed in denoising, like anticorrelated cluster energies.

Bibliography

- [1] P.E. Hodgson, E. Gadioli, and E. Gadioli Erba. *Introductory Nuclear Physics*. Oxford Science Publications, 2003.
- [2] G. Audi, et al. The AME2012 atomic mass evaluation. *Chinese Physics C*, 36(12):1287–2014, 2012.
- [3] E. Majorana. Teoria simmetrica dellelettrone e del positrone. *Nuovo Cimento*, 14:171, 1937.
- [4] F. T. Avignone, III, S. R. Elliott, and J. Engel. Double beta decay, majorana neutrinos, and neutrino mass. *Reviews in Modern Physics*, 80:481, 2008.
- [5] H. Nishino, et al. Search for proton decay via $p- > e^+\pi^0$ and $p- > \mu^+\pi^0$ in a large water cherenkov detector. *Phys. Rev. Lett.*, 102:141801, Apr 2009. doi:10.1103/PhysRevLett.102.141801.
- [6] SINDRUM II Collaboration. Improved limit on the branching ratio of $\mu \rightarrow e^+$ conversion on titanium. *Physics Letters B*, 422:334–338, 1998.
- [7] G. Feinberg, P. Kabir, and S. Weinberg. Transformation of muons into electrons. *Phys. Rev. Lett.*, 3:527, 1959.
- [8] J. Schechter and J.W.F. Valle. Neutrinoless double- β decay in $su(2) \times u(1)$ theories. *Phys. Rev. D*, 25:2951, 1982.
- [9] Carter Hall and John Wilkerson. To appear in Annual Reviews of Nuclear and Particle Physics.
- [10] Rabindra N. Mohapatra and Goran Senjanović. Neutrino mass and spontaneous parity nonconservation. *Phys. Rev. Lett.*, 44:912–915, Apr 1980. doi:10.1103/PhysRevLett.44.912.
- [11] Y. Fukuda, et al. Evidence for oscillation of atmospheric neutrinos. *Phys. Rev. Lett.*, 81:1562–1567, Aug 1998. doi:10.1103/PhysRevLett.81.1562.
- [12] M. C. Gonzalez-Garcia and Yosef Nir. Neutrino masses and mixing: evidence and implications. *Rev. Mod. Phys.*, 75:345–402, Mar 2003. doi:10.1103/RevModPhys.75.345.

- [13] A. Gando, et al. Constraints on θ_{13} from a three-flavor oscillation analysis of reactor antineutrinos at KamLAND. *Phys. Rev. D*, 83:052002, Mar 2011. doi:10.1103/PhysRevD.83.052002.
- [14] P. Adamson, et al. Measurement of the neutrino mass splitting and flavor mixing by MINOS. *Phys. Rev. Lett.*, 106:181801, May 2011. doi:10.1103/PhysRevLett.106.181801.
- [15] F. P. An, et al. Improved measurement of electron antineutrino disappearance at Daya Bay. *Chinese Physics C*, 37(1):011001, 2013.
- [16] K. Abe, et al. Search for differences in oscillation parameters for atmospheric neutrinos and antineutrinos at Super-Kamiokande. *Phys. Rev. Lett.*, 107:241801, Dec 2011. doi:10.1103/PhysRevLett.107.241801.
- [17] Planck Collaboration. Planck 2013 results. XVI. cosmological parameters. *Astronomy and Astrophysics*, under review.
- [18] J. Angrik et al. KATRIN design report 2004. Technical report, KATRIN Collaboration, 2005.
- [19] V. N. Aseev, et al. Upper limit on the electron antineutrino mass from the Troitsk experiment. *Phys. Rev. D*, 84:112003, Dec 2011. doi:10.1103/PhysRevD.84.112003.
- [20] Joachim Wolf. The KATRIN neutrino mass experiment. *Nuclear Instruments and Methods in Physics Research Section A: Accelerators, Spectrometers, Detectors and Associated Equipment*, 623(1):442 – 444, 2010. ISSN 0168-9002. doi: <http://dx.doi.org/10.1016/j.nima.2010.03.030>. 1st International Conference on Technology and Instrumentation in Particle Physics.
- [21] Joseph A. Formaggio. Year one: Direct neutrino masses post Planck. In *TAUP2013*. To be published by Elsevier.
- [22] J. Kotila and F. Iachello. Phase-space factors for double- β decay. *Phys. Rev. C*, 85:034316, Mar 2012. doi:10.1103/PhysRevC.85.034316.
- [23] Kai Zuber. Summary of the workshop on: Nuclear matrix elements for neutrinoless double beta decay. Available at <http://arxiv.org/abs/nucl-ex/0511009>.
- [24] J Beringer, et al. Review of particle physics. *PHYSICAL REVIEW D*, 86(1):1504, 2012. ISSN 1550-7998.
- [25] S. Umebara, et al. Neutrino-less double- β decay of ^{48}Ca studied by $\text{CaF}_2(\text{Eu})$ scintillators. *Phys. Rev. C*, 78:058501, Nov 2008. doi:10.1103/PhysRevC.78.058501.
- [26] M. Agostini, et al. Results on neutrinoless double- β decay of ^{76}Ge from phase I of the GERDA experiment. *Phys. Rev. Lett.*, 111:122503, Sep 2013. doi:10.1103/PhysRevLett.111.122503.

- [27] A.S. Barabash and V.B. Brudanin. Investigation of double-beta decay with the NEMO-3 detector. *Physics of Atomic Nuclei*, 74(2):312–317, 2011. ISSN 1063-7788. doi:10.1134/S1063778811020062.
- [28] J. Argyriades, et al. Measurement of the two neutrino double beta decay half-life of Zr-96 with the NEMO-3 detector. *Nuclear Physics A*, 847(34):168 – 179, 2010. ISSN 0375-9474. doi:<http://dx.doi.org/10.1016/j.nuclphysa.2010.07.009>.
- [29] R. Arnold et al. Search for neutrinoless double-beta decay of ^{100}Mo with the NEMO-3 detector. Preprint available at <http://arxiv.org/abs/1311.5695>.
- [30] C. Arnaboldi, et al. Results from a search for the $0\nu\beta\beta$ -decay of ^{130}Te . *Phys. Rev. C*, 78:035502, Sep 2008. doi:10.1103/PhysRevC.78.035502.
- [31] A. Gando, et al. Limit on neutrinoless $\beta\beta$ decay of ^{136}Xe from the first phase of KamLAND-Zen and comparison with the positive claim in ^{76}Ge . *Phys. Rev. Lett.*, 110:062502, Feb 2013. doi:10.1103/PhysRevLett.110.062502.
- [32] J. Argyriades, et al. Measurement of the double- β decay half-life of ^{150}Nd and search for neutrinoless decay modes with the NEMO-3 detector. *Phys. Rev. C*, 80:032501, Sep 2009. doi:10.1103/PhysRevC.80.032501.
- [33] J. Barea, J. Kotila, and F. Iachello. Limits on neutrino masses from neutrinoless double- β decay. *Phys. Rev. Lett.*, 109:042501, Jul 2012. doi:10.1103/PhysRevLett.109.042501.
- [34] M Auger, et al. The EXO-200 detector, part I: detector design and construction. *Journal of Instrumentation*, 7(05):P05010, 2012.
- [35] J.B. Albert et al. Search for majorana neutrinos with the first two years of EXO-200 data. *To be determined*, 2014. Preprint available at <http://arxiv.org/abs/1402.6956>.
- [36] E. Conti, et al. Correlated fluctuations between luminescence and ionization in liquid xenon. *Phys. Rev. B*, 68:054201, Aug 2003. doi:10.1103/PhysRevB.68.054201.
- [37] C. E. Dahl. *The physics of background discrimination in liquid xenon, and first results from Xenon10 in the hunt for WIMP dark matter*. Ph.D. thesis, Princeton University, 2009.
- [38] J. B. Albert, et al. Improved measurement of the $2\nu\beta\beta$ half-life of ^{136}Xe with the EXO-200 detector. *Phys. Rev. C*, 89:015502, Jan 2014. doi:10.1103/PhysRevC.89.015502.
- [39] Josh Albert, et al. Neutron capture gamma tech note for $0\nu\beta\beta$ analysis (summer 2013), 2013. Internal EXO Document 021.

- [40] M.R. Bhat. Evaluated nuclear structure data file (ENSDF). In SyedM. Qaim, editor, *Nuclear Data for Science and Technology*, Research Reports in Physics, pages 817–821. Springer Berlin Heidelberg, 1992. ISBN 978-3-642-63473-4. doi: 10.1007/978-3-642-58113-7_227. Data extracted using the NNDC On-Line Data Service from the ENSDF database, file revised as of February 24, 2014.
- [41] Arthur H. Compton. A quantum theory of the scattering of x-rays by light elements. *Phys. Rev.*, 21:483–502, May 1923. doi:10.1103/PhysRev.21.483.
- [42] M.J. Berger, et al. XCOM: Photon cross section database (version 1.5). [Online] Available: <http://physics.nist.gov/xcom> [Sunday, 23-Feb-2014 03:19:51 EST], 2010. National Institute of Standards and Technology, Gaithersburg, MD.
- [43] D.S. Leonard, et al. Systematic study of trace radioactive impurities in candidate construction materials for EXO-200. *Nuclear Instruments and Methods in Physics Research Section A: Accelerators, Spectrometers, Detectors and Associated Equipment*, 591(3):490 – 509, 2008. ISSN 0168-9002. doi: <http://dx.doi.org/10.1016/j.nima.2008.03.001>.
- [44] R. Neilson, et al. Characterization of large area APDs for the EXO-200 detector. *Nuclear Instruments and Methods in Physics Research Section A: Accelerators, Spectrometers, Detectors and Associated Equipment*, 608(1):68 – 75, 2009. ISSN 0168-9002. doi:<http://dx.doi.org/10.1016/j.nima.2009.06.029>.
- [45] E.-I. Esch, et al. The cosmic ray muon flux at WIPP. *Nuclear Instruments and Methods in Physics Research Section A: Accelerators, Spectrometers, Detectors and Associated Equipment*, 538(13):516 – 525, 2005. ISSN 0168-9002. doi: <http://dx.doi.org/10.1016/j.nima.2004.09.005>.
- [46] M Moszyski, M Szawłowski, M Kapusta, and M Balcerzyk. Large area avalanche photodiodes in scintillation and x-rays detection. *Nuclear Instruments and Methods in Physics Research Section A: Accelerators, Spectrometers, Detectors and Associated Equipment*, 485(3):504 – 521, 2002. ISSN 0168-9002. doi:[http://dx.doi.org/10.1016/S0168-9002\(01\)02117-9](http://dx.doi.org/10.1016/S0168-9002(01)02117-9).
- [47] R. Neilson. APD installation: Selection and ganging, 2009. Presented to the EXO collaboration at the February 2009 EXO week meeting.
- [48] Josh Albert, et al. Energy correction technote for $0\nu\beta\beta$ analysis (spring 2013), 2013. Internal EXO Document 007.
- [49] EXO Monte Carlo Group. EXO 200 MonteCarlo documentation, 2013. Internal EXO Document 010.
- [50] EXO Reconstruction Analysis Group. Event reconstruction in EXO-200, 2013. Internal EXO Document 008.
- [51] Ryan Herbst. EXO electronics functional specification, draft revision 0.24, 2010. Internal EXO documentation.

- [52] L. Yang. EXO-200 electronics upgrade study report, 2013. Internal EXO Document 012.
- [53] Sheldon Ross. *A First Course in Probability*. Pearson Prentice Hall, 2006.
- [54] M Szydagis, et al. NEST: a comprehensive model for scintillation yield in liquid xenon. *Journal of Instrumentation*, 6(10):P10002, 2011.
- [55] A. El Guennouni, K. Jbilou, and H. Sadok. A block version of BiCGSTAB for linear systems with multiple right-hand sides. *Electronic Transactions on Numerical Analysis*, 16:129, 2003.
- [56] L. S. Blackford, et al. An updated set of basic linear algebra subprograms (BLAS). *ACM Trans. Math. Soft.*, 28(2):135, 2002.
- [57] Kazushige Goto and Robert A. van de Geijn. Anatomy of high-performance matrix multiplication. *ACM Trans. Math. Softw.*, 34(3):12:1–12:25, May 2008. ISSN 0098-3500. doi:10.1145/1356052.1356053.
- [58] Intel. *Reference Manual for Intel Math Kernel Library*, 11.1 edition.
- [59] A. S. Barabash. Double beta decay: present status. *Phys. Atom. Nucl.*, 73:162, 2010.
- [60] Arthur H. Compton. A quantum theory of the scattering of x-rays by light elements. *Physical Review*, 21:483, 1923.
- [61] Matteo Frigo and Steven G. Johnson. The design and implementation of FFTW3. *Proceedings of the IEEE*, 93(2):216–231, 2005. Special issue on “Program Generation, Optimization, and Platform Adaptation”.
- [62] Clayton Davis. The daq et cetera, or, stuff you wish you could ignore, but are about to find out you cannot, 2013. Presentation at Spring analysis workshop before EXO Week.
- [63] S. Herrin. *Double Beta Decay in Xenon-136: Measuring the Neutrino-Emitting Mode and Searching for Majoron-Emitting Modes*. Ph.D. thesis, Stanford University, 2013.
- [64] David W. Scott. *Multivariate density estimation : theory, practice, and visualization*. John Wiley and Sons, Inc., 1992.
- [65] S. Agostinelli, et al. Geant4a simulation toolkit. *Nuclear Instruments and Methods in Physics Research Section A: Accelerators, Spectrometers, Detectors and Associated Equipment*, 506(3):250 – 303, 2003. ISSN 0168-9002. doi:[http://dx.doi.org/10.1016/S0168-9002\(03\)01368-8](http://dx.doi.org/10.1016/S0168-9002(03)01368-8).
- [66] J. Allison, et al. Geant4 developments and applications. *Nuclear Science, IEEE Transactions on*, 53(1):270–278, Feb 2006. ISSN 0018-9499. doi:10.1109/TNS.2006.869826.

- [67] M Dressel. Geometrical importance sampling in Geant4: from design to verification. Technical Report CERN-OPEN-2003-048, CERN, Geneva, Sep 2003.
- [68] W. Shockley. Currents to conductors induced by a moving point charge. *Journal of Applied Physics*, 9(10):635–636, 1938. doi:<http://dx.doi.org/10.1063/1.1710367>.
- [69] Simon Ramo. Currents induced by electron motion. *Proceedings of the IRE*, 27(9):584–585, Sept 1939. ISSN 0096-8390. doi:[10.1109/JRPROC.1939.228757](https://doi.org/10.1109/JRPROC.1939.228757).
- [70] D.O. North. An analysis of the factors which determine signal/noise discrimination in pulsed-carrier systems. *Proceedings of the IEEE*, 51(7):1016–1027, July 1963. ISSN 0018-9219. doi:[10.1109/PROC.1963.2383](https://doi.org/10.1109/PROC.1963.2383). Reprint of original 1943 paper, which was classified.
- [71] Josh Albert, et al. Energy correction technote for $0\nu\beta\beta$ analysis (august 2013), 2013 (revised February 2014). Internal EXO Document 018.
- [72] G.F. Knoll. *Radiation detection and measurement*. Wiley, 2000. ISBN 9780471073383.
- [73] Caio Licciardi. Calculation of the average energy resolution used in the search for $\beta\beta0\nu$ with run-2 data, 2014. Internal EXO Document 019.
- [74] Igor Ostrovskiy. 0 2013. final analysis documentation, 2013. Internal EXO Document 015.
- [75] Glen Cowan, Kyle Cranmer, Eilam Gross, and Ofer Vitells. Asymptotic formulae for likelihood-based tests of new physics. *The European Physical Journal C*, 71(2):1–19, 2011. ISSN 1434-6044. doi:[10.1140/epjc/s10052-011-1554-0](https://doi.org/10.1140/epjc/s10052-011-1554-0).
- [76] Tomás R. Rodríguez and Gabriel Martínez-Pinedo. Energy density functional study of nuclear matrix elements for neutrinoless $\beta\beta$ decay. *Phys. Rev. Lett.*, 105:252503, Dec 2010. doi:[10.1103/PhysRevLett.105.252503](https://doi.org/10.1103/PhysRevLett.105.252503).
- [77] J. Menndez, A. Poves, E. Caurier, and F. Nowacki. Disassembling the nuclear matrix elements of the neutrinoless decay. *Nuclear Physics A*, 818(34):139 – 151, 2009. ISSN 0375-9474. doi:<http://dx.doi.org/10.1016/j.nuclphysa.2008.12.005>.
- [78] J. Barea, J. Kotila, and F. Iachello. Nuclear matrix elements for double- β decay. *Phys. Rev. C*, 87:014315, Jan 2013. doi:[10.1103/PhysRevC.87.014315](https://doi.org/10.1103/PhysRevC.87.014315).
- [79] Fedor Šimkovic, Vadim Rodin, Amand Faessler, and Petr Vogel. $0\nu\beta\beta$ and $2\nu\beta\beta$ nuclear matrix elements, quasiparticle random-phase approximation, and isospin symmetry restoration. *Phys. Rev. C*, 87:045501, Apr 2013. doi:[10.1103/PhysRevC.87.045501](https://doi.org/10.1103/PhysRevC.87.045501).
- [80] H. V. Klapdor-Kleingrothaus and I. V. Krivosheina. Evidence for neutrinoless double beta decay. *Mod. Phys. Lett. A*, 21:20:1547, 2006.